

THEORY AND NUMERICS OF THE COMMUNITY OCEAN VERTICAL MIXING (CVMix) PROJECT

Stephen M. Griffies ^{1*}, Michael Levy ^{2†}, Alistair J. Adcroft ^{3*}, Gokhan Danabasoglu ^{4†},
Robert W. Hallberg ^{5*}, Doug Jacobsen ^{6△}, William Large ^{7†}, and Todd Ringler ^{8△}

^{*}NOAA/Geophysical Fluid Dynamics Laboratory, Princeton USA

[†]National Center for Atmospheric Research, Boulder USA

[△]Los Alamos National Laboratory, Los Alamos USA

January 17, 2015

¹Stephen.Griffies@noaa.gov

²MLevy@ucar.edu

³Alistair.Adcroft@noaa.gov

⁴Gokhan@ucar.edu

⁵Robert.Hallberg@noaa.gov

⁶Jacobsen.douglas@gmail.com

⁷Wily@ucar.edu

⁸Ringler@lanl.gov

THE CVMix PROJECT

COMMUNITY OCEAN VERTICAL MIXING (CVMix) is a software package that aims to provide transparent, robust, flexible, well documented, shared Fortran source code for use in parameterizing vertical mixing processes in numerical ocean models. The project is focused on developing software for a consensus of closures that return a vertical diffusivity, viscosity, and possibly a non-local transport, with each quantity dependent on the tracer or velocity being mixed. CVMix modules are written as kernels designed for use in a variety of Fortran ocean model codes such as MPAS-ocean, MOM, and POP. CVMix modules use MKS units and expect the same for input and output. Code development occurs within a community of scientists and engineers who make use of CVMix modules for a variety of ocean codes. CVMix modules are freely distributed to the open source community under GPLv2 using an open source methodology.

This document is freely distributed and should be referenced as the following.

THEORY AND NUMERICS OF THE COMMUNITY OCEAN VERTICAL MIXING (CVMix) PROJECT

S.M. Griffies, M. Levy, A.J. Adcroft, G. Danabasoglu, R.W. Hallberg, D. Jacobsen, W. Large, T. Ringler

Technical Report

Draft from January 17, 2015

95 + v pages

This document was prepared using \LaTeX as described by [Lamport \(1994\)](#) and [Goossens et al. \(1994\)](#).

Contents

1	CVMix PARAMETERIZATIONS	1
1.1	Vertical mixing parameterizations in CVMix	1
1.2	General form of CVMix parameterizations	2
1.3	KPP matching and ordering the CVMix schemes	3
2	ELEMENTS OF CVMix PARAMETERIZATIONS	5
2.1	Discrete vertical grid	5
2.2	Gravitational stability	7
2.3	Gradient Richardson number	12
3	SAMPLE CHAPTER FOR CVMix DOCUMENTATION	17
3.1	Introduction to the mixing scheme	17
3.2	Theory	18
3.3	Numerical implementation in CVMix	18
3.4	Further sections	18
4	STATIC BACKGROUND SCHEMES	19
4.1	Options for static background mixing coefficients	19
4.2	The profile from Bryan-Lewis (1979)	19
5	PARAMETERIZED SHEAR INDUCED MIXING	23
5.1	Mixing from shear instability	23
5.2	Pacanowski and Philander mixing	24
5.3	Richardson number mixing from Large et al. (1994)	24
6	ENERGETICALLY BASED MIXING SCHEMES FROM TIDAL DISSIPATION	25
6.1	Introduction to tidal induced mixing	25
6.2	Energetic elements of tide mixing parameterizations	26
6.3	The Simmons et al. (2004) scheme	30
7	DOUBLE DIFFUSION	33
7.1	Introduction to mixing from double diffusive processes	33
7.2	Salt fingering regime	34
7.3	Diffusive convective regime	34
8	KPP SURFACE OCEAN BOUNDARY LAYER	35
8.1	Elements of the K-profile parameterization (KPP)	37
8.2	Surface ocean boundary momentum fluxes	44
8.3	Surface ocean boundary buoyancy fluxes	45
8.4	Surface layer and Monin-Obukhov similarity	52

8.5	Specifying the KPP parameterization	56
8.6	Further considerations for the KPP non-local term	78
8.7	KPP with surface waves	84
8.8	Symbols used in this chapter	87
BIBLIOGRAPHY		91

List of Figures

1.1	Flow diagram for CVMix schemes	4
2.1	Discrete vertical column for CVMix modules	7
2.2	Parcel displacements for gravitational stability calculation	10
2.3	Placement of fields onto the B-grid	14
2.4	Placement of fields onto the C-grid	15
4.1	Bryan-Lewis background diffusivities	21
4.2	Latitude-depth Bryan-Lewis diffusivity	21
8.1	KPP boundary layer schematic	41
8.2	Figure 1 from Large et al. (1994)	43
8.3	Figure 2 from Large et al. (1994)	60
8.4	Figure B1 from Large et al. (1994)	61
8.5	Alternative similarity functions	62
8.6	Determining non-local gravitational stability	73
8.7	KPP shape function	80
8.8	KPP temperature test	82
8.9	Modified KPP shape function	84
8.10	KPP temperature test with modified non-local	85

CVMix PARAMETERIZATIONS

Contents

1.1	Vertical mixing parameterizations in CVMix	1
1.2	General form of CVMix parameterizations	2
1.3	KPP matching and ordering the CVMix schemes	3

We provide in this chapter an overview of the vertical mixing parameterizations available with CVMix.

1.1 Vertical mixing parameterizations in CVMix

The CVMix Project aims to address the needs of various ocean modeling groups to code, test, tune, and document parameterizations of oceanic vertical mixing for numerical ocean simulations. Phase I of the project has focused on first-order turbulence closures for vertical mixing processes. Future development may consider higher order schemes, motivated by developments with the General Ocean Turbulence Model (GOTM) from [Umlauf et al. \(2005\)](#). Notably, CVMix does *not* determine time stepping for the model prognostic fields. Instead, time stepping is the responsibility of the calling model code.

The following schemes are included in the CVMix parameterizations during Phase I of the development.

- **STATIC BACKGROUND MIXING** (Chapter 4): Certain turbulent processes, in particular the ambient background gravity wave “noise”, constitute a background level of mixing that is largely steady in time from the perspective of large-scaling ocean modeling. Though assumed to be time independent, these processes generally have a nontrivial space dependence. CVMix provides options for various of these time independent schemes:
 - the vertical profile from [Bryan and Lewis \(1979\)](#);
- **Shear INDUCED MIXING** (Chapter 5): The following schemes are available for shear mixing:
 - [Pacanowski and Philander \(1981\)](#), applicable largely for tropical circulation;
 - [Large et al. \(1994\)](#) and [Large and Gent \(1999\)](#), which builds on the [Pacanowski and Philander \(1981\)](#) scheme;
- **TIDALLY INDUCED MIXING** (Chapter 6): The following schemes are available for parameterizing mixing induced by ocean tides.
 - [Simmons et al. \(2004\)](#)
- **DOUBLE DIFFUSIVE PROCESSES** (Chapter 7): Double diffusive processes arise from the distinct mixing properties of temperature relative to salinity and other material tracers.

- KPP SURFACE BOUNDARY LAYER (Chapter 8): The K-profile parameterization (KPP) scheme from [Large et al. \(1994\)](#) provides for a diffusivity as well as a non-local transport, each within the surface planetary boundary layer.
- VERTICAL CONVECTIVE MIXING: Vertical profiles can become gravitationally unstable, such as when the ocean is forced with a negative buoyancy flux. Older approaches such as [Cox \(1984\)](#) and [Rahmstorf \(1993\)](#) considered a convective *adjustment* algorithm, in which vertical pairs of grid cells were adjusted towards a profile of static stability. In effect, the vertical diffusivity is infinite when using adjustment schemes. CVMix does *not* provide options for convective adjustment. Instead, CVMix allows for the specification of a diffusivity that is large in regions of gravitational instability, thus enabling vertical convective *mixing* rather than *adjustment*. Notably, when using the KPP surface boundary layer scheme, convective mixing is *not* computed inside the KPP boundary layer. Instead, it is only computed beneath the boundary layer, and it is done so *after* the KPP boundary layer matching has occurred (see Section 1.3).

1.2 General form of CVMix parameterizations

CVMix focuses only on vertical transport processes in the ocean, so that we are concerned with the tracer or velocity equation in the form

$$\frac{\partial \bar{\lambda}}{\partial t} = -\frac{\partial}{\partial z} (\overline{w' \lambda'} + \bar{w} \bar{\lambda}). \quad (1.1)$$

In this equation, w' is the turbulent or fluctuating portion of the vertical velocity¹

$$w = w' + \bar{w}, \quad (1.2)$$

λ' is a fluctuating scalar or velocity component

$$\lambda = \lambda' + \bar{\lambda}, \quad (1.3)$$

and the overline denotes an Eulerian ensemble or time average that separates the mean flow from turbulent fluctuations. The vertical flux $\bar{w} \bar{\lambda}$ is represented in a numerical model by an advection operator or remapping operation, and it is comprised of flow *resolved* by the model grid. In contrast, $\overline{w' \lambda'}$ is the correlation between fluctuations in the vertical velocity component and the field λ . This correlation is often termed the *turbulent flux* of λ . It is not explicitly represented by a numerical model, since it arises from processes at the subgrid scale. CVMix code provides a suite of closures, or *parameterizations*, for this subgrid scale flux.

We are interested in those correlations $\overline{w' \lambda'}$ that can be parameterized in terms of vertical diffusion or vertical non-local mixing. That is, all parameterizations considered in CVMix can be formulated in terms of a diffusivity and a non-local transport, in which case the turbulent flux is written as

$$\overline{w' \lambda'} = -K_\lambda \left(\frac{\partial \bar{\lambda}}{\partial z} \right) + K_\lambda^{\text{non-local}} \gamma_\lambda. \quad (1.4)$$

The first term on the right hand side of equation (1.4) provides for the familiar downgradient vertical diffusion determined by a non-negative vertical diffusivity, $K_\lambda \geq 0$, and the local vertical derivative of the model's resolved field, $\partial \bar{\lambda} / \partial z$. This term is referred to as the local portion of the vertical mixing parameterization

$$\overline{w' \lambda'}^{\text{local}} = -K_\lambda \left(\frac{\partial \bar{\lambda}}{\partial z} \right). \quad (1.5)$$

Note that the term “local” is used for this portion of the parameterized flux (1.4) since it is determined by the local derivative of the mean field, $\bar{\lambda}$. However, the diffusivity can generally be determined as a non-local function of boundary layer properties, with such being the case for the KPP scheme (Chapter 8).

¹In Chapter 8, we follow the notation of [Large et al. \(1994\)](#) by writing the mean quantities with an uppercase, W and Λ , and turbulent fluctuations with a lowercase, w and λ . For the present chapter, we follow the more standard notation of equation (1.2).

The second term in equation (1.4), γ_λ , accounts for non-local transport that is not directly associated with local vertical gradients of λ , in which we have

$$\overline{w'\lambda'}^{\text{non-local}} = K_\lambda^{\text{non-local}} \gamma_\lambda. \quad (1.6)$$

KPP is the only scheme available with CVMix that prescribes a nonzero value for γ_λ . In the original implementation from [Large et al. \(1994\)](#), they considered $K_\lambda^{\text{non-local}} = K_\lambda$. However, as noted in Sections 1.3 and 8.5.3, that prescription leads to problems for the non-local flux $\overline{w'\lambda'}^{\text{non-local}}$ for those cases where the diffusivity $K_\lambda^{\text{non-local}}$ at the base of the boundary layer does not vanish. When $K_\lambda^{\text{non-local}}$ does not vanish at the boundary layer base, then the non-local flux has a spurious jump condition across the boundary layer base, since the flux vanishes below the boundary layer. We leave further details of this issue for the discussion in Section 8.5.3, where we argue that the KPP scheme should set *both* its local and non-local fluxes smoothly to zero at the boundary layer base.

Every scheme available in CVMix computes parameterized turbulent fluxes based on a suite of inputs from the calling model, such as the surface buoyancy and momentum fluxes, vertical stratification, and vertical shear. There may also need to be information about the bottom roughness and unresolved tide speeds. Besides the diffusivity and non-local transport, various diagnostic fields are available to help understand the internal workings of the parameterizations.

1.3 KPP matching and ordering the CVMix schemes

Certain of the CVMix schemes represent parameterizations of processes that are largely independent. Their resulting diffusivities and viscosities are thus added to produce a net mixing coefficient. Other schemes, however, must be called in a certain order given the underlying assumptions built into the scheme. The issue concerns the KPP surface boundary layer scheme when used in a form according to [Large et al. \(1994\)](#), in which diffusivities are matched across the boundary layer base. We here summarize the two main issues associated with this approach.

- **KPP AFTER INTERIOR NON-CONVECTIVE MIXING:** As implemented according to [Large et al. \(1994\)](#), the KPP scheme matches diffusivities at the base of the boundary layer to values computed beneath the boundary layer (Section 8.5.3). In this case, KPP must be called subsequent to those schemes determining non-convective mixing coefficients in the ocean interior.
- **KPP BEFORE INTERIOR CONVECTIVE MIXING:** Again, if implementing KPP according to the methods from [Large et al. \(1994\)](#), diffusivity matching at the base of the KPP boundary layer intrinsically assumes there to be a transition from typically larger diffusivities in the boundary layer to typically smaller diffusivities in the interior. However, this sort of transition cannot always be ensured, since gravitationally unstable water can appear beneath the boundary layer in which case the interior diffusivities can be quite large. Problems with the diffusivity matching occur if insisting that KPP match its boundary layer diffusivity to a potentially large interior diffusivity arising from convective mixing. These problems are ameliorated if parameterized convective mixing in the ocean interior is called *after* the KPP boundary layer scheme. Furthermore, note that convective parameterizations are not used inside the KPP boundary layer, since KPP provides the mixing coefficients in the boundary layer.

The above concerns with the [Large et al. \(1994\)](#) implementation of KPP are eliminated *if* one does not match the boundary layer diffusivity to the interior diffusivity. In this case, the KPP scheme and all other schemes can be called in any order, with the resulting net diffusivity used after all of the physical processes contribute to the mixing coefficients. This alternative simplified approach to the KPP scheme is discussed in Section 8.5.3. We recommend using the simpler approach, unless aiming to reproduce older results from KPP formulated using the [Large et al. \(1994\)](#) matching conditions.

These considerations lead to the flow diagram shown in Figure 1.1 for use of CVMix schemes.

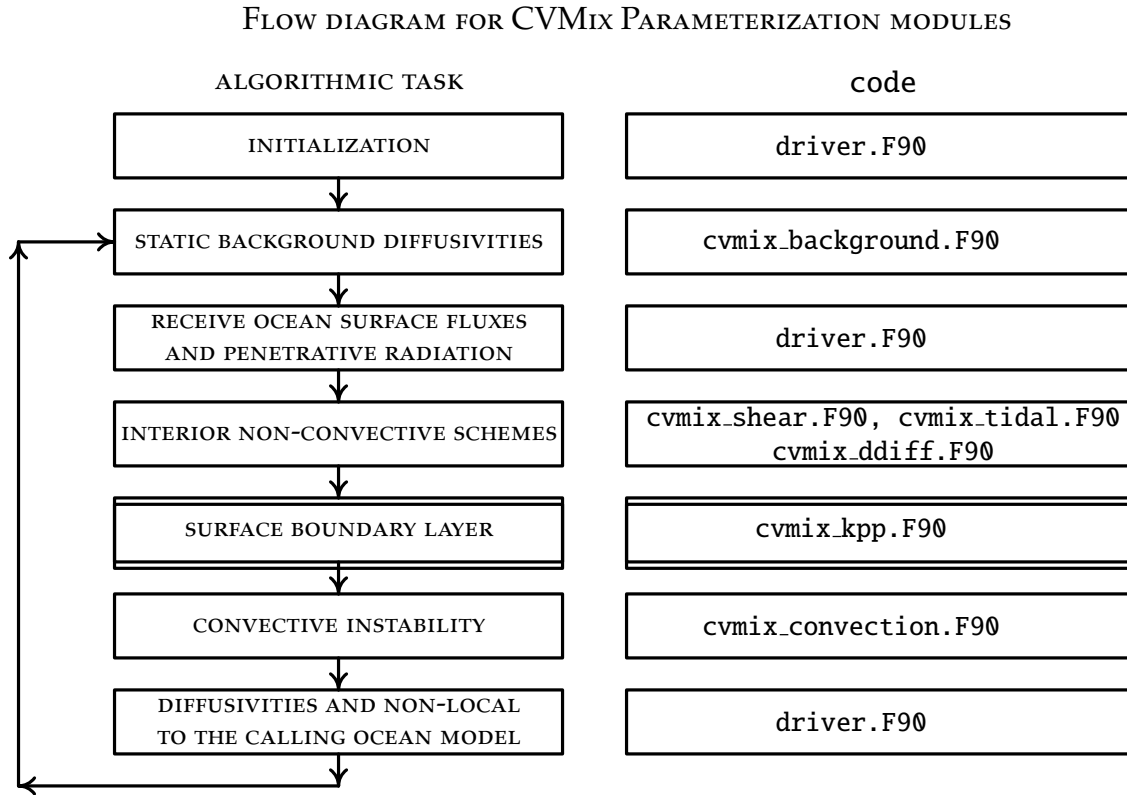


Figure 1.1: This flow diagram depicts the general algorithmic steps required to utilize the CVMix parameterization modules. The initialization step occurs in the ocean model (e.g., MPAS-ocean, MOM, or POP) calling the CVMix modules. This initialization serves to set up arrays and derived type structures, all as a function of the input that it receives from the calling ocean model code. The next step during initialization is to call the module `cvmix_background.F90` to fill chosen static background diffusivities. Upon entering the time dependent portion of the ocean model integration, the driver receives surface fluxes and penetrative radiative fluxes. Calls are made to chosen interior non-convective mixing schemes, such as shear mixing, tide mixing, and double diffusion. Thereafter, the surface boundary layer scheme is called, with KPP the scheme targetted for Phase I of CVMix. If implementing the KPP scheme according to [Large et al. \(1994\)](#), then the boundary layer calculation *must* come after the interior non-convective portion, and before the convective portion (see discussion in Section 1.3). If instead using the simpler approach detailed in Section 8.5.3, then KPP can be called in any order within the calling tree. After the boundary layer, then convective mixing is called, with regions of gravitationally unstable water given a large diffusivity. Notably, if KPP is used for the surface boundary layer, parameterized convective mixing is generally performed only beneath the KPP boundary layer. The final step returns the diffusivity K_λ , viscosity, and non-local transport $K_\lambda^{\text{non-local}} \gamma_\lambda$ (equation (1.6)), arrays to the calling ocean model code. A new time step starts by reinitializing the diffusivities to their static background values.

ELEMENTS OF CVMix PARAMETERIZATIONS

Contents

2.1	Discrete vertical grid	5
2.2	Gravitational stability	7
2.2.1	Density change under infinitesimal displacements	8
2.2.2	Neutral directions	8
2.2.3	Squared buoyancy frequency	9
2.2.3.1	Stability to upward displacements from a deeper reference point	9
2.2.3.2	Stability to downward displacements from a shallower reference point	11
2.2.3.3	Combined displacements to approximate gravitational stability at interface depth	11
2.2.3.4	Linear approximation: not recommended in general	12
2.2.3.5	Discrete calculation of the squared buoyancy frequency	12
2.3	Gradient Richardson number	12
2.3.1	Considerations for the B-grid	13
2.3.2	Considerations for the C-grid	14

We present in this chapter certain elements required for computing CVMix parameterizations. Details specific to particular schemes are provided in later chapters.

2.1 Discrete vertical grid

As part of the numerical discretizations used by CVMix modules, we have need to describe how discrete fields are placed on a vertical grid, and how finite difference operations are performed. A vertical column generally has time dependent positions of the discrete fields, distances between the positions, and thicknesses of the cells over which the discrete fields are defined. Generality is necessary for models where grid cell thicknesses are functions of time, and CVMix allows for such freedom.

Figure 2.1 provides a schematic of the conventions for a tracer column used by CVMix modules. The conventions are motivated by those used in MOM and POP, yet some details may differ slightly. A summary of the choices made in developing this figure are as follows.

- **VERTICAL COORDINATE AND DEPTH:** The vertical coordinate z increases upward and extends from the ocean bottom at $z = -H(x, y)$ to the sea surface at $z = \eta(x, y, t)$

$$-H(x, y) \leq z \leq \eta(x, y, t). \tag{2.1}$$

Conversely, the *depth*

$$d = -z + \eta \quad (2.2)$$

increases from a value of $d = 0$ at $z = \eta$ to $d = H + \eta$ at $z = -H$

$$0 \leq d \leq H + \eta. \quad (2.3)$$

So in summary, depth increases when moving down into the ocean starting from the free surface, and z increases moving up from a resting ocean at $z = 0$.

- HEIGHT COORDINATE: The height vertical coordinate is defined as minus the depth

$$\mathcal{H} = -d = z - \eta \quad (2.4)$$

and so represents the height above the sea surface. In the ocean, the height is negative (liquid ocean sits beneath the sea surface), and sits within the range of values

$$-(H + \eta) \leq \mathcal{H} \leq 0. \quad (2.5)$$

For the CVMix implementation of the KPP scheme detailed in Chapter 8, the code assumes the vertical coordinate provided by the calling routine is the height, so that the CVMix code does not need to be given the sea level field.

- TRACER CELL ARRAYS: Tracer cell arrays are labelled with the discrete index kt , and have dimensions $nlevs$. The index kt increases downward starting from $kt = 1$ for the top model grid cell. The number of wet points, $nlevs$, is a function of the column. Examples of tracer cell arrays include temperature, salinity, pressure, density, thermal expansion coefficient, and haline contraction coefficient.
- W-CELL OR INTERFACE ARRAYS: W-cell or interface arrays are labelled with the discrete index kw , and have dimensions $nlevs+1$. The index kw increases downward starting from $kw = 1$ at the top ocean interface. The notation “w-cell” originates from the continuity equation, in which the vertical velocity component, w , transfers mass or tracer across the vertical interfaces of tracer cells. Examples of w-cell or interface arrays are diffusivity, viscosity, vertical tracer derivatives, buoyancy frequency, and Richardson number. For most w-cell arrays, both the top interface at $kw=1$ and bottom interface at $kw=nlevs+1$ have zero values.

One argument for using $nlevs+1$ interfaces is that we avoid ambiguity of where the data resides. Interface arrays of size $nlevs$ could start at either the top or bottom of the first grid cell and, even if well documented, the ambiguity will increase the potential for code errors. It does not matter so much whether interface arrays are dimensioned $0:nlevs$ or $1:nlevs+1$; there is only one way the data could be laid out relative to the tracer arrays which have dimensions $1:nlevs$. Yet the reason to prefer $1:nlevs+1$ is that this dimensioning simplifies declarations and argument passing, given the standard assumptions made by Fortran in laying out memory for arrays.

- TRACER CELL THICKNESS: The rectangular boxes in Figure 2.1 represent tracer cells whose thickness is measured by the array element $dzt(kt)$ with units of meter. This array has dimensions $dzt(nlevs)$. These thicknesses are generally time dependent. The array dzt is an input to CVMix, passed from the ocean model each time step.
- W-CELL THICKNESS OR TRACER POINT SEPARATION: The array dzw has dimensions $dzw(nlevs+1)$. The array element $dzw(kw=1)$ measures distance (in meters) from the top of the top tracer cell to the tracer point $T(kt=1)$, and array element $dzw(kw=nlevs+1)$ measures the distance from the bottom tracer point $T(kt=nlevs)$ to the bottom of the bottom tracer cell. Intermediate elements of dzw measure the distance between tracer points, or equivalently the thickness of a w-cell. These distances are generally time dependent. The array dzw is an input to CVMix, passed from the ocean model each time step.
- DISTANCE FROM OCEAN SURFACE TO TRACER CELL POINT: The distance (in meters) from the tracer cell point to the ocean surface is given by the array element $zt(kt)$. This array has dimensions $zt(nlevs)$. If needed, the array zt is constructed inside CVMix code based on the values of dzt and dzw .

- **DISTANCE FROM OCEAN SURFACE TO INTERFACE:** The distance from the tracer cell interface, or the w-point, to the ocean surface is given by the array element $zw(kw)$. This array has dimensions $zw(nlevs+1)$. If needed, the array zw is constructed inside CVMix code based on the values of dzt and dzw .

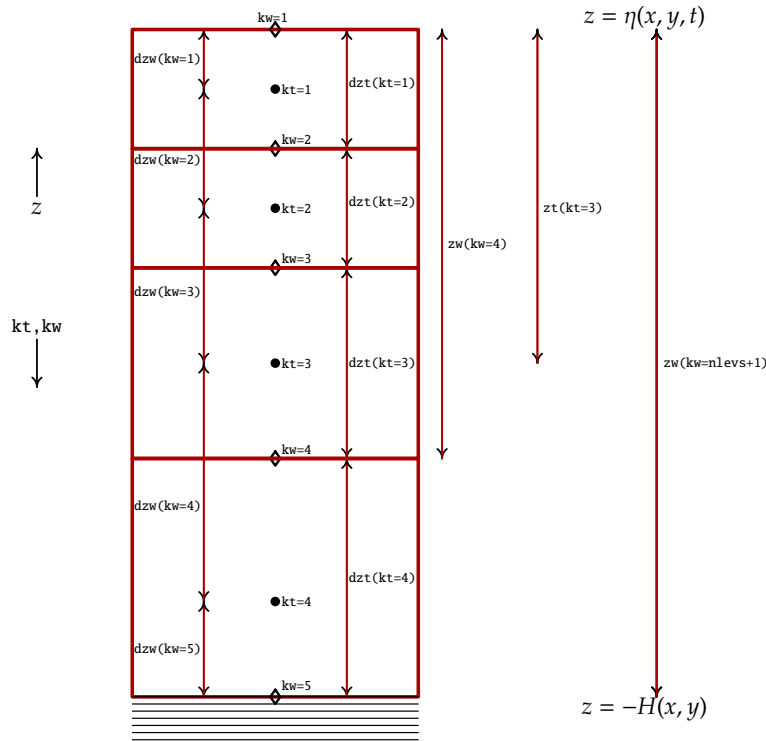


Figure 2.1: Schematic of a discrete vertical column used in CVMix modules, with the surface at $z = \eta(x, y, t)$ and bottom at $z = -H(x, y)$. The vertical coordinate z increases upward, whereas the discrete vertical indices kt and kw increase downward. CVMix code assumes distances and thicknesses are in units of meters. The rectangular boxes represent tracer cells in the ocean model. The array element $dzt(kt)$ measures the thickness of a tracer cell. This array has dimensions $dzt(nlevs)$, where $nlevs$ is the number of wet cells in a particular column. For this particular example, $nlevs = 4$. The array dzw has dimensions $dzw(nlevs+1)$. The array element $dzw(kw=1)$ measures the distance from the top of the top tracer cell to the tracer point $T(kt=1)$, and array element $zw(kw=nlevs+1)$ measures the distance from the bottom tracer point $T(kt=nlevs)$ to the bottom of the bottom tracer cell. Intermediate elements of dzw measure the distance between tracer points, or equivalently the thickness of w-cells. The distance from the ocean surface to a tracer point is measured by the array element $zt(kt)$, and the distance to the interface is measured by $zw(kw)$. The total thickness of a column is $zw(nlevs+1)$, and it is generally time dependent, as are all of the grid distances dzt and dzw . Arrays that are defined at the interface, such as buoyancy frequency, Richardson number, diffusivity, viscosity, have vertical indices kw . Arrays defined at the tracer cell point, such as temperature, salinity, and density, have vertical indices kt .

2.2 Gravitational stability

Buoyancy stratification plays a key role in physical ocean processes. We have need to quantify stratification for use in CVMix parameterizations, along with the associated gravitational stability of a water column. For this purpose, we introduce the notion of an adiabatic and isohaline parcel displacement, from which we

develop an algorithm for computing the buoyancy frequency used to measure vertical stratification. The notions detailed here should be respected by the calling ocean model in order for the CVMix modules to produce physically relevant results.

The squared buoyancy frequency, N^2 , is an input to CVMix modules.

2.2.1 Density change under infinitesimal displacements

Consider a displacement $d\mathbf{x}$ of a fluid parcel. To leading order, the *in situ* density at the new point is related to the reference density by

$$\rho(\mathbf{x} + d\mathbf{x}) = \rho(\mathbf{x}) + d\rho(\mathbf{x}). \quad (2.6)$$

Using the leading order term in a Taylor series expansion, the density increment can be approximated by

$$d\rho = \rho(\mathbf{x} + d\mathbf{x}) - \rho(\mathbf{x}) \quad (2.7a)$$

$$\approx d\mathbf{x} \cdot \nabla \rho \quad (2.7b)$$

$$= \rho d\mathbf{x} \cdot \rho^{-1} \nabla \rho \quad (2.7c)$$

$$= \rho d\mathbf{x} \cdot \left(-\alpha \nabla \Theta + \beta \nabla S + \frac{\nabla p}{\rho c_{\text{sound}}^2} \right), \quad (2.7d)$$

where all terms on the right hand side are evaluated at the reference point \mathbf{x} . To reach this expression, we introduced the thermal expansion coefficient

$$\alpha = -\frac{1}{\rho} \left(\frac{\partial \rho}{\partial \Theta} \right), \quad (2.8)$$

the haline contraction coefficient

$$\beta = \frac{1}{\rho} \left(\frac{\partial \rho}{\partial S} \right), \quad (2.9)$$

and the squared sound speed

$$c_{\text{sound}}^2 = \left(\frac{\partial p}{\partial \rho} \right). \quad (2.10)$$

The ambient density at the new point, $\rho(\mathbf{x} + d\mathbf{x})$, thus differs from density at the reference point, $\rho(\mathbf{x})$, by an amount $d\rho(\mathbf{x})$ according to

$$\rho(\mathbf{x} + d\mathbf{x}) - \rho(\mathbf{x}) = \rho(\mathbf{x}) d\mathbf{x} \cdot \left(-\alpha \nabla \Theta + \beta \nabla S + \frac{\nabla p}{\rho c_{\text{sound}}^2} \right). \quad (2.11)$$

2.2.2 Neutral directions

Parcel displacements associated with mixing will change the parcel's temperature, salinity, and concentration of other material tracers. Rather than considering such mixing processes, we here wish to know if through buoyancy forces alone, a particular parcel displacement is favored, resisted, or neutral. For this purpose, we introduce the notion of a displacement restricted to adiabatic and isohaline conditions (i.e., no heat or salt exchanged during the parcel displacement). Such displacements occur in the absence of mechanical energy needed for mixing. Our goal is thus to determine *neutral* directions, whereby non-dissipative motion occurs in the absence of buoyancy forces.

The density change associated with an adiabatic and isohaline displacement is determined just by pressure changes arising from the displacement, so that

$$\rho(\mathbf{x} + d\mathbf{x})_{\text{adiabatic/isohaline}} - \rho(\mathbf{x}) = \rho d\mathbf{x} \cdot \left(\frac{\nabla p}{\rho c_{\text{sound}}^2} \right). \quad (2.12)$$

This density change occurs merely through the pressure dependence of *in situ* density. Operationally, to compute $\rho(\mathbf{x} + d\mathbf{x})_{\text{adiabatic/isohaline}}$, we may choose to evaluate the right hand side of equation (2.12), or we may evaluate the equation of state at the temperature and salinity of the reference point, \mathbf{x} , but with pressure at the displaced point, $\mathbf{x} + d\mathbf{x}$

$$\rho(\mathbf{x} + d\mathbf{x})_{\text{adiabatic/isohaline}} = \rho[\Theta(\mathbf{x}), S(\mathbf{x}), p(\mathbf{x} + d\mathbf{x})]. \quad (2.13)$$

The difference in density between a parcel undergoing an adiabatic and isohaline displacement, $\rho(\mathbf{x} + d\mathbf{x})_{\text{adiabatic/isohaline}}$, and the density of the ambient environment, $\rho(\mathbf{x} + d\mathbf{x})$, is thus given by

$$\rho(\mathbf{x} + d\mathbf{x}) - \rho(\mathbf{x} + d\mathbf{x})_{\text{adiabatic/isohaline}} = \rho[\Theta(\mathbf{x} + d\mathbf{x}), S(\mathbf{x} + d\mathbf{x}), p(\mathbf{x} + d\mathbf{x})] - \rho[\Theta(\mathbf{x}), S(\mathbf{x}), p(\mathbf{x} + d\mathbf{x})] \quad (2.14a)$$

$$= \rho d\mathbf{x} \cdot (-\alpha \nabla \Theta + \beta \nabla S), \quad (2.14b)$$

where the final equality ignores higher order terms in the Taylor series. If a parcel makes an adiabatic and isohaline excursion and finds itself in a region where the ambient density is unchanged, then there are no buoyancy forces to resist that displacement. Directions defined by such displacements are termed *neutral directions* (McDougall, 1987). By definition, neutral directions are orthogonal to the local dia-neutral unit vector

$$\hat{\gamma} = \left(\frac{-\alpha \nabla \Theta + \beta \nabla S}{|-\alpha \nabla \Theta + \beta \nabla S|} \right), \quad (2.15)$$

so that

$$\rho(\mathbf{x} + d\mathbf{x}) - \rho(\mathbf{x} + d\mathbf{x})_{\text{adiabatic/isohaline}} = (\rho d\mathbf{x} \cdot \hat{\gamma}) |-\alpha \nabla \Theta + \beta \nabla S|. \quad (2.16)$$

2.2.3 Squared buoyancy frequency

When measuring the gravitational stability of a fluid column, we are concerned with vertical displacements and the resistance from buoyancy stratification to such displacements. To anticipate the needs of the discrete calculation, we assume knowledge of the density, tracer concentration, and pressure at depths z and $z + dz$ (see Figure 2.2).

2.2.3.1 Stability to upward displacements from a deeper reference point

Consider first an upward displacement starting from the reference depth z and going to $z + dz$. Following the notation of Figure 2.2, we have

$$\rho(z + dz) - \rho(z + dz)_{\text{adiabatic/isohaline}} = \rho[\Theta(z + dz), S(z + dz), p(z + dz)] - \rho[\Theta(z), S(z), p(z + dz)]. \quad (2.17)$$

As for the case of a general displacement considered in Section 2.2.2, we perform a Taylor series expansion about the reference depth at z to render the leading order identity

$$\begin{aligned} \rho(z + dz) - \rho(z + dz)_{\text{adiabatic/isohaline}} &\approx \rho(z) dz \left[-\alpha(z) \left(\frac{\partial \Theta}{\partial z} \right) + \beta(z) \left(\frac{\partial S}{\partial z} \right) \right] \\ &= - \left(\frac{\rho dz}{g} \right) N^2. \end{aligned} \quad (2.18)$$

The final equality in equation (2.18) introduced the squared buoyancy frequency

$$N_{\text{linear}}^2 = g \left(\alpha \frac{\partial \Theta}{\partial z} - \beta \frac{\partial S}{\partial z} \right), \quad (2.19)$$

where the vertical derivatives and expansion coefficients are evaluated at the deep reference point z . Calculating gravitational stability according to the linear approximate expression (2.19) is accurate so long as all higher order terms in the Taylor series approximation can be neglected. It is for this reason we denote this a linear approximation to the buoyancy frequency. The higher order terms are potentially important

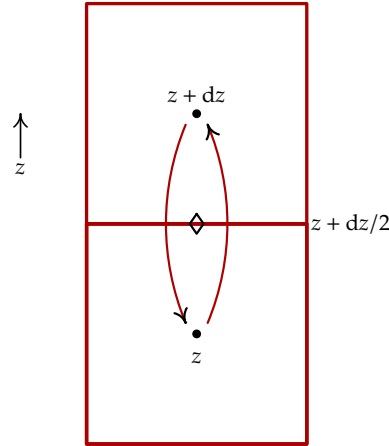


Figure 2.2: Illustration of how parcels are displaced when checking for the gravitational stability. As for the discrete column shown in Figure 2.1, we assume knowledge of the tracer and pressure values at the tracer points z and $z + dz$. Two displacements are considered: one vertically up and one vertically down. The notation corresponds on the discrete grid of Figure 2.1, where $z + dz$ in the present figure corresponds to an interface depth $zw(kw)$; the deeper point at z corresponds to the tracer point $zt(kt+1)$; and the shallower point $z + dz$ corresponds to the tracer point $zt(kt)$.

in regions where the equation of state becomes quite nonlinear, such as the high latitudes of the Southern Ocean. So we do not generally recommend the linear approximation for global modeling. Instead, we recommend use of the full squared buoyancy frequency

$$N_{\text{full}}^2(z \rightarrow z + dz) \equiv -\left(\frac{g}{dz}\right) \left(\frac{\rho(z + dz) - \rho(z + dz)_{\text{adiabatic/isohaline}}}{\rho(z)} \right) \quad (2.20)$$

Again, the calculation (2.20) will determine gravitational stability of an upward parcel displacement from depth z to $z + dz$. To further expose the physics of this calculation, consider two vertical stratifications.

- **GRAVITATIONALLY STABLE STRATIFICATION:** $N_{\text{FULL}}^2(z \rightarrow z + dz) > 0$: In this case, a vertically upward displacement occurring without heat or salt exchange will produce a parcel density that is more than the ambient density: $\rho(z + dz) - \rho(z + dz)_{\text{adiabatic/isohaline}} < 0$. This particular adiabatic and isohaline displacement is resisted by buoyancy forces. A displaced parcel will exhibit oscillatory motion with squared frequency $N_{\text{full}}^2(z \rightarrow z + dz)$ (see Section 2.9.1 of Vallis (2006)). The vertical density profile is thus gravitationally stable.
- **GRAVITATIONALLY UNSTABLE STRATIFICATION:** $N_{\text{FULL}}^2(z \rightarrow z + dz) < 0$: Now the upward adiabatic and isohaline displacement leads to a lesser density than the ambient environment: $\rho(z + dz) - \rho(z + dz)_{\text{adiabatic/isohaline}} > 0$. This particular adiabatic and isohaline displacement is encouraged by buoyancy forces to rise even further. The vertical density profile is thus gravitationally unstable.

2.2.3.2 Stability to downward displacements from a shallower reference point

We now determine the gravitational stability of fluid to displacements from a shallow reference point $z^* = z + dz$ downward to z , which requires the calculation

$$\begin{aligned}
 \rho(z) - \rho(z)_{\text{adiabatic/isohaline}} &= \rho[\Theta(z), S(z), p(z)] - \rho[\Theta(z + dz), S(z + dz), p(z)] \\
 &= \rho[\Theta(z^* - dz), S(z^* - dz), p(z)] - \rho[\Theta(z^*), S(z^*), p(z)] \\
 &\approx -\rho dz \left[-\alpha \left(\frac{\partial \Theta}{\partial z} \right) + \beta \left(\frac{\partial S}{\partial z} \right) \right] \\
 &= \left(\frac{\rho dz}{g} \right) N^2,
 \end{aligned} \tag{2.21}$$

where terms in the final two equalities are evaluated at the shallow reference point $z^* = z + dz$. Following equation (2.20), we introduce the full squared buoyancy frequency

$$N_{\text{full}}^2(z + dz \rightarrow z) \equiv \left(\frac{g}{dz} \right) \left(\frac{\rho(z) - \rho(z)_{\text{adiabatic/isohaline}}}{\rho(z + dz)} \right). \tag{2.22}$$

2.2.3.3 Combined displacements to approximate gravitational stability at interface depth

Let us summarize the two previous results. Again, we have two tracer points at depths z and $z + dz$. Gravitational stability can be probed in two separate ways. First we consider the deeper depth z as a reference point and displace parcels vertically upward to $z + dz$. This calculation leads to the squared buoyancy frequency at the reference point z

$$\begin{aligned}
 N_{\text{full}}^2(z \rightarrow z + dz) &= -\left(\frac{g}{dz} \right) \left(\frac{\rho(z + dz) - \rho(z + dz)_{\text{adiabatic/isohaline}}}{\rho(z)} \right) \\
 &= -\left(\frac{g}{dz} \right) \left(\frac{\rho[\Theta(z + dz), S(z + dz), p(z + dz)] - \rho[\Theta(z), S(z), p(z + dz)]}{\rho(z)} \right).
 \end{aligned} \tag{2.23}$$

We next the shallower depth $z + dz$ as a reference point and displace parcels vertically downward to z . This calculation leads to the squared buoyancy frequency at the reference point $z + dz$

$$\begin{aligned}
 N_{\text{full}}^2(z + dz \rightarrow z) &= \left(\frac{g}{dz} \right) \left(\frac{\rho(z) - \rho(z)_{\text{adiabatic/isohaline}}}{\rho(z + dz)} \right) \\
 &= \left(\frac{g}{dz} \right) \left(\frac{\rho[\Theta(z), S(z), p(z)] - \rho[\Theta(z + dz), S(z + dz), p(z)]}{\rho(z + dz)} \right).
 \end{aligned} \tag{2.24}$$

We now use these two results to render an approximation to the squared buoyancy frequency at the interface point $z + dz/2$, which is where the discrete calculation requires the stability to be estimated (Section 2.2.3.5). For this purpose, we take the average to yield an expression in terms of density differences

$$\begin{aligned}
 N_{\text{full}}^2(z + dz/2) &\equiv \frac{N_{\text{full}}^2(z \rightarrow z + dz) + N_{\text{full}}^2(z + dz \rightarrow z)}{2} \\
 &= -\frac{g}{2dz} \left(\frac{\rho[\Theta(z + dz), S(z + dz), p(z + dz)] - \rho[\Theta(z), S(z), p(z + dz)]}{\rho(z)} - \frac{\rho[\Theta(z), S(z), p(z)] - \rho[\Theta(z + dz), S(z + dz), p(z)]}{\rho(z + dz)} \right).
 \end{aligned} \tag{2.25}$$

As a sanity check, note that if the density is independent of pressure, and we replace densities in the denominator with the constant reference density ρ_o as commonly done for the Boussinesq approximation (see Section 2 of Roquet et al. (2014)), we have the familiar simplified result

$$N^2(z + dz/2) = -\frac{g}{dz} \left(\frac{\rho[\Theta(z + dz), S(z + dz)] - \rho[\Theta(z), S(z)]}{\rho_o} \right) \quad \text{density independent of pressure.} \tag{2.26}$$

2.2.3.4 Linear approximation: not recommended in general

Instead of computing the full buoyancy frequency in terms of density differences, one may choose to make a linearization of the expansion following equation (2.19), in which we write

$$N_{\text{linear}}^2(z + dz/2) \equiv \frac{N_{\text{linear}}^2(z) + N_{\text{linear}}^2(z + dz)}{2} = g \left(\bar{\alpha}^z \frac{\partial \Theta}{\partial z} - \bar{\beta}^z \frac{\partial S}{\partial z} \right), \quad (2.27)$$

where we introduced the vertical averaging operator to bring the expansion coefficients from the tracer point to the interface

$$\bar{\alpha}(z + dz/2) = \frac{\alpha(z) + \alpha(z + dz)}{2}. \quad (2.28)$$

The vertical tracer derivatives are naturally placed on the vertical cell interface. Contrary to the density difference approach of equation (2.25), the expression (2.27) requires no non-standard calculations of the equation of state. What it does require is calculation of the thermal expansion coefficients, with that calculation also used for neutral physics. So the expression (2.27) may be somewhat more computationally efficient. Nonetheless, when used as a measure of gravitational stability, the expression (2.25) makes less assumptions about our ability to truncate the Taylor series at the leading order. This truncation may become problematic particularly in high latitudes where the equation of state can become quite nonlinear. Hence, we generally do not recommend use of the linear expression (2.27) for the calculation of water column stability.

2.2.3.5 Discrete calculation of the squared buoyancy frequency

CVMix modules do *not* compute the buoyancy frequency. Rather, the calling model does and then passes N^2 to CVMix. Nonetheless, CVMix modules must assume a placement for the buoyancy frequency, with the following choice made:

CVMix modules assume the squared buoyancy frequency, N^2 , lives at the vertical interface of tracer cells, following the convention given by Figure 2.1.

We now write the buoyancy frequency expression (2.25) in terms of discrete indices for ready incorporation into a numerical model, in which we have

$$N^2(kw) = - \left(\frac{g}{2 dzw(kw)} \right) \left(\frac{\rho[\Theta(kt), S(kt), p(kt)] - \rho[\Theta(kt+1), S(kt+1), p(kt)]}{\rho(kt+1)} - \frac{\rho[\Theta(kt+1), S(kt+1), p(kt+1)] - \rho[\Theta(kt), S(kt), p(kt+1)]}{\rho(kt)} \right). \quad (2.29)$$

Note that by referring to Figures 2.1 and 2.2, we see that the discrete label kt corresponds to the shallower point $z+dz$, whereas $kt+1$ corresponds to the deeper point z . This correspondence is made when converting equation (2.25) to equation (2.29).

2.3 Gradient Richardson number

The gradient Richardson number measures the ratio of the stabilizing effects from buoyancy stratification to the destabilizing effects from vertical shear

$$Ri = \frac{N^2}{|\partial_z \mathbf{u}|^2}. \quad (2.30)$$

In this equation, N^2 is the squared buoyancy frequency, whose discrete calculation was detailed in Section 2.2.3.5. The denominator contains the squared vertical shear of the horizontal velocity, $|\partial_z \mathbf{u}|^2$. When the Richardson number is small, say below 1/4 as in Miles (1961), the flow tends toward a turbulent state

via production of Kelvin-Helmholz instabilities.¹ Consequently, many vertical mixing schemes make use of the Richardson number, such as the shear mixing schemes presented in Chapter 5. Additionally, the KPP boundary layer scheme (Chapter 8) makes use of a bulk Richardson number used to define properties of the surface planetary boundary layer (Section 8.5.7).

As for the squared buoyancy frequency N^2 , the CVMix modules do *not* compute a Richardson number, since details of this calculation depend on choices regarding the grid layout in the ocean model. Rather, the Richardson number is an input to CVMix modules. CVMix modules assume a placement for the Richardson number, with the following choice made:

The gradient Richardson number, Ri , is an input to CVMix modules. CVMix modules assume the gradient Richardson number lives at the vertical interface of tracer cells, following the convention given by Figure 2.1.

Staggering of tracer and velocity fields on a discrete grid leads to ambiguity for how to compute a discrete Richardson number. The issue is the squared buoyancy frequency in the numerator naturally lives at the vertical interface between tracer grids (Section 2.2.3.5), whereas the horizontal positioning for the denominator depends on the chosen horizontal staggering of velocity. We detail here some possible methods for the B-grid and C-grid. Unstructured grids used by MPAS-ocean require further considerations. Each grid involves averaging operations specific to the grid in order to compute the shear. There are even further methods available if we choose a different discrete placement of N^2 beyond that discussed in Section 2.2.3.5.

2.3.1 Considerations for the B-grid

Figure 2.3 illustrates the horizontal arrangement of prognostic model fields used with the B-grid. The B-grid places both horizontal prognostic velocity components at the same point, the corner of the tracer cell. This placement is natural when computing the Coriolis Force. However, it is unnatural for computation of advective tracer transport or the horizontal pressure gradient force acting on velocity. The need to perform an averaging operation when computing the horizontal pressure gradient leads to the computational mode associated with gravity waves on the B-grid (Mesinger (1973), Killworth et al. (1991), Pacanowski and Griffies (1999), Griffies et al. (2001), and Section 12.9 of Griffies (2004)).

We present here some methods for computing the squared vertical shear of the horizontal velocity on the B-grid, and thus methods for computing the Richardson number.

- **T-GRID AVERAGE OF U-GRID VELOCITY:** The first approach computes a horizontal average of the velocity field to place it onto the T-grid, and then computes the vertical derivative and its square. The 4-point horizontal average to compute a T-grid velocity is written

$$\mathbf{u}^T = \overline{\mathbf{u}}^{x,y}. \quad (2.31)$$

Note that this, and all, four point averages do *not* include land points. We next compute the squared vertical shear with the T-grid horizontal velocity for use in the Richardson number calculation

$$Ri^{(Ba)} = \frac{N^2}{\left| \frac{\partial \mathbf{u}^T}{\partial z} \right|^2}. \quad (2.32)$$

- **T-GRID AVERAGE OF U-GRID SHEAR:** A slight modification of the $Ri^{(Ba)}$ calculation takes the T-grid horizontal average of the U-grid shear

$$\left(\frac{\partial \mathbf{u}}{\partial z} \right)^T = \overline{\left(\frac{\partial \mathbf{u}}{\partial z} \right)^{x,y}}, \quad (2.33)$$

¹The critical Richardson number, below which instabilities are enabled, may need to be artificially set larger than the canonical 1/4 when considering discrete approximations to the velocity shear. The reason is that we are unable to precisely compute the vertical shear on a finite grid. See Section 4b of Jackson et al. (2008) for discussion.

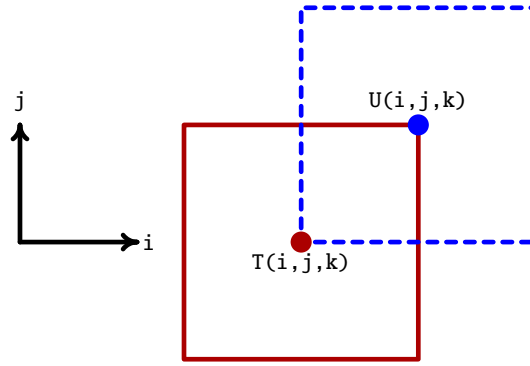


Figure 2.3: Illustration of how fields are placed on the horizontal B-grid using a *northeast convention*. Velocity points $U(i, j, k)$ are placed to the northeast of tracer points $T(i, j, k)$. Both horizontal velocity components $u_{i,j,k}$ and $v_{i,j,k}$ are placed at the velocity point $U(i, j, k)$. Both the tracer point and velocity point have a corresponding grid cell region, denoted by the solid and dashed squares.

and then computes the square so that

$$Ri^{(Bb)} = \frac{N^2}{\left| \left(\frac{\partial \mathbf{u}}{\partial z} \right)^T \right|^2}. \quad (2.34)$$

With uniform vertical grid spacing, the two Richardson number calculations are the same

$$Ri^{(Ba)} = Ri^{(Bb)} \quad \text{uniform vertical grid spacing.} \quad (2.35)$$

- **T-GRID AVERAGE OF SQUARED U-GRID SHEAR:** The third method computes the squared shear on the original U-grid, and then averages the squared shears onto the T-grid

$$\left(\left| \frac{\partial \mathbf{u}}{\partial z} \right|^2 \right)^T = \overline{\left(\left| \frac{\partial u}{\partial z} \right|^2 + \left| \frac{\partial v}{\partial z} \right|^2 \right)^{x,y}}, \quad (2.36)$$

so that

$$Ri^{(Bc)} = \frac{N^2}{\left(\left| \frac{\partial \mathbf{u}}{\partial z} \right|^2 \right)^T}. \quad (2.37)$$

2.3.2 Considerations for the C-grid

Figure 2.4 illustrates the horizontal arrangement of prognostic model fields used with the C-grid. The C-grid places the zonal velocity component on the zonal tracer cell face, and meridional velocity component on the meridional tracer cell face. This placement is suited for computation of advective tracer transport. It is also suited for computing the stress tensor and the horizontal pressure gradient force acting on velocity components. However, it is not natural for computation of the Coriolis Force. The need to perform an averaging operation to compute the Coriolis Force leads to the presence of a computational null mode associated with geostrophically balanced flow (Adcroft et al., 1999).

We present here some methods for computing the squared vertical shear of the horizontal velocity on the C-grid, and thus methods for computing the Richardson number.

- **T-GRID AVERAGE OF U,V-GRID VELOCITY COMPONENTS:** The first approach considered computes a horizontal average of the u, v velocity components to place both onto the T-grid, and then computes the

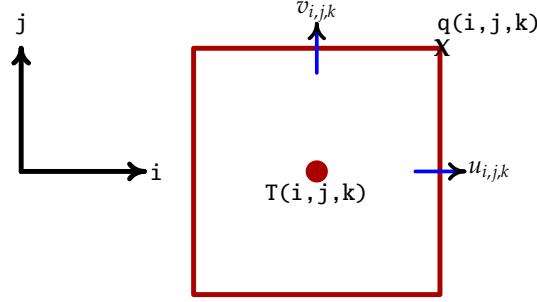


Figure 2.4: Illustration of how fields are placed on the horizontal C-grid. We illustrate here the convention that the zonal velocity component $u_{i,j,k}$ sits at the east face of the tracer cell $T(i, j)$, and the meridional velocity component $v_{i,j,k}$ sits at the north face of the tracer cell $T(i, j, k)$. This convention follows the *northeast* convention also used for the B-grid.

vertical derivative and its square. The horizontal averaging requires a two-point average so that

$$(u^\tau, v^\tau) = (\bar{u}^x, \bar{v}^y). \quad (2.38)$$

As for the B-grid averaging considered in Section 2.3.1, all averages considered here do *not* include land points. The squared vertical shear with the T-grid horizontal velocity is then used for the Richardson number calculation

$$\left| \frac{\partial \mathbf{u}^\tau}{\partial z} \right|^2 = \left(\frac{\partial \bar{u}^x}{\partial z} \right)^2 + \left(\frac{\partial \bar{v}^y}{\partial z} \right)^2 \quad (2.39)$$

$$\text{Ri}^{(\text{ca})} = \frac{N^2}{\left| \frac{\partial \mathbf{u}^\tau}{\partial z} \right|^2}. \quad (2.40)$$

- T-GRID AVERAGE OF U,V-GRID SHEAR: A slight modification of the $\text{Ri}^{(\text{ca})}$ calculation takes the T-grid horizontal average of the u,v-grid shear

$$\left(\frac{\partial \mathbf{u}}{\partial z} \right)^\tau = \left[\overline{\left(\frac{\partial u}{\partial z} \right)^x}, \overline{\left(\frac{\partial v}{\partial z} \right)^y} \right], \quad (2.41)$$

and then computes the square so that

$$\text{Ri}^{(\text{cb})} = \frac{N^2}{\left| \left(\frac{\partial \mathbf{u}}{\partial z} \right)^\tau \right|^2}. \quad (2.42)$$

With uniform vertical grid spacing, the two Richardson number calculations are the same

$$\text{Ri}^{(\text{ca})} = \text{Ri}^{(\text{cb})} \quad \text{uniform vertical grid spacing.} \quad (2.43)$$

- T-GRID AVERAGE OF SQUARED U,V-GRID SHEAR: The third method computes the squared shear on the original u,v-grid, and then averages the squared shears onto the T-grid

$$\left(\left| \frac{\partial \mathbf{u}}{\partial z} \right|^2 \right)^\tau = \overline{\left| \frac{\partial u}{\partial z} \right|^2}^x + \overline{\left| \frac{\partial v}{\partial z} \right|^2}^y \quad (2.44)$$

so that

$$\text{Ri}^{(\text{bc})} = \frac{N^2}{\left(\left| \frac{\partial \mathbf{u}}{\partial z} \right|^2 \right)^\tau}. \quad (2.45)$$

SAMPLE CHAPTER FOR CVMix

DOCUMENTATION

Contents

3.1	Introduction to the mixing scheme	17
3.2	Theory	18
3.3	Numerical implementation in CVMix	18
3.4	Further sections	18

This chapter provides a sample for what is useful to include in the CVMix documentation of a physical parameterization scheme. Clear and complete CVMix documentation is critical for the intelligent use of any scheme, so the author should focus on creating documentation that is useful and pedagogical. The following CVMix Fortran module is directly connected to the material in this chapter:

`cvmix_MODULE.F90`

Here are some suggestions for writing this document.

- Aim for a level of concise pedagogy, so that the reader will readily understand the scheme, but without going into too many details that are available in published literature. Some of the other CVMix chapters are good examples of this philosophy (e.g., tide mixing chapter [6](#)), though others are not (e.g., KPP chapter [8](#)).
- This chapter should describe any test cases available from the scheme, including sample figures. Test cases allow the new user to verify a particular implementation, and to provide a sample of how the physical parameterization works.
- Add new bibliography entries to the .bib file in the directory `cvmix_manual/references`.
- Figures associated with this document should ideally be named `new_scheme_figure_number.pdf` or the like, thus making it simpler to associate a figure with a chapter.

3.1 Introduction to the mixing scheme

This section provides a broad overview of the scheme, focusing on the scientific background and the processes available from the CVMix module.

3.2 Theory

This section develops the basic theory for the scheme, summarizing elements of the published literature in a manner that provides an intellectual foundation for the CVMix scheme. The reader should understand what the scheme aims to do from a physics perspective.

3.3 Numerical implementation in CVMix

This section develops the numerical implementation choices made for the CVMix implementation. Please include here a full description of options for using the scheme, as well as a list of parameters and their physical dimensions. Recommended usage and test cases can be presented here as well.

3.4 Further sections

The above template is clearly insufficient for some purposes. Feel free to modify as you see appropriate.

Chapter

4

STATIC BACKGROUND SCHEMES

Contents

4.1	Options for static background mixing coefficients	19
4.2	The profile from Bryan-Lewis (1979)	19

This chapter presents options in CVMix code for prescribing static (time independent) background diffusivities and viscosities. The following CVMix Fortran module is directly connected to the material in this chapter:

cvmix_background.F90

4.1 Options for static background mixing coefficients

[Jochum \(2009\)](#) describes the large sensitivities found in climate model simulations to the choice of background vertical diffusivities. There are various options in CVMix code for specifying a static background diffusivity and viscosity. These mixing coefficients are generally a function of space but remain the same value throughout the simulation, and so are independent of the flow state. These static values are primarily determined for tracer diffusivity, with a Prandtl number (ratio of diffusivity to viscosity) used to determine the background viscosity. A common choice for Prandtl number is 10, although for some background diffusivities there is no corresponding background viscosity (i.e., zero Prandtl number).

4.2 The profile from Bryan-Lewis (1979)

A classic choice for background diffusivity is that proposed by [Bryan and Lewis \(1979\)](#), which has an arctangent form with smaller values in the upper ocean and larger values beneath a pivot depth, originally set to 1500 m

$$\kappa_{\text{Bryan-Lewis}} = \text{vdc1} + \text{vdc2} \arctan[(|z| - \text{dpth}) \text{linv}]. \quad (4.1)$$

This is the form appearing in POP, where the parameters are defined as follows.

- vdc1 is the diffusivity (squared length per time) at $|z| = \text{dpth}$,
- vdc2 = amplitude of variation for the diffusivity (squared length per time)
- linv is an inverse length scale

- dpth is the vertical depth where the diffusivity equals vdc1 .

All lengths and diffusivities should be in MKS units. In many implementations, such as for GFDL-CM2.1, there is no corresponding Bryan-Lewis viscosity, so the corresponding Bryan-Lewis Prandtl number is zero. But more generally, the viscosity is computed according to a chosen Prandtl number.

In MOM5 and earlier versions of MOM, the form (4.1) is written in the somewhat more cumbersome manner for historical reasons

$$\kappa_{\text{Bryan-Lewis}} = \text{convert}(\text{afkph} + (\text{dfkph}/\pi) \arctan[\text{sfkph}(100|z| - \text{zfkph})]), \quad (4.2)$$

where afkph , dfkph , sfkph , and zfkph are tunable constants, and $\text{convert} = 1 \times 10^{-4} \text{ m}^2 \text{ s}^{-1}$ converts from the original CGS to MKS. The mapping between the MOM and POP forms (4.1) is given by the following

$$\text{vdc1} = \kappa_o \text{afkph} \quad (4.3)$$

$$\text{vdc2} = \kappa_o \text{dfkph}/\pi \quad (4.4)$$

$$\text{linv} = 100 \text{sfkph} \quad (4.5)$$

$$\text{dpth} = 100 \text{zfkph}. \quad (4.6)$$

We provide this mapping since Figure 4.1 was constructed using the original MOM-based form. Shown are two examples of vertical diffusivity profiles used in the GFDL-CM2.1 simulations (see Griffies et al., 2005, for discussion), with the values given by

$$\text{afkph} = 0.75 \quad (4.7)$$

$$\text{dfkph} = 0.95 \quad (4.8)$$

$$\text{sfkph} = 4.5 \times 10^{-5} \quad (4.9)$$

$$\text{zfkph} = 2500 \quad (4.10)$$

and for the equatorial region they are

$$\text{afkph} = 0.65 \quad (4.11)$$

$$\text{dfkph} = 1.15 \quad (4.12)$$

$$\text{sfkph} = 4.5 \times 10^{-5} \quad (4.13)$$

$$\text{zfkph} = 2500. \quad (4.14)$$

The original implementation from Bryan and Lewis (1979) chose the background as a function only of depth. However, the CM2.1 implementation shown in Figure 4.2 provides an exponential transition from the lower latitude form to the higher latitude form, with the transition latitude taken as 35° . In this way, the background diffusivity is a function of both latitude and depth. The resulting diffusivity is shown in Figure 4.2.

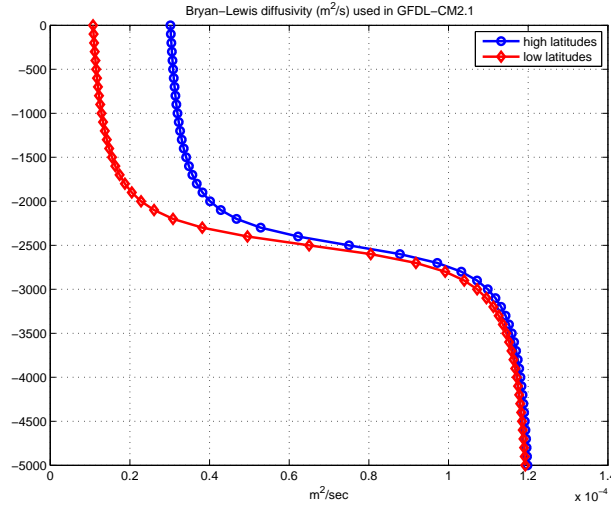


Figure 4.1: Sample vertical profiles for background diffusivities (in units of $\text{m}^2 \text{s}^{-1}$) given by the [Bryan and Lewis \(1979\)](#) functional form, as used by the OM3 ocean component of the GFDL-CM2.1 climate model ([Griffies et al., 2005](#)). The surface values in the tropics are $0.1 \times 10^{-4} \text{m}^2 \text{s}^{-1}$, whereas they are increased in the high latitudes to $0.3 \times 10^{-4} \text{m}^2 \text{s}^{-1}$. The Bryan-Lewis coefficients from equation (4.2) for the high latitudes are given by $\text{afkph} = 0.75$, $\text{dfkph} = 0.95$, $\text{sfkph} = 4.5 \times 10^{-5}$, $\text{zfkph} = 2500$, and for the equatorial region they are $\text{afkph} = 0.65$, $\text{dfkph} = 1.15$, $\text{sfkph} = 4.5 \times 10^{-5}$, $\text{zfkph} = 2500$.

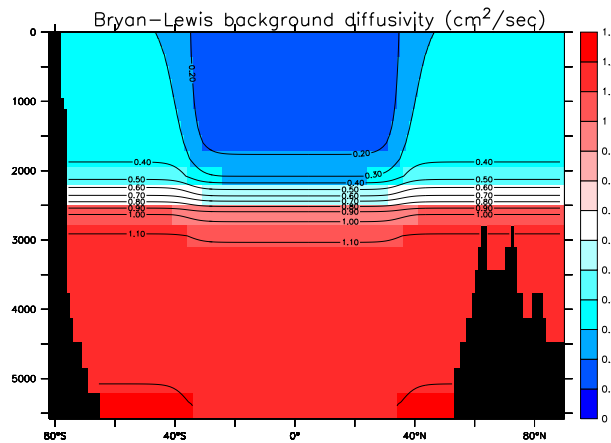


Figure 4.2: Shown here is the latitude dependent Bryan-Lewis diffusivity ($\text{cm}^2 \text{s}^{-1}$) based on values used in GFDL-CM2.1 configuration discussed in [Griffies et al. \(2005\)](#). The diffusivity is composed of the two profiles shown in Figure 4.1, with an exponential transition at 35° from the lower values in the tropics to the larger values in the high latitudes.

PARAMETERIZED SHEAR INDUCED MIXING

Contents

5.1	Mixing from shear instability	23
5.2	Pacanowski and Philander mixing	24
5.3	Richardson number mixing from Large et al. (1994)	24

In this chapter we detail the CVMix version of those parameterizations arising from shear induced mixing in stratified flows. The following CVMix Fortran module is directly connected to the material in this chapter:

cvmix_shear.F90

5.1 Mixing from shear instability

Shear induced mixing occurs when vertical shears in the horizontal velocity overcome the stabilizing effects from vertical buoyancy stratification. Shear instability is governed by the local or gradient Richardson number discussed in Section 2.3

$$Ri = \frac{N^2}{|\partial_z \mathbf{u}|^2}. \quad (5.1)$$

In this expression, N^2 is the squared buoyancy frequency detailed in Section 2.2. We assume throughout that the water is stably stratified, so that $N^2 > 0$. With $N^2 < 0$, one should set the diffusivity and viscosity to a large value to parameterize mixing associated with the gravitational instability.

The denominator in the Richardson number in equation (5.1) is the squared vertical shear of the horizontal velocity vector resolved by the model grid

$$|\partial_z \mathbf{u}|^2 = \left(\frac{\partial u}{\partial z} \right)^2 + \left(\frac{\partial v}{\partial z} \right)^2. \quad (5.2)$$

When the Richardson number is below a critical value, $Ri < Ri_c$, shear instabilities can grow to initiate turbulence, which in turn leads to enhanced mixing.

The canonical value of the critical gradient Richardson number is

$$Ri_c = 1/4 \quad \text{analytical value from shear layer instability.} \quad (5.3)$$

This value corresponds to the critical value for initiation of a Kelvin-Helmholz instability in a shear layer (Miles, 1961). However, as reviewed in Section 4b of Jackson et al. (2008), there are many reasons that 1/4

is not always the optimal value to use in numerical simulations. Thus, most schemes choose noticeably larger values, which allows for shear-induced mixing to be initiated in less unstable regions of the model's resolved flow.

5.2 Pacanowski and Philander mixing

An early form for parameterized shear mixing is that proposed by [Pacanowski and Philander \(1981\)](#), where their application focused on equatorial dynamics. They used a different viscosity, $\nu_{pp\ shear}$ and diffusivity, $\kappa_{pp\ shear}$. For gravitationally stable profiles (i.e., $N^2 > 0$), they chose

$$\nu_{pp\ shear} = \frac{\nu_0}{(1 + a Ri)^n} \quad (5.4)$$

$$\kappa_{pp\ shear} = \frac{\nu_0}{(1 + a Ri)^{n+1}}, \quad (5.5)$$

where ν_0 , a and n are adjustable parameters. Common settings used in POP are $a = 5$ and $n = 2$. Note that the Prandtl number is not constant using this prescription

$$Pr_{pp} = \frac{\nu_{pp\ shear}}{\kappa_{pp\ shear}} \quad (5.6a)$$

$$= 1 + a Ri. \quad (5.6b)$$

For gravitationally unstable profiles, the mixing coefficients are set to a large value, as in the shear mixing from [Large et al. \(1994\)](#) discussed in Section 5.3.

5.3 Richardson number mixing from [Large et al. \(1994\)](#)

For regions beneath the KPP boundary layer (see Figure 8.1), [Large et al. \(1994\)](#) and [Large and Gent \(1999\)](#) parameterized shear induced mixing using the following diffusivities

$$\kappa_{kpp\ shear} = \begin{cases} \kappa_0 & Ri < 0 \quad \text{gravitational instability regime} \\ \kappa_0 \left[1 - \left(\frac{Ri}{Ri_0} \right)^2 \right]^3 & 0 < Ri < Ri_0 \quad \text{shear instability regime} \\ 0 & Ri \geq Ri_0 \quad \text{stable regime.} \end{cases} \quad (5.7)$$

The form in the shear instability regime falls most rapidly near $Ri = 0.4 Ri_0$, which aims to parameterize the onset of shear instability. In this neighborhood, rapid changes in Ri can cause gravitational instabilities to develop in the vertical, but these are largely controlled by vertically smoothing Ri profiles with a 1 – 2 – 1 smoother. Unlike [Pacanowski and Philander \(1981\)](#), [Large et al. \(1994\)](#) chose a unit Prandtl number for shear induced mixing; i.e., the shear induced viscosity is the same as the shear induced diffusivity

$$Pr_{kpp} = \frac{\nu_{kpp\ shear}}{\kappa_{kpp\ shear}} \quad (5.8a)$$

$$= 1. \quad (5.8b)$$

ENERGETICALLY BASED MIXING SCHEMES FROM TIDAL DISSIPATION

Contents

6.1	Introduction to tidal induced mixing	25
6.2	Energetic elements of tide mixing parameterizations	26
6.2.1	Bottom drag	26
6.2.2	Wave drag from breaking internal gravity waves	27
6.2.3	Relating dissipation to mixing via Osborn (1980)	27
6.2.4	Vertical deposition function	28
6.2.5	Local versus non-local wave energy dissipation	28
6.2.6	Prandtl number	29
6.2.7	General form of the vertical diffusivity	29
6.2.8	Energetic balances	29
6.3	The Simmons et al. (2004) scheme	30
6.3.1	Calculation of the wave energy dissipation	30
6.3.2	Deposition function	31
6.3.3	Regularization of the diffusivity	31
6.3.4	Regarding a shallow depth cutoff	32
6.3.5	Further comments	32

This chapter summarizes the CVMix implementation of the parameterized vertical mixing associated with mechanical energy dissipation from tidal motions in both the ocean interior and near the bottom. The following CVMix Fortran module is directly connected to the material in this chapter:

`cvmix_tidal.F90`

6.1 Introduction to tidal induced mixing

Mixing arises when mechanical energy dissipates at the small scales in the presence of a nonzero gradient of tracer and/or momentum. There are two sources of mechanical energy dissipation considered in this chapter.

- **INTERNAL WAVES IN OCEAN INTERIOR:** Breaking internal gravity waves arise when barotropic tidal flow is scattered into internal tidal energy. This process occurs when astronomical tides interact with rough bottom topography.
- **TIDAL WAVES INTERACTING WITH CONTINENTAL SHELVES:** Frictional bottom drag is enhanced as tides encounter continental shelves (whose depths are generally 500 m or less). There is an associated mixing of water masses due to this dissipation.

To resolve both of these dissipation processes explicitly in a numerical model requires grid resolution no coarser than meters in the vertical (throughout the water column), and 1-10 kilometers in the horizontal. This very fine resolution is not generally accessible to global climate models, so it is necessary to consider a parameterization.

CVMix has implementations for the following tide mixing parameterizations.

- **BAROCLINIC OR INTERNAL WAVE MIXING:** [Simmons et al. \(2004\)](#) presented the first implementation in an ocean climate model of an internal tide mixing parameterization. [Jayne \(2009\)](#) followed with an updated implementation. A more recent study by [Melet et al. \(2013\)](#) implemented the ideas from [Polzin \(2009\)](#) to remove the arbitrariness of the vertical deposition function used by [Simmons et al. \(2004\)](#) and [Jayne \(2009\)](#). Any of these schemes aim to provide a physically based replacement for the static vertical diffusivity of [Bryan and Lewis \(1979\)](#) (Chapter 4).

Although CVMix provides an optional Prandtl number, it is general practice to assume a unit Prandtl number for each of the tide parameterization schemes.¹

6.2 Energetic elements of tide mixing parameterizations

We now consider elements of how energetic based tide mixing parameterizations are formulated.

6.2.1 Bottom drag

Frictional bottom drag is typically parameterized as

$$\mathbf{D}_{\text{bottom drag}} = C_D \mathbf{u} |\mathbf{u}| \quad (\text{units of } \text{m}^2 \text{ s}^{-2}), \quad (6.1)$$

where C_D is a dimensionless drag coefficient with a value on the order of

$$C_D \approx 2 \times 10^{-3}. \quad (6.2)$$

Energy dissipation associated with this bottom drag is given by

$$E_{\text{bottom drag}} = \rho_o \mathbf{u} \cdot \mathbf{D}_{\text{bottom drag}} = \rho_o |\mathbf{u}|^3 \quad (\text{units of } \text{W m}^{-2}), \quad (6.3)$$

where ρ_o is a reference ocean density.

A component to the energy dissipation (6.3) is associated with barotropic tides as they encounter the ocean bottom, particularly continental shelves and other shallow ocean regions. In an ocean model that does not represent the astronomical tides, we may choose to enhance the model's bottom velocity through a root-mean-square tidal speed, U_{tide} , so that the bottom drag takes the form

$$\mathbf{D}_{\text{bottom drag}} = C_D \mathbf{u} \left(\mathbf{u}^2 + U_{\text{tide}}^2 \right)^{1/2}, \quad (6.4)$$

where now the velocity \mathbf{u} refers to the model's resolved bottom velocity field. The modified energy dissipation from bottom drag thus takes the form

$$E_{\text{bottom drag}} = \rho_o C_D \mathbf{u}^2 \left(\mathbf{u}^2 + U_{\text{tide}}^2 \right)^{1/2}. \quad (6.5)$$

The tidal speed U_{tide} may be a prescribed global constant, as in the OCCAM simulations from [Webb et al. \(1998\)](#). It may instead be a map determined by an offline tide model, as in [Jayne and St.Laurent \(2001\)](#). Or, it may be computed online by periodically running a tide model during the update of the primitive equation ocean model.

¹The Prandtl number is the ratio of viscosity to diffusivity.

6.2.2 Wave drag from breaking internal gravity waves

A drag associated with breaking internal gravity waves was written by [Jayne and St.Laurent \(2001\)](#) as

$$\mathbf{D}_{\text{wave drag}} = (1/2)N_{\text{bott}}\kappa_{\text{topo}}h_{\text{topo}}^2\mathbf{u} \quad (\text{units of m}^2\text{ s}^{-2}), \quad (6.6)$$

where N_{bott} is the buoyancy frequency at the ocean bottom, and $(\kappa_{\text{topo}}, h_{\text{topo}})$ are wavenumber (dimensions of inverse length) and amplitude (dimensions of length) scales for the topography. The product $\kappa_{\text{topo}}h_{\text{topo}}^2$ has dimensions of length and defines a *roughness length*

$$L_{\text{rough}} = \kappa_{\text{topo}}h_{\text{topo}}^2 \quad (6.7)$$

to be specified according to statistics of the observed ocean bottom topography. The internal wave drag can thus be written as

$$\mathbf{D}_{\text{wave drag}} = (1/2)N_{\text{bott}}L_{\text{rough}}\mathbf{u} \quad (\text{units of m}^2\text{ s}^{-2}). \quad (6.8)$$

The energy dissipation associated with breaking internal gravity waves is given by

$$\begin{aligned} E_{\text{wave drag}} &= \rho_o \langle \mathbf{u} \cdot \mathbf{D}_{\text{wave drag}} \rangle \\ &= (\rho_o/2)N_{\text{bott}}L_{\text{rough}}\langle \mathbf{u}^2 \rangle \quad (\text{units of W m}^{-2}). \end{aligned} \quad (6.9)$$

In the [Jayne and St.Laurent \(2001\)](#) paper, they emphasize that κ_{topo} , which sets the roughness length through $L_{\text{rough}} = \kappa_{\text{topo}}h_{\text{topo}}^2$, is used as a tuning parameter, with the tide model tuned to give sea level values agreeing with observations. Then, the energy dissipation can be diagnosed from the tide model.

As with the bottom drag (Section 6.2.1), the wave energy dissipation arises from energy removed from the barotropic tides, yet here it is transferred into baroclinic tides. Some of the energy transferred into the baroclinic tides dissipates locally due to local wave breaking, and this dissipation then leads to enhanced local mixing. The remaining baroclinic energy propagates away; i.e., it is non-local. The ratio of local to non-local energy is not well known, and is the focus of research.

6.2.3 Relating dissipation to mixing via [Osborn \(1980\)](#)

Mixing occurs when mechanical energy is dissipated in the presence of stratification. The relation between energy dissipation and mixing is not known from first principles, so we consider dimensional arguments to establish a useful form. Since we are concerned with vertical mixing, we assume that diffusivity is inversely proportional to the vertical stratification, with stratification strength measured by the buoyancy frequency, N^2 (see Section 2.2.3). Mechanical energy per mass has units of $\text{m}^2\text{ s}^{-2} = \text{J kg}^{-1}$, and the dissipation of this energy, written as ϵ , has units of $\text{m}^2\text{ s}^{-3} = \text{W kg}^{-1}$

$$\epsilon = \text{mechanical energy dissipation in units of m}^2\text{ s}^{-3} = \text{W kg}^{-1}. \quad (6.10)$$

Together, the energy dissipation and buoyancy frequency define a diffusivity given through the relation ([Osborn, 1980](#))

$$\kappa_{\text{dissipate}} = \frac{\Gamma\epsilon}{N^2}, \quad (6.11)$$

where the dimensionless parameter Γ measures the efficiency that mechanical energy dissipation translates into mixing that can be parameterized by a diffusivity acting on vertical stratification. This relation converts measurements of mechanical energy dissipation into a diffusivity.

The efficiency parameter in equation (6.11) is often chosen as

$$\Gamma = 0.2 \quad (6.12)$$

based measurements ([Osborn, 1980](#); [Ivey and Imberger, 1991](#)). However, in regions of very weak vertical stratification, where $N^2 \rightarrow 0$, we suggest following [Melet et al. \(2013\)](#), in which the mixing efficiency tends to zero according to

$$\Gamma = 0.2 \left(\frac{N^2}{N^2 + \Omega^2} \right) \quad (6.13)$$

where

$$\begin{aligned}\Omega &= \left(\frac{2\pi + 2\pi/365.24}{86400\text{s}} \right) \\ &= \left(\frac{\pi}{43082} \right) \text{s}^{-1} \\ &= 7.2921 \times 10^{-5} \text{s}^{-1}\end{aligned}\tag{6.14}$$

is the angular rotation rate of the earth about its axis and about the sun. This modified mixing efficiency reduces the regions where spuriously large values of diffusivity may occur, especially next to the bottom, where low values of N^2 may appear. There is little physical reason to believe the huge diffusivities diagnosed from regions with $N^2 < \Omega^2$.

6.2.4 Vertical deposition function

We are generally concerned in this chapter with mixing induced by energy dissipation that is largest near the bottom. This bottom intensified dissipation leads to the largest levels of mixing also near the bottom. Yet there are means for dissipation to move upwards into the water column, and it is this mixing that generally has far more impact on the ocean stratification. Details of how dissipation moves upwards into the column remains a topic of research. We present here a formulation followed by the CVMix implementations of the [Simmons et al. \(2004\)](#) and [Melet et al. \(2013\)](#) schemes. In this case, we write the energy dissipation in the form

$$\epsilon = \mathcal{E} F(z),\tag{6.15}$$

where \mathcal{E} is an energy dissipation times a length scale, and $F(z)$ is a vertical deposition function with units of inverse length. Both [Simmons et al. \(2004\)](#) and [Melet et al. \(2013\)](#) chose

$$\mathcal{E} = \frac{q E_{\text{wave drag}}(x, y)}{\rho},\tag{6.16}$$

where $E_{\text{wave drag}}(x, y)$ is the energy input to wave drag originating from the bottom (equation (6.9)), ρ is the *in situ* density, and q is the dimensionless fraction of energy that dissipates locally rather than propagating away to dissipate non-locally. We have more to say on q in Section 6.2.5. The vertical deposition function is assumed to integrate to unity over an ocean column

$$\int_{-H}^{\eta} F(z) dz = 1.\tag{6.17}$$

[Simmons et al. \(2004\)](#) chose an empirical exponential function (equation (6.26)) for $F(z)$, whereas [Melet et al. \(2013\)](#) based their choice on theoretical results from [Polzin \(2009\)](#).

6.2.5 Local versus non-local wave energy dissipation

The dimensionless parameter, q , introduced in equation (6.16) measures the fraction of wave energy dissipated locally, and thus contributes to local mixing. [Simmons et al. \(2004\)](#) and [Melet et al. \(2013\)](#) both chose

$$q = 1/3\tag{6.18}$$

based on the work of [St.Laurent et al. \(2002\)](#). The remaining 2/3 of the wave energy propagates away and is assumed to dissipate non-locally. The non-local dissipation of internal tidal energy, as well as the dissipation of internal energy from other sources (e.g., wind energy), are accounted for in an *ad hoc* manner via the background diffusivity κ_0 (and background viscosity). A value within the range

$$\kappa_0 = (0.1 - 0.2) \times 10^{-4} \text{m}^2 \text{s}^{-1}\tag{6.19}$$

is recommended based on the measurements of [Ledwell et al. \(1993\)](#). Other choices are considered in Chapter 4.

Setting $q = 1/3$ globally is strictly incorrect for internal gravity wave dissipation. The actual value is related to the modal content of the excited internal tide, which is related to the roughness spectrum of topography. The redder the mode/roughness spectrum, the lower q . For example, Hawaii has been modelled as a knife-edge by [St.Laurent et al. \(2003\)](#). This topography excites predominantly low modes, and these modes are stable, propagate quickly, and have long interaction times. That is, they propagate to the far field. [Klymak et al. \(2005\)](#) argue that $q = 0.1$ for Hawaii from the Hawaiian Ocean Mixing Experiment (HOME) data. For the mid-Atlantic ridge, the use of $q = 1/3$, as in [Simmons et al. \(2004\)](#) and [Melet et al. \(2013\)](#), may be more suitable. In contrast, the bottom mixing scheme from [Legg et al. \(2006\)](#) in effect assume

$$q = 1 \quad \text{bottom mixing scheme,} \quad (6.20)$$

which is sensible given that the mixing they considered occurs predominantly within a bottom boundary layer.

6.2.6 Prandtl number

The Prandtl number is the ratio of viscosity to diffusivity. [Simmons et al. \(2004\)](#) do not discuss vertical viscosity in their study. If one considers a non-zero Prandtl number, then vertical viscosity is enhanced along with the diffusivity when considering internal wave breaking. The following are examples of the Prandtl number chosen for the tide mixing parameterizations.

- The earth system models of [Dunne et al. \(2012\)](#) assume a unit Prandtl number for mixing related to tide mixing.
- [Jayne \(2009\)](#), as well as the released version of CESM, chose a Prandtl number of 10 for the tidal mixing scheme (see page 1759 of [Jayne \(2009\)](#)). The only exception is when vertical stratification goes to zero, in which case the Prandtl number is set to unity, consistent with the KPP implementation (in CESM) of convective mixing.

6.2.7 General form of the vertical diffusivity

The previous considerations lead to the following general form for a diffusivity arising from mechanical energy dissipation that originates from the ocean bottom

$$\kappa_{\text{dissipate}} = \frac{\Gamma \epsilon_{\text{dissipate}}}{N^2} \quad (6.21a)$$

$$= \frac{\Gamma \mathcal{E}_{\text{dissipate}} F(z)}{N^2} \quad (6.21b)$$

$$= \frac{q \Gamma E_{\text{dissipate}}(x, y) F_{\text{dissipate}}(z)}{\rho N^2}. \quad (6.21c)$$

The energy dissipation at the ocean bottom, $E_{\text{dissipate}}(x, y)$, and the vertical deposition function, $F_{\text{dissipate}}(z)$, distinguish the schemes considered by [Simmons et al. \(2004\)](#) and [Melet et al. \(2013\)](#).

6.2.8 Energetic balances

One of the main reasons to formulate diffusivities based on mechanical energy input is that this energy is exchanged in a conservative manner within the ocean. This conservation then leads to self-consistency tests for the model implementation of various energy-based mixing parameterizations. We consider here in particular the work done against stratification by vertical diffusion with a diffusivity $\kappa_{\text{dissipate}}$, with this work given by

$$\mathcal{P} \equiv \int \kappa_{\text{dissipate}} \rho N^2 dV. \quad (6.22)$$

Use of equation (6.25) for the vertical diffusivity with a constant mixing efficiency $\Gamma = 0.2$ yields

$$\mathcal{P} = \int \kappa_{\text{dissipate}} \rho N^2 dV \quad (6.23a)$$

$$= q\Gamma \int E_{\text{dissipate}}(x, y) dx dy, \quad (6.23b)$$

assuming $q\Gamma$ constant. Note that to reach this result, we set $\int F_{\text{dissipate}}(z) dz = 1$ (Section 6.2.4), which is a constraint that is maintained by the CVMix implementation of the energetic-based mixing schemes. Equation (6.23) says that the energy from some form of dissipation mechanism is deposited in the ocean interior and works against stratification.

For the more general case of $q\Gamma$ spatially dependent, we have the balance

$$\mathcal{P} = \int \kappa_{\text{dissipate}} \rho N^2 dV \quad (6.24a)$$

$$= \int q\Gamma E_{\text{dissipate}}(x, y) F_{\text{dissipate}}(z) dV, \quad (6.24b)$$

which again is a statement of energy conservation between wave dissipation and mixing of density. Although equation (6.24) is a trivial identity following from the definition of the closure, it is not trivial to maintain in the ocean model. The main reason is that we work with diffusivities when integrating the tracer equations in an ocean model, and these diffusivities are often subjected to basic numerical consistency criteria, such as the following.

- We may wish to have the diffusivities monotonically decay upwards in the column. Given the N^{-2} dependence of the diffusivity in equation (6.21), monotonicity is not guaranteed. Without an added monotonicity constraint, the simulation can be subject to spurious instabilities in which intermediate depths become weakly stratified through some mixing, which in turn produces even larger diffusivities to further reduce the stratification. Jayne (2009) discovered this behaviour in his simulations with POP.
- The diffusivities should be bounded by a reasonable number, such as $50 - 100 \text{ cm}^2 \text{ sec}^{-1}$.

Imposing constraints such as these on the diffusivity corrupts the identity (6.23). In general, the constraints remove energy from the interior, so that in practice $\int \kappa_{\text{dissipate}} \rho N^2 dV < \int q\Gamma E_{\text{dissipate}}(x, y) dV$.

6.3 The Simmons et al. (2004) scheme

To account for mixing associated with energy dissipation from breaking internal gravity waves, Simmons et al. (2004) propose a diffusivity given by

$$\kappa_{\text{simmons}} = \frac{\Gamma \epsilon_{\text{wave drag}}}{N^2} \quad (6.25a)$$

$$= \frac{\Gamma \mathcal{E}_{\text{wave drag}} F_{\text{simmons}}(z)}{N^2} \quad (6.25b)$$

$$= \frac{q\Gamma E_{\text{wave drag}}(x, y) F_{\text{simmons}}(z)}{\rho N^2}, \quad (6.25c)$$

which again is the general form introduced in Section 6.2.7. To reach this result, we used equation (6.15) to introduce the vertical deposition function F_{simmons} , and equation (6.16) to introduce the wave drag energy dissipation, $E_{\text{wave drag}}$, given by equation (6.9).

6.3.1 Calculation of the wave energy dissipation

The wave energy dissipation, $E_{\text{wave drag}}$, is evaluated as follows.

- N_{bott} is computed from the model's evolving buoyancy frequency at the top face of a bottom boundary layer (often just the bottom-most tracer cell). Note that the buoyancy frequency at the bottom face of the bottom-most cell is zero, by definition.
- The effective roughness length $L_{\text{rough}} = \kappa_{\text{topo}} h_{\text{topo}}^2$ requires an algorithm to compute h_{topo} from observed bottom topography, and tide model to tune κ_{topo} . However, in practice what can be done is to take h_{topo} given some variance of topography within a grid cell, and then tune $E_{\text{wave drag}}$ to be roughly 1TW in ocean deeper than 1000m, with κ_{topo} as the tuning parameter.

6.3.2 Deposition function

The bottom intensified vertical profile, or deposition function, is taken as

$$F_{\text{simmons}}(z) = \frac{e^{-(d-h)/\zeta}}{\zeta(1 - e^{-d/\zeta})} \quad (6.26a)$$

$$= \frac{e^{h/\zeta}}{\zeta(e^{d/\zeta} - 1)} \quad (6.26b)$$

$$= e^{-z/\zeta} \left(\frac{e^{\eta/\zeta}}{\zeta(e^{d/\zeta} - 1)} \right). \quad (6.26c)$$

In this expression,

$$d = H + \eta \quad (6.27)$$

is the time dependent thickness of water between the free surface at $z = \eta$ and the ocean bottom at $z = -H$, and

$$h = -z + \eta \quad (6.28)$$

is the time dependent distance from the free surface to a point within the water column.² The chosen form of the deposition function is motivated by the microstructure measurements of [St.Laurent et al. \(2001\)](#) in the abyssal Brazil Basin, and the continental slope measurements of [Moum et al. \(2002\)](#). This profile respects the observation that mixing from breaking internal gravity waves, generated by scattered barotropic tidal energy, is exponentially trapped within a distance ζ from the bottom. An *ad hoc* decay scale of

$$\zeta = 500 \text{ m} \quad (6.29)$$

is suggested by [Simmons et al. \(2004\)](#) for use with internal gravity wave breaking in the abyssal ocean.

6.3.3 Regularization of the diffusivity

The diffusivities resulting from this parameterization can reach levels upwards of the maximum around $20 \times 10^{-4} \text{ m}^2 \text{ s}^{-1}$ seen in the [Polzin et al. \(1997\)](#) results. Due to numerical resolution issues, the scheme can in practice produce even larger values. We need to consider the physical relevance of these large values. The following lists some options that the modeller may wish to exercise.

- We may choose to limit the tide-induced diffusivity to be no larger than a maximum value, defaulted to $0.005 \text{ m}^2 \text{ s}^{-1}$ in CVMix. In contrast, [Jayne \(2009\)](#) set a maximum diffusivity at $0.1 \text{ m}^2 \text{ s}^{-1}$, which perhaps led to problems with his implementation.
- Based on observations, the mechanical energy input from wave drag (equation (6.9)) should not exceed roughly 0.1 W m^{-2} at a grid point (Bob Hallberg, personal communication 2008). Depending on details of the bottom roughness and tide velocity amplitude, a typical model implementation may easily exceed this bound. Hence, it may be necessary to cap the mechanical energy input to be no larger than a set bound.
- Use of the stratification dependent mixing efficiency (6.13) provides a physically based means to regularize the regions where N^2 can get extremely small.

²We emphasize that with a free surface, d and h are generally time dependent. Furthermore, with general vertical coordinates, h is time dependent for all grid cells. See Section 2.1 for details.

6.3.4 Regarding a shallow depth cutoff

[Simmons et al. \(2004\)](#) do not apply their scheme in waters with ocean bottom shallower than 1000m, whereas [Jayne \(2009\)](#) applies the scheme for all depths. CVMix has a namelist that allows for setting a cutoff depth, with the cutoff defaulted to 0m, thus allowing for the scheme to operate over all ocean regions. In principle, there is nothing wrong with using the [Simmons et al. \(2004\)](#) scheme all the way to shallow waters, and removing the somewhat arbitrary depth cutoff is more satisfying. So one may wish to naively use $q = 1/3$ without a 1000m depth cutoff.

Likewise, $\zeta = 500\text{m}$ globally may be a reasonable choice. The structure function will properly integrate to unity, whether or not the ocean depth H is greater or less than ζ .

6.3.5 Further comments

Here are some further points to consider for this scheme.

- One means to ensure that the diffusivities are within a reasonable bound, without capping them after their computation, is to artificially restrict the stratification used in the calculation to be no less than a certain number. [Simmons et al. \(2004\)](#) chose the floor value $N^2 \geq 10^{-8} \text{s}^{-2}$. There is a great deal of sensitivity to the floor value used. GFDL practice is to keep the floor value quite low so that $N_{\min}^2 < \Omega^2$. CVMix does not provide an option for setting this floor.
- If the maximum diffusivity realized by the scheme is allowed to be very large, say much greater than as $1000 \text{cm}^2 \text{sec}^{-1}$, then the near bottom stratification can become very small. In this case, $E_{\text{wave drag}}$ can dip below the canonical 1TW value. This process resembles a negative feedback in some manner, though it has not been explored extensively.
- [Simmons et al. \(2004\)](#) chose a tidal energy data set between 72°S and 72°N (polar regions had no tidal forcing and just used a constant background mixing). In contrast, [Jayne \(2009\)](#) used a global data set.

DOUBLE DIFFUSION

Contents

7.1	Introduction to mixing from double diffusive processes	33
7.2	Salt fingering regime	34
7.3	Diffusive convective regime	34

This chapter details the parameterization of mixing from double diffusive processes. The following CVMix Fortran module is directly connected to the material in this chapter:

cvmix_ddiff.F90

7.1 Introduction to mixing from double diffusive processes

Double diffusion processes ([Schmitt, 1994](#)) have the potential to significantly enhance vertical diffusivities. The key stratification parameter of use for double diffusive processes is

$$R_\rho = \frac{\alpha}{\beta} \left(\frac{\partial \Theta / \partial z}{\partial S / \partial z} \right), \quad (7.1)$$

where the thermal expansion coefficient is given by

$$\alpha = -\frac{1}{\rho} \left(\frac{\partial \rho}{\partial \Theta} \right), \quad (7.2)$$

and the haline contraction coefficient is

$$\beta = \frac{1}{\rho} \left(\frac{\partial \rho}{\partial S} \right). \quad (7.3)$$

Note that the effects from double diffusive processes on viscosity are ignored in CVMix for two reasons:

- The effects on viscosity are not well known.
- For most applications, the vertical Prandtl number is larger than unity (often 10) for background viscosities (Chapter 4), so that modifying the vertical viscosity according to double diffusion will not represent a sizable relative impact.

There are two regimes of double diffusive processes, with the parameterization different in the regimes. We now detail how CVMix parameterizes vertical mixing in these two regimes.

7.2 Salt fingering regime

The salt fingering regime occurs when salinity is destabilizing the water column (salty above fresh water) and when the stratification parameter R_ρ is within a particular range:

$$\frac{\partial S}{\partial z} > 0 \quad (7.4)$$

$$1 < R_\rho < R_\rho^0 = 2.55. \quad (7.5)$$

The parameterized vertical diffusivity in this regime is fit to observational estimates given by [Laurent and Schmitt \(1999\)](#), who propose the following form

$$\kappa_d = \kappa_d^0 \left[1 - \frac{R_\rho - 1}{R_\rho^0 - 1} \right]^3. \quad (7.6)$$

The default values for the parameter κ_d^0 are set to

$$\kappa_d^0 = \begin{cases} 1 \times 10^{-4} \text{ m}^2 \text{ s}^{-1} & \text{for salinity and other tracers} \\ 0.7 \times 10^{-4} \text{ m}^2 \text{ s}^{-1} & \text{for temperature.} \end{cases} \quad (7.7)$$

7.3 Diffusive convective regime

Diffusive convective instability occurs where the temperature is destabilizing (cold above warm) and with $0 < R_\rho < 1$

$$\frac{\partial \Theta}{\partial z} < 0 \quad (7.8)$$

$$0 < R_\rho < 1. \quad (7.9)$$

For temperature, the vertical diffusivity used in [Large et al. \(1994\)](#) is given by

$$\kappa_d = \nu_{\text{molecular}} \times 0.909 \exp\left(4.6 \exp\left[-.54\left(R_\rho^{-1} - 1\right)\right]\right), \quad (7.10)$$

where

$$\nu_{\text{molecular}} = 1.5 \times 10^{-6} \text{ m}^2 \text{ s}^{-1} \quad (7.11)$$

is the molecular viscosity of water. Multiplying the diffusivity (7.10) by the factor

$$\text{factor} = \begin{cases} (1.85 - 0.85 R_\rho^{-1}) R_\rho & 0.5 \leq R_\rho < 1 \\ 0.15 R_\rho & R_\rho < 0.5, \end{cases} \quad (7.12)$$

gives the diffusivity for salinity and other tracers.

KPP SURFACE OCEAN BOUNDARY LAYER

Contents

8.1	Elements of the K-profile parameterization (KPP)	37
8.1.1	Conventions	37
8.1.2	General form of the KPP parameterization	39
8.1.3	The vertical diffusivity	39
8.1.3.1	Boundary layer thickness	40
8.1.3.2	Measuring vertical distances within the OBL	40
8.1.3.3	Scale for turbulent vertical velocity fluctuations w_λ	41
8.1.3.4	Non-dimensional vertical shape function $G_\lambda(\sigma)$	42
8.1.4	The non-local transport γ_λ	42
8.1.5	Some caveats regarding KPP	44
8.2	Surface ocean boundary momentum fluxes	44
8.3	Surface ocean boundary buoyancy fluxes	45
8.3.1	General features of buoyancy forcing	45
8.3.2	Scalar budgets for a surface ocean model grid cell	46
8.3.3	Salt fluxes from sea ice melt and formation	47
8.3.4	Salt and heat fluxes associated with water transport	47
8.3.5	Non-penetrative surface heat fluxes	47
8.3.5.1	Longwave radiation	47
8.3.5.2	Latent heat fluxes	48
8.3.5.3	Sensible heat fluxes	48
8.3.6	The case of frazil	48
8.3.7	Penetrative shortwave radiation	49
8.3.8	Buoyancy budget for a surface ocean model grid cell	49
8.3.9	Surface boundary terms contributing to buoyancy evolution	50
8.3.9.1	Heat carried by water transport	50
8.3.9.2	Penetrative radiation	50
8.3.9.3	Non-penetrative heating	51
8.3.9.4	Salt carried by water transport	51
8.3.9.5	Salt fluxes due to sea ice melt or formation	51
8.3.10	Buoyancy forcing that acts on the OBL	51
8.4	Surface layer and Monin-Obukhov similarity	52
8.4.1	The surface layer	52
8.4.2	Monin-Obukhov similarity theory	52
8.4.3	Similarity functions and Monin-Obukhov length scale	54

8.5	Specifying the KPP parameterization	56
8.5.1	The turbulent vertical velocity scale w_λ	56
8.5.1.1	Velocity scale w_λ with stable buoyancy forcing	56
8.5.1.2	Velocity scale w_λ with unstable buoyancy forcing	57
8.5.1.3	Summarizing properties of the turbulent velocity scale w_λ	57
8.5.1.4	Summarizing some useful test cases for the turbulent velocity scale	58
8.5.2	Similarity functions ϕ_λ	59
8.5.2.1	The Large et al. (1994) choices for unstable buoyancy forcing	59
8.5.2.2	Alternative choices for unstable buoyancy forcing	59
8.5.3	The shape function $G_\lambda(\sigma)$ as per Large et al. (1994)	61
8.5.3.1	Constraints arising from the surface boundary condition at $\sigma = 0$	62
8.5.3.2	Constraints arising from matching at $\sigma = 1$	63
8.5.3.3	Vanishing derivative at $\sigma = 1$	63
8.5.4	The non-local term γ_λ as per Large et al. (1994)	64
8.5.4.1	General features of γ_λ with the KPP parameterization	64
8.5.4.2	Summary of the non-local transport parameterization	65
8.5.5	The shape function and non-local transport: Part I	67
8.5.5.1	Problem I: non-local flux larger than surface flux	67
8.5.5.2	Problem II: spuriously large divergence	67
8.5.5.3	Resolution I: two shape functions	68
8.5.5.4	Resolution II: universal shape function	68
8.5.5.5	Further problems to be discussed later	69
8.5.6	Penetrative shortwave and the KPP non-local redistribution	69
8.5.6.1	Physical ideas	69
8.5.6.2	Some mathematics	70
8.5.6.3	Modifying the treatment of shortwave in the KPP non-local flux	70
8.5.7	Bulk Richardson number and the OBL thickness	71
8.5.7.1	Averaging properties over the surface layer	72
8.5.7.2	Non-local gravitational stability	72
8.5.7.3	Unresolved velocity scale U_t used for Ri_b	74
8.5.7.4	An algorithm to specify the unresolved velocity scale U_t	75
8.5.7.5	Minimum value for the unresolved velocity scale U_t	76
8.5.7.6	Restrictions on h under stable buoyancy forcing	76
8.5.7.7	Noise in the boundary layer thickness	77
8.5.8	Surface boundary condition	77
8.5.9	Summary of the standard CVMix implementation of KPP	78
8.6	Further considerations for the KPP non-local term	78
8.6.1	KPP in the top grid cell	79
8.6.2	Tracer evolution with the KPP parameterization	79
8.6.3	A thought experiment with surface cooling	81
8.6.4	Modified shape function for the KPP non-local flux	82
8.6.5	Tests with the modified KPP non-local shape function	84
8.7	KPP with surface waves	84
8.7.1	Modified budgets with Stokes velocity	85
8.7.2	Modifications from Stokes velocity and Langmuir turbulence	86
8.8	Symbols used in this chapter	87

We summarize the KPP surface boundary layer scheme ([Large et al., 1994](#)) as implemented in CVMix. CVMix provides the same features as [Large et al. \(1994\)](#) and Appendix A of [Danabasoglu et al. \(2006\)](#). For those not intent on recovering older results, we make available a simplified treatment of the non-dimensional shape or structure function $G(\sigma)$. The following CVMix Fortran module is directly connected to the material in this chapter:

cvmix_kpp.F90

8.1 Elements of the K-profile parameterization (KPP)

The ocean surface boundary layer (OBL) mediates the exchange of properties between the ocean and other components of the climate system. Hence, parameterization of processes active in the OBL are fundamental to the integrity of a climate simulation. The K-profile parameterization (KPP) is a widely used method for parameterizing boundary layer processes in both the atmosphere and ocean.¹ The paper by [Large et al. \(1994\)](#) introduced this scheme to the ocean community for use in parameterizing processes in the surface ocean boundary layer. The pedagogical lectures by [Large \(1998\)](#) and [Large \(2012\)](#) provide added insight into the scheme that complements some of the material in [Large et al. \(1994\)](#).

The KPP scheme has been used by many ocean climate studies for parameterizing mixing in the OBL, with examples discussed in [Large et al. \(1997\)](#), [Holland et al. \(1998\)](#), [Gent et al. \(1998\)](#), [Umlauf et al. \(2005\)](#), [Li et al. \(2001\)](#), [Smyth et al. \(2002\)](#), [Durski et al. \(2004\)](#), and [Chang et al. \(2005\)](#). It was also used in various climate and earth system models developed at NCAR and GFDL, and elsewhere.

We aim to thoroughly expose physical aspects of the KPP scheme, building on discussions in [Large et al. \(1994\)](#) and [Large \(2012\)](#). We also discuss issues that arose when testing the scheme for CVMix. These tests motivate suggestions for how to make use of the CVMix version of KPP. Correspondingly, we propose simplifications available in CVMix that aim to resolve problems with the [Large et al. \(1994\)](#) implementation.

8.1.1 Conventions

We use the following notational and sign conventions in this chapter.

- The fluid is assumed to be volume conserving Boussinesq. Extensions to a mass conserving non-Boussinesq fluid are trivial.
- The geopotential coordinate, z , increases up, with $z = 0$ defining the resting ocean surface. The ocean free surface is at $z = \eta(x, y, t)$ and the static ocean bottom is at $z = -H(x, y)$. Neither η nor H contain overturns.
- The height coordinate, \mathcal{H} , is defined as minus the depth, d , according to the discussion in Section 2.1, in which

$$\mathcal{H} = -d = z - \eta, \quad (8.1)$$

which lives within the range

$$-(H + \eta) \leq \mathcal{H} \leq 0. \quad (8.2)$$

The CVMix version of the KPP code assumes the calling models (e.g., MOM, MPAS, POP) provide the height as defined here, so that the CVMix code does not need to be given the sea level field.

- A lowercase λ is used to denote a turbulent fluctuation of an arbitrary field within the surface ocean boundary layer; e.g., a tracer such as potential or conservative temperature θ and salinity s , or a velocity component (u, v, w) . Note that x is the notation used in [Large et al. \(1994\)](#) and [Large \(1998\)](#), but we prefer the Greek letter λ to avoid confusion with the horizontal spatial coordinate. Also, the symbol s is sometimes used for scalar fields such as salinity and temperature, whereas m is sometimes used for components of a vector field.

¹We consider here the implementation of KPP for the surface ocean boundary layer, as implementations for the bottom do not exist in MOM or POP. [Durski et al. \(2004\)](#) consider KPP for the ocean bottom in ROMS.

- There is no distinction in the treatment of scalar fields within the KPP boundary layer. It is only beneath the boundary layer, where double diffusive processes are relevant, that we distinguish the mixing between scalar fields such as temperature and salinity. Also, surface forcing for salt/scalars and heat distinguish the tracers.
- An uppercase Λ is used to denote the Eulerian mean of a tracer or velocity component within the surface ocean boundary layer; e.g., potential or conservative temperature Θ , salinity S , or velocity component (U, V, W) . The Eulerian mean fields are time stepped by an ocean climate model within the boundary layer, and correlations of turbulent variables must be parameterized to close the mean field equations.
- The expression $\overline{w\lambda}$ is used to symbolize the Eulerian correlation of the fluctuating turbulent vertical velocity and a fluctuating scalar or vector field. This correlation appears in the mean field time tendency equation for Λ in the Boussinesq primitive ocean equations (see equation (8.8)). KPP provides a parameterization of this vertical turbulent flux within the surface ocean boundary layer.
- The mean and turbulent vertical velocity components, W, w , are positive for upward motion. This sign convention implies that

$$\overline{w\lambda} > 0 \implies \text{turbulent flux for } \lambda \text{ transported vertically upward.} \quad (8.3)$$

If λ is the temperature, then a positive correlation at the ocean surface,

$$\overline{w\theta}^{d=0} > 0, \quad (8.4)$$

corresponds to surface cooling. To reduce notation clutter, correlations evaluated at the ocean surface will be written

$$\overline{w\theta}^0 = \overline{w\theta}^{d=0}. \quad (8.5)$$

- Boundary fluxes of scalar fields are denoted by a capital Q , along with a subscript or superscript to denote the particular flux. Such scalar fluxes are assumed to be positive when entering the ocean and negative when leaving the ocean

$$Q > 0 \implies \text{boundary scalar flux enters the ocean.} \quad (8.6)$$

- We make the following observations about the sign conventions (8.3) and (8.6).
 - A positive heat flux, $Q^{\text{heat}} > 0$, either through the ocean surface or ocean bottom, adds heat to the ocean; likewise for salt and water.
 - The sign convention (8.6) is followed in MOM and POP. However, it is not the convention used in [Large et al. \(1994\)](#), whose convention was in fact opposite for some cases except for penetrative radiation.
 - We consider a positive surface buoyancy forcing, $B_f > 0$ (units $\text{m}^2 \text{s}^{-3}$), to increase the ocean buoyancy. Adding heat to the ocean increases its buoyancy in regions of positive thermal expansion, whereas adding salt decreases buoyancy in regions of positive haline contraction.
 - The convention (8.6) necessitates a minus sign when equating surface boundary fluxes of scalars to the correlations $\overline{w\lambda}^0$ defined by equation (8.3).
 - At the ocean bottom, the convention requires no minus sign, since $\overline{w\lambda}^{d=H+\eta} > 0$ means there is a transfer of scalar field into the ocean through the ocean bottom, such as through geothermal heating. Note that we are not concerned with implementing KPP at the ocean bottom ([Durski et al., 2004](#)).

- Momentum imparted to the ocean surface by a boundary stress, τ , acts to accelerate the ocean in the respective direction. In contrast, a positive sign to a component of $\overline{w\mathbf{u}}^0$ removes the associated momentum from the surface ocean. These sign conventions give rise to the minus sign in the relation (8.30) connecting turbulent kinematic stress to the boundary stress:

$$\overline{w\mathbf{u}}^0 = -\rho^{-1} \tau. \quad (8.7)$$

8.1.2 General form of the KPP parameterization

Ignoring all terms except vertical advective transport in the prognostic equation for the mean field Λ , its time tendency is determined by

$$\frac{\partial \Lambda}{\partial t} = -\left(\frac{\partial(W\Lambda)}{\partial z}\right) - \left(\frac{\partial(\overline{w\lambda})}{\partial z}\right). \quad (8.8)$$

The advective flux by the mean vertical velocity, $W\Lambda$, is represented via a numerical advection operator. In contrast, the turbulent correlation, $\overline{w\lambda}$, is a subgrid scale flux that must be parameterized in order to close the equation for Λ . Here, the overbar signifies an Eulerian averaging operator over unresolved turbulent motions occurring within the OBL.

The KPP scheme provides a first order closure for $\overline{w\lambda}$ within the OBL. It does so by introducing two terms in the following manner

$$\overline{w\lambda} = -K_\lambda \left(\frac{\partial \Lambda}{\partial z}\right) + K_\lambda^{\text{non-local}} \gamma_\lambda. \quad (8.9)$$

The KPP prescription (8.9) thus parameterizes the vertical turbulent flux according to

$$\overline{w\lambda} = \overline{w\lambda}^{\text{local}} + \overline{w\lambda}^{\text{non-local}}. \quad (8.10)$$

The first term provides for the familiar downgradient vertical diffusion determined by a vertical diffusivity and the local vertical derivative of the mean field. This term is referred to as the local portion of the parameterization

$$\overline{w\lambda}^{\text{local}} = -K_\lambda \left(\frac{\partial \Lambda}{\partial z}\right). \quad (8.11)$$

Note that the diffusivity K_λ computed from KPP is a non-local function of boundary layer properties, so the name “local” is not directed at the diffusivity, but instead at the vertical derivative. The second term, γ_λ , accounts for non-local transport that is not directly associated with local vertical gradients of Λ , in which

$$\overline{w\lambda}^{\text{non-local}} = K_\lambda^{\text{non-local}} \gamma_\lambda. \quad (8.12)$$

8.1.3 The vertical diffusivity

The KPP vertical diffusivity used to parameterize the local flux (8.11) in the OBL is determined as a non-local function of boundary layer properties. It is written in the following form

$$K_\lambda(\sigma) = h w_\lambda(\sigma) G_\lambda(\sigma). \quad (8.13)$$

The diffusivity is constructed as the product of three terms:

- boundary layer thickness h ,
- vertical turbulent velocity scale $w_\lambda(\sigma)$,
- dimensionless vertical shape or structure function $G_\lambda(\sigma)$.

Note that we introduce a dependence of the shape function on the field diffused. Such dependence can arise if taking the approach of Large et al. (1994) whereby the boundary layer diffusivity is matched at the base of the boundary layer to the interior diffusivities, which can generally be a function of the tracer,

λ . However, as discussed in Section 8.5.5, the recommended approach for CVMix is to use the following universal shape function for all tracers (equation (8.157))

$$G(\sigma)_{\text{universal}} = \sigma (1 - \sigma)^2, \quad (8.14)$$

thus greatly simplifying the KPP scheme.

Large et al. (1994) proposed to set the diffusivities equal

$$K_{\lambda}^{\text{non-local}} = K_{\lambda}, \quad (8.15)$$

and we support that recommendation, along with setting the shape function to the universal form (8.14). However, in moving from the Large et al. (1994) version of KPP to this simplified version, one may choose to test an intermediate version in which the non-dimensional shape function is distinct for $K_{\lambda}^{\text{non-local}}$ and K_{λ} . It is for this reason that we maintain the distinct symbols for the diffusivities, even though we recommend users choose the CVMix implementation of KPP that sets them equal. We have more to say on this topic in Section 8.5.3.

8.1.3.1 Boundary layer thickness

The boundary layer thickness is denoted by

$$h \geq 0 \text{ is the boundary layer thickness.} \quad (8.16)$$

This is the thickness of the OBL prescribed by the KPP scheme, with details given in Section 8.5.7. The surface boundary layer generally thickens when mechanical forcing mixes the water, and negative buoyancy forcing makes the water gravitationally unstable. Conversely, the boundary layer shoals with weak winds and/or positive buoyancy forcing. The direct dependence of the vertical diffusivity in equation (8.13) on the OBL thickness manifests the common property of boundary layers, whereby thicker layers generally arise from stronger eddy motions and are thus associated with more rapid mixing of tracer concentration and momentum.

Figure 8.1 provides a schematic of the KPP boundary layer, the Monin-Obukhov surface layer, and the associated momentum, mass, and buoyancy fluxes impacting these layers. Details of this figure will be explored in the following.

8.1.3.2 Measuring vertical distances within the OBL

When measuring distances within the boundary layer, it is the thickness of the water as measured from the ocean surface that is important. Free surface undulations can be a nontrivial fraction of the boundary layer thickness, particularly under conditions of stable buoyancy forcing. Hence, we make explicit note that the ocean has an undulating free surface at $z = \eta(x, y, t)$, which contrasts to Large et al. (1994) and Large (1998), who assumed that $z = 0$ sets the upper ocean surface.

Following Large et al. (1994), we introduce the non-dimensional depth, σ , given by

$$\sigma = \frac{d}{h}. \quad (8.17)$$

In this definition, $d \geq 0$ is the distance from the ocean surface at $z = \eta$ to a point within the boundary layer

$$d = -z + \eta. \quad (8.18)$$

Likewise, $h \geq 0$ is the distance from the free surface to the bottom of the boundary layer

$$h = h_{\text{obl}} + \eta, \quad (8.19)$$

where h_{obl} is the depth of the boundary layer as measured from $z = 0$. That is, h is the thickness of the OBL, and it is this thickness, not h_{obl} , that is predicted by KPP (Section 8.5.7). Regions within the boundary layer are given by the non-dimensional depth range

$$0 \leq \sigma \leq 1 \quad \text{within boundary layer,} \quad (8.20)$$

with $\sigma = 0$ the ocean surface and $\sigma = 1$ the bottom of the boundary layer.

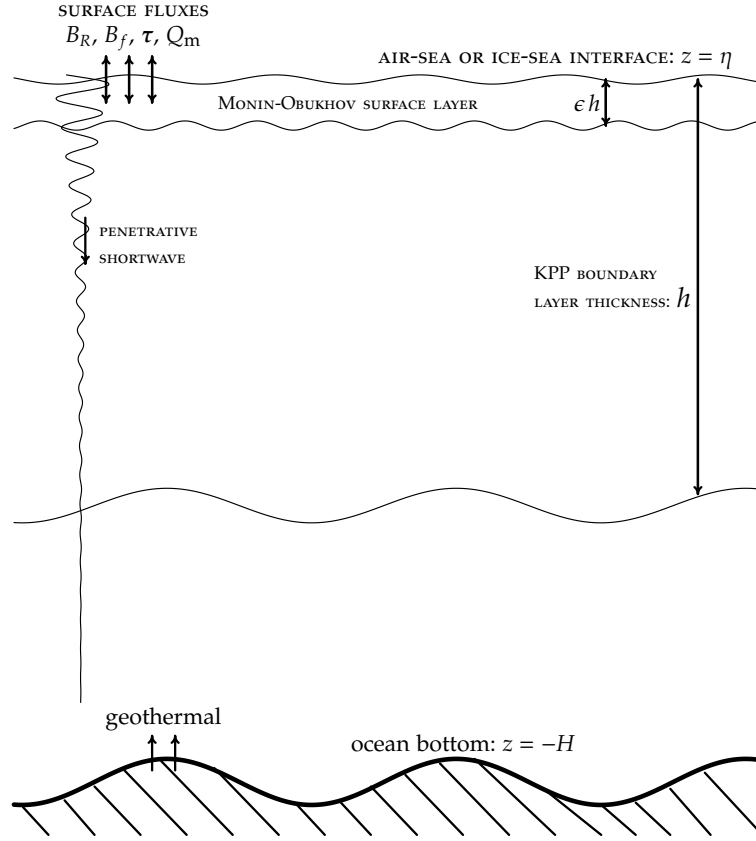


Figure 8.1: Schematic of the upper ocean boundary layer regions associated with the KPP boundary layer parameterization. The upper ocean is exposed to non-penetrative air-sea and ice-sea fluxes of momentum τ (Section 8.2), mass Q_m (Section 8.3), and buoyancy B_f (Section 8.3). In addition, there is penetrative shortwave radiation, $-w\theta_R$ (Section 8.3), indicated by the exponentially decaying vertical sinusoidal. The Monin-Obukhov surface layer (Section 8.4) has a thickness ϵh , with $\epsilon \approx 0.1$. The surface layer is where turbulence delivers fluxes to the molecular skin layer for transfer to the atmosphere or ice. The surface layer starts from just beneath the surface roughness elements at the upper ocean interface. Since neither these roughness elements, nor the molecular viscous sublayer, are resolved in ocean models, we assume in practice that the Monin-Obukhov surface layer extends to the sea surface at $z = \eta(x, y, t)$. The KPP boundary layer includes the surface layer, and it has a thickness $h(x, y, t)$ determined by the KPP parameterization (Section 8.5.7). The ocean bottom at $z = -H(x, y)$ is rigid and is exposed to geothermal heating. Presently, the KPP boundary layer scheme has not been implemented in MOM or POP to parameterize bottom boundary layer physics, though nothing fundamental precludes such. In fact, [Durski et al. \(2004\)](#) provide just such an implementation.

8.1.3.3 Scale for turbulent vertical velocity fluctuations w_λ

We introduce a scale for turbulent vertical velocity fluctuations, written as $w_\lambda(\sigma)$. This scale is a function of depth within the boundary layer, and a function of the field to which it refers. [Large et al. \(1994\)](#) recommend using the same scale w_s for all scalar fields (temperature, salinity, and passive tracers)

$$w_s = \text{same for all scalars.} \quad (8.21)$$

The scale w_s also is the same as the turbulent velocity scale for momentum, w_m , in cases where the surface buoyancy forcing, B_f is positive. However, $w_m < w_s$ under unstable surface buoyancy forcing

$$w_m = w_s \quad B_f > 0 \quad (8.22a)$$

$$w_m < w_s \quad B_f < 0. \quad (8.22b)$$

That is, gravitational instability is assumed to mix scalars more efficiently than momentum. We return to the specification of w_λ in Section 8.5.1.

8.1.3.4 Non-dimensional vertical shape function $G_\lambda(\sigma)$

Non-dimensional vertical shape function $G_\lambda(\sigma)$ is used to smoothly transition from the ocean surface to the bottom of the boundary layer. Large et al. (1994) chose a cubic polynomial

$$G_\lambda(\sigma) = a_0 + a_1 \sigma + a_2 \sigma^2 + a_3 \sigma^3. \quad (8.23)$$

Since turbulent eddies do not cross the ocean surface at $\sigma = 0$, we should correspondingly have a vanishing diffusivity at $\sigma = 0$. This constraint is satisfied by setting

$$a_0 = 0. \quad (8.24)$$

We detail in Section 8.5.3 how to specify the remaining expansion coefficients a_1, a_2, a_3 following the approach from Large et al. (1994), in which the polynomial coefficients a_1, a_2, a_3 depend on the tracer fields in so far as they are specified by matching to the interior diffusivities. Double diffusive processes lead to distinct diffusivities for temperature and material tracers such as salt.

However, as discussed in Section 8.5.3, the recommended approach for CVMix is to use the following universal shape function for all tracers (equation (8.157))

$$G(\sigma)_{\text{universal}} = \sigma (1 - \sigma)^2, \quad (8.25)$$

thus greatly simplifying the KPP scheme. This universal shape function satisfies

$$G(0)_{\text{universal}} = G(1)_{\text{universal}} = G'(1)_{\text{universal}} = 0, \quad (8.26)$$

which is the form suggested by atmospheric boundary layer implementations of KPP (see Figure 8.3).

8.1.4 The non-local transport γ_λ

There are many processes in the boundary layer that lead to transport that is difficult to parameterize as a function of the local vertical derivative of the mean field (see Section 2 of Large et al. (1994)). This behaviour leads to a diffusivity K_λ that is a function of the surface fluxes and boundary layer thickness h . Furthermore, under convective forcing (negative surface buoyancy forcing; $B_f < 0$), fluxes can penetrate into the stratified interior. This characteristic then motivates the introduction of a non-local transport term γ_λ to the KPP parameterization (equation (8.9)) in the case of $B_f < 0$. To further identify the need for a non-local transport term γ_λ , we reproduce Figure 1 from Large et al. (1994), here shown as Figure 8.2. The caption to Figure 8.2 explores the many facets of this figure used to help justify the non-local term in KPP.

As part of the KPP parameterization, the non-local transport, γ_λ , aims to account for such processes as boundary layer eddies whose transport may be unrelated to the local vertical gradient of the mean field, and whose impacts may penetrate within the stratified ocean interior. In general, Large et al. (1994) prescribe the following characteristics to γ_λ .

- Page 371 of (Large et al., 1994) notes that there is no theory for non-local momentum transport, so the non-local transport is assumed to directly affect only the tracer fields:

$$\gamma_\lambda = \begin{cases} 0 & \text{if } \lambda = (u, v, w) \text{ a velocity component} \\ \neq 0 & \text{nonzero if } \lambda = \theta, s \text{ or another tracer.} \end{cases} \quad (8.27)$$

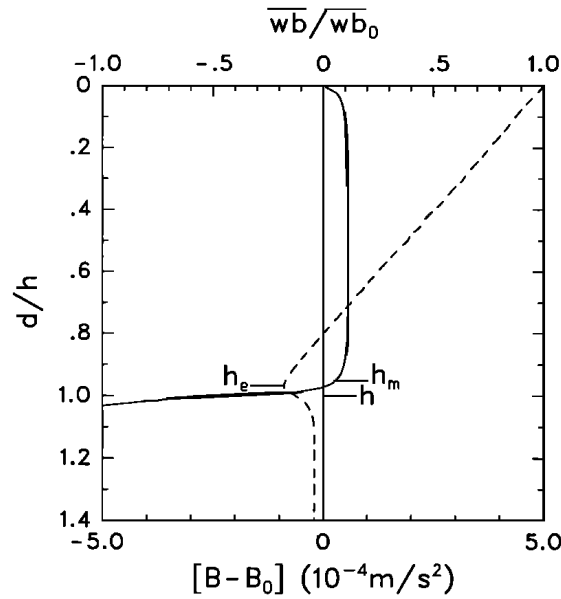


Figure 8.2: This is a reproduction of Figure 1 from [Large et al. \(1994\)](#). The figure is derived from a one-dimensional simulation after 3 days of convective deepening (zero winds; negative surface buoyancy forcing) into an initially uniformly stratified water column. The vertical axis is vertical distance starting from the ocean surface interface at $z = \eta$ and $d = 0$, extending down to $d = h$ ($h = 13.6$ m at this point of the integration), which is the base of the boundary layer, and finally to $d = 1.4h$, which is beneath the boundary layer.

The horizontal axis on the bottom is the mean buoyancy, B , relative to that at the surface, B_0 , and the profile is depicted by the solid line. Positive values of $B - B_0$ indicate that the mean buoyancy at a point is larger than at the surface, with $B - B_0 > 0$ expected under negative buoyancy forcing at the ocean surface.

The horizontal axis on the top is the ratio of the local turbulent buoyancy flux \overline{wb} to the surface turbulent flux \overline{wb}^0 (denoted \overline{wb}_0 by [Large et al. \(1994\)](#)). The dashed line depicts this ratio. Positive values of \overline{wb} represent upward turbulent buoyancy fluxes; e.g., upward fluxes of heat (ocean surface cooling) for the case where buoyancy is determined by temperature, and the thermal expansion coefficient is positive.

Positive values for \overline{wb} in regions between roughly $0.35 < d < 0.8$ represent upward turbulent buoyancy fluxes in a region where the mean vertical gradient of B is nearly zero, thus indicating non-local turbulent transport. In shallower regions with $d < 0.35$, the mean gradient is negative, $\partial_z B < 0$, and the fluxes are positive, $\overline{wb} > 0$, thus representing downgradient turbulent fluxes. Likewise, for $d > 0.8$, the turbulent fluxes are downgradient.

The mixed layer depth is denoted by h_m , though this depth is subject to arbitrary specification of the density difference. The entrainment depth is h_e , with this depth taken where the buoyancy flux reaches a negative extrema. Note that it is an empirical result that under pure convective forcing ($\tau = 0, B_f < 0$), the turbulent entrainment flux is roughly 20% of the surface flux: $\overline{wb}^{d=h_e} = \beta_T \overline{wb}^0$, where $\beta_T = -0.2$. This situation is depicted in the figure.

[Smyth et al. \(2002\)](#) consider a non-local term for momentum, thus motivating further research to see whether it is suitable for climate modeling. CVMix has not implemented the [Smyth et al. \(2002\)](#) scheme. However, CVMix has hooks available in the code for a non-local momentum transport term, thus facilitating further research into this question.

- The non-local transport is non-zero only within the OBL:

$$\gamma_\lambda = \begin{cases} 0 & \text{if } \sigma > 1 \\ \neq 0 & \text{if } 0 \leq \sigma \leq 1. \end{cases} \quad (8.28)$$

- The non-local transport is non-zero only in the presence of destabilizing negative surface ocean buoyancy flux, whose presence gives rise to convective mixing:

$$\gamma_\lambda = \begin{cases} 0 & \text{for positive (stabilizing) surface buoyancy forcing} \\ \neq 0 & \text{for negative (destabilizing) surface buoyancy forcing.} \end{cases} \quad (8.29)$$

- The non-local transport can give rise, under certain conditions, to either down-gradient or up-gradient transport of the mean tracer field. Hence, it can either act to smooth gradients of mean fields (down-gradient non-local fluxes) or enhance gradients (upgradient non-local fluxes).

We summarize the KPP parameterization of γ_λ in Section 8.5.4. As shown in that section, the KPP non-local transport acts to redistribute the surface tracer fluxes throughout the boundary layer.

8.1.5 Some caveats regarding KPP

Subsequent to [Large et al. \(1994\)](#), many ocean modelling groups have made use of the KPP scheme for ocean climate purposes. One key practical feature of the scheme is the general ability to use relatively coarse vertical grid spacing, more coarse than typically suitable for turbulent kinetic energy methods such as those coded in [Umlauf et al. \(2005\)](#). Physically, the non-local transport term available in KPP can capture features in the boundary layer that are more difficult, if not impossible, to parameterize using local methods.

Nonetheless, KPP is not a complete scheme nor is it without its problems. For example, as we note in Section 8.6, there are cases where KPP is clearly performing in an unphysical manner. One key reason the scheme can be pushed outside of physical relevance concerns the absence of an energetic basis for KPP. Furthermore, the non-local scheme is not constrained to satisfy the 2nd Law of Thermodynamics, meaning that it can produce extrema. We present potential “fixes” in Section 8.6. However, these fixes are based largely on *ad hoc* considerations. A more fundamental approach may be to combine the ideas of KPP with those of energetically based turbulence closure schemes. Such considerations are the topic of ongoing research.

8.2 Surface ocean boundary momentum fluxes

In this section and Section 8.3, we present features of how surface boundary fluxes force the upper ocean, largely following Appendix A of [Large et al. \(1994\)](#). The aim is to identify how surface boundary fluxes impact the upper ocean, with this characterization then used in Section 8.4 to help establish some basic features of ocean boundary layers. These ideas are then used in Section 8.5 to specify the diffusivity and non-local transport from the KPP parameterization.

Vertical exchange of momentum across the atmosphere-ocean or sea-ice-ocean boundary occurs largely through turbulent processes. The resulting horizontal stress vector acting on the ocean, τ , is determined through application of a bulk formula (e.g., see Appendix C of [Griffies et al. \(2009\)](#) or [Large and Yeager \(2009\)](#)). For our purposes, we assume τ is given, thus yielding the ocean kinematic fluxes associated with the turbulent transport of momentum across the ocean surface at $d = -z + \eta = 0$

$$-\overline{w\mathbf{u}}^0 = \left(\frac{\tau}{\rho(\eta)} \right) \approx \left(\frac{\tau}{\rho_o} \right). \quad (8.30)$$

In this equation, $\rho(\eta)$ is the surface ocean density, which is commonly approximated by the constant Boussinesq reference density ρ_o . A positive sign on a component of τ acts to accelerate the flow in the

respective direction, whereas a positive sign to a component of $\overline{w\mathbf{u}}^0$ removes momentum from the ocean. These sign conventions give rise to the minus sign in the relation (8.30). In addition to defining the kinematic surface fluxes, knowledge of τ allows us to compute surface boundary layer velocity scales when working within the Monin-Obukhov similarity theory (Section 8.4.2).

In addition to turbulent momentum transfer, τ is associated with momentum transported through mass exchange across the ocean surface, since water transported across the ocean generally carries a nonzero momentum. [Kantha and Clayson \(2000\)](#) (see their page 431) point out that this effect can be nontrivial, particularly when resolving strong atmospheric storms. They also make the case for including this effect in computing the Monin-Obukhov length scale defined by equation (8.79) (see their equation (4.3.11)). Notably, when running a coupled model, the stress from rain is included, since it is part of the momentum convergence acting at the bottom of the atmospheric column. Modifying the stress from a prescribed atmospheric state, such as CORE ([Large and Yeager, 2009](#)), requires further considerations.

8.3 Surface ocean boundary buoyancy fluxes

Turbulent and advective fluxes of momentum and buoyancy are transferred across the upper ocean surface boundary, with ocean processes such as advection and mixing then transporting the boundary momentum and buoyancy laterally as well as into the ocean interior. In contrast, penetrative shortwave radiation is absorbed into the ocean absent ocean transport processes, with such absorption a function of ocean optical properties. In the unphysical case of perfectly transparent seawater, shortwave radiation penetrates through the boundary layer and so has no influence on boundary layer processes. In realistic cases, much of the shortwave radiation is absorbed in the boundary layer, with only a fraction leaking through to the interior. In general, such non-turbulent and non-advective transport of buoyancy via penetrative radiation represents a fundamentally novel aspect of ocean boundary layer physics relative to the atmosphere. Namely, for the atmosphere, radiative absorption is far less relevant than in the upper ocean, since the atmosphere is largely transparent to radiation. We therefore consider penetrative shortwave radiation as distinct from other buoyancy fluxes when formulating how boundary fluxes impact the ocean.

8.3.1 General features of buoyancy forcing

The buoyancy of a fluid is commonly defined as (e.g., page 83 of [Large \(1998\)](#))

$$B = g \left(\frac{\rho_o - \rho}{\rho_o} \right), \quad (8.31)$$

where g is the constant gravitational acceleration, and ρ_o is a reference density, taken here to equal the Boussinesq reference density. A reduction in density is associated with an increase in buoyancy; that is, the water becomes more *buoyant*. Changes in buoyancy arise through changes in density associated with temperature and salinity changes, since buoyancy changes are computed relative to a fixed pressure level. In this way, buoyancy changes are directly related to processes that impact locally referenced potential density.

Ocean buoyancy is affected through surface ocean heat, salt, and water fluxes. These fluxes are associated with the following physical processes.

- Turbulent processes transfer heat through latent and sensible heating.
- Longwave radiation cools the upper ocean, with this radiation affected by the upper ocean skin temperature.
- Penetrative shortwave radiation is absorbed in seawater and so increases buoyancy.
- The transfer of salt occurs when sea ice melts and forms. This transfer is proportional to the water mass flux and the difference in salinity between the liquid ocean and sea ice. More generally, we simply consider this process to be associated with a salt flux between sea ice and ocean, with this flux operationally computed as part of a sea ice model.

- Advective processes transfer heat and salt across the ocean surface through the transfer of water mass across the interface.

We further detail these processes in the following.

8.3.2 Scalar budgets for a surface ocean model grid cell

Buoyancy is not a prognostic variable in ocean models. So to develop a quantitative understanding of how buoyancy is impacted by surface fluxes, we consider the evolution of temperature, salinity, and mass in an arbitrary top model grid cell, and focus exclusively on evolution arising from surface boundary fluxes. We write these budgets in their finite volume sense, which includes density and thickness weighting of scalar tracer fields

$$\frac{\partial(\rho dz \Theta)}{\partial t} = Q_m \Theta_m + Q_{\theta}^{\text{non-pen}} + (Q_{\theta}^{\text{pen}}(z = \eta) - Q_{\theta}^{\text{pen}}(z = -\Delta z)) \quad (8.32)$$

$$\frac{\partial(\rho dz S)}{\partial t} = Q_m S_m + Q_S \quad (8.33)$$

$$\frac{\partial(\rho dz)}{\partial t} = Q_m. \quad (8.34)$$

We now detail the terms appearing in these equations.

- ρdz is the mass per horizontal area of seawater in the grid cell. For a volume conserving Boussinesq fluid, the *in situ* density, ρ , is set to the constant reference density ρ_o

$$\rho = \rho_o \quad \text{Boussinesq fluid.} \quad (8.35)$$

- Θ is the grid cell potential temperature, or more accurately it is the conservative temperature of McDougall (2003) (see IOC et al. (2010)).
- S is the grid cell salinity.
- Q_m is the mass flux ($\text{kg m}^{-2} \text{sec}^{-1}$) of water crossing the ocean surface. Following the sign convention (8.6), we consider $Q_m > 0$ for water entering the ocean (as when precipitation plus runoff exceeds evaporation).
- Θ_m is the temperature of water crossing the ocean surface, and $C_p^o Q_m \Theta_m$ is the associated enthalpy flux (W m^{-2}). We further discuss this flux in Section 8.3.4.
- S_m is the salinity of water crossing the ocean surface, and $Q_m S_m$ is the associated mass flux of salt. Note that S_m is typically taken to be zero, as for precipitation and evaporation. However, rivers can contain a nonzero salt concentration, so we keep S_m for the following formulation. We further discuss this salt flux in Section 8.3.4.
- C_p^o is the seawater heat capacity at constant pressure ($\text{J kg}^{-1} \text{ } ^\circ\text{C}^{-1}$). IOC et al. (2010) provides the most precise value appropriate for an ocean with heat measured through conservative temperature.
- Q_S is the flux of salt ($\text{kg m}^{-2} \text{sec}^{-1}$) that crosses the ocean surface. Following the sign convention (8.6), we take $Q_S > 0$ when salt enters the ocean. This flux arises in the transfer of salt when sea ice forms and melts. We further discuss this salt flux in Section 8.3.3.
- $C_p^o Q_{\theta}^{\text{non-pen}}$ is the non-penetrative surface heat flux associated with turbulent processes (latent and sensible) and radiative longwave cooling (W m^{-2}). Following the sign convention (8.6), we take $Q_{\theta}^{\text{non-pen}} > 0$ for heat entering the ocean surface (i.e., ocean warming). We further discuss this heat flux in Section 8.3.5.
- $C_p^o Q_{\theta}^{\text{pen}}(z = \eta)$ is the radiative shortwave heat flux (W m^{-2}) entering the ocean through its surface at $z = \eta$, with $Q_{\theta}^{\text{pen}}(\eta) > 0$ warming the ocean surface. Likewise, $C_p^o Q_{\theta}^{\text{pen}}(z = -\Delta z)$ is the radiative shortwave heat flux leaving the top cell through its bottom face. We further discuss this heat flux in Section 8.3.7.

8.3.3 Salt fluxes from sea ice melt and formation

The mass flux of salt Q_s ($\text{kg m}^{-2} \text{sec}^{-1}$) is positive for salt entering the ocean. There is transport of salt across the ocean surface when sea ice forms and melts, due to the nonzero salt content in sea ice. Otherwise, the surface salt flux is generally zero for the large scale ocean. For ocean models, however, the salt flux can be nonzero when formulating the surface boundary in terms of virtual salt fluxes rather than real water fluxes (Huang, 1993; Griffies et al., 2001). It can also be non-zero when using an ocean-ice model that is not coupled to an atmosphere or land model, in which case salt restoring is required to maintain stability of the overturning circulation (see Section 3 of Griffies et al. (2009)).

8.3.4 Salt and heat fluxes associated with water transport

In most cases, salinity in the water fluxed across the ocean surface is zero, so that $S_m = 0$. However, there are some cases where rivers have a nonzero salinity so that $S_m \neq 0$ and the product $Q_m S_m$ leads to an advective transport of salt across the ocean surface.

Since water transported across the ocean has a nonzero heat content, this transport in turn affects the net heat content in the upper ocean. One can either prescribe the temperature of this water, Θ_m , or the product $Q_m \Theta_m$. Consider the case where the product is specified for river water entering the ocean, which is the case with the GFDL land model used in the earth system model of Dunne et al. (2012). In this case, the heat flux with respect to 0°C (in units of W m^{-2}) of liquid river runoff $\mathcal{H}^{\text{liquid runoff}}$ is given to the ocean from the land model, so that

$$Q_m \Theta_m = \frac{\mathcal{H}^{\text{liquid runoff}}}{C_p^{\text{liquid runoff}}}, \quad (8.36)$$

with $C_p^{\text{liquid runoff}}$ the heat capacity of the water coming in from the river runoff. Likewise, if the heat associated with frozen runoff (e.g., calving land ice) is provided by the land model, then we have

$$Q_m \Theta_m = \frac{\mathcal{H}^{\text{solid runoff}}}{C_p^{\text{solid runoff}}}, \quad (8.37)$$

with $C_p^{\text{solid runoff}}$ the heat capacity of the solid runoff. These two heat capacities are typically provided by the component model (i.e., the land model) used to compute the runoff fields. Similar considerations hold for transfer of water between sea ice models and the ocean.

8.3.5 Non-penetrative surface heat fluxes

Following the sign convention (8.6), the heat flux $C_p^o Q_\theta^{\text{non-pen}}$ (W m^{-2}) is positive for heat entering the ocean. This flux is comprised of the following contributions (see page 34 of Gill, 1982)

$$C_p^o Q_\theta^{\text{non-pen}} = Q_{\text{long}} + Q_{\text{latent}} + Q_{\text{sens}}. \quad (8.38)$$

Longwave, latent, and sensible heat fluxes are typically deposited or withdrawn from the ocean surface layer (Section 8.4). In practice, ocean models assume these fluxes are taken entirely from the surface grid cell.

These fluxes are termed non-penetrative since they are deposited or withdrawn from the liquid ocean surface layer, with transport then occurring through ocean advection and mixing. This behaviour contrasts to that of penetrative shortwave radiation, which is transferred into the ocean interior as a function of seawater optics, so it does not depend on ocean transport. We now comment in a bit more detail on the various non-penetrative fluxes.

8.3.5.1 Longwave radiation

Longwave radiation leaves the ocean in the form of the $\sigma_{\text{SB}} T^4$ Stefan-Boltzmann Law, with T the skin temperature and

$$\sigma_{\text{SB}} = 5.6734 \times 10^{-8} \text{ W m}^{-2} \text{ }^\circ\text{K}^{-4} \quad (8.39)$$

the Stefan-Boltzmann constant. Following the sign convention detailed in Section 8.1.1, $Q_{\text{long}} < 0$ since the longwave heat flux removes heat from the ocean surface and sends it back to the atmosphere.

8.3.5.2 Latent heat fluxes

Q_{latent} arises from phase changes whereby liquid seawater either evaporates, or it acts to melt frozen precipitation. In either case, $Q_{\text{latent}} < 0$ since the liquid ocean loses heat to energize the phase changes.

When seawater evaporates, the latent heat lost by the ocean is determined by the latent heat of vaporization for fresh water

$$H^{\text{vapor}} = 2.5 \times 10^6 \text{ J kg}^{-1}, \quad (8.40)$$

so that

$$Q_{\text{evap}} = H^{\text{vapor}} Q_{\text{m}}^{\text{evap}} \quad (8.41)$$

where $Q_{\text{m}}^{\text{evap}} < 0$ is the mass flux ($\text{kg m}^{-2} \text{ sec}^{-1}$) of fresh water leaving the ocean due to evaporation. A similar expression holds when seawater melts frozen precipitation (e.g., snow), in which case

$$H^{\text{fusion}} = 3.34 \times 10^5 \text{ J kg}^{-1}, \quad (8.42)$$

so that

$$Q_{\text{melt}} = -H^{\text{fusion}} Q_{\text{m}}^{\text{frozen precip}}, \quad (8.43)$$

where $Q_{\text{m}}^{\text{frozen precip}} > 0$ is the mass flux ($\text{kg m}^{-2} \text{ sec}^{-1}$) of frozen precipitation falling onto the ocean surface. Again, both Q_{evap} and Q_{melt} are negative since latent heating extracts heat from the ocean.

8.3.5.3 Sensible heat fluxes

Q_{sens} is the sensible heat transfer proportional to the difference between the ocean temperature and that of the atmosphere, sea ice, or land ice. Sensible heating generally acts to cool the ocean ($Q_{\text{sens}} < 0$), particularly near western boundary currents such as the Gulf Stream, Kuroshio, and Agulhas.

8.3.6 The case of frazil

As the temperature of seawater cools to the freezing point, sea ice is formed, initially through the production of frazil ice. Frazil can generally form at various levels in the upper ocean, though many ocean models assume frazil production occurs just in the top grid cell. Operationally in an ocean model, liquid water can be supercooled at any particular time step through surface fluxes and transport. An adjustment process is used to heat the liquid water back to the freezing point, with this positive heat flux $Q_{\text{frazil}} > 0$ extracted from the ice model as frazil sea ice is formed. When that adjustment is performed may determine whether to include Q_{frazil} as part of the net heat flux impacting the boundary layer turbulence. We omitted frazil heating in equation (8.38), as that is the approach taken at NCAR. However, others, such as GFDL prior to 2012, include frazil as part of the KPP boundary layer calculation. We summarize the issues here.

- **FRAZIL OMITTED FROM B_f :** When computing the surface buoyancy flux, B_f , for use in KPP, the NCAR practice omits frazil heating, as reflected in equation (8.38). In effect, this approach assumes that all the negative buoyancy forcing that occurs in the upper ocean is used to drive convective boundary layer turbulence. After mixing, a portion of the heat, $Q_{\text{frazil}} > 0$, is returned to the liquid ocean to warm the water back to freezing, with this heat taken from the ice model as it forms frazil sea ice.
- **FRAZIL INCLUDED IN B_f :** Many ocean climate models compute frazil heating just in the top model grid cell. It is thus operationally trivial to include $Q_{\text{frazil}} > 0$ as another term in the non-penetrative heating (equation (8.38)). Physically, this approach adds the amount of heat Q_{frazil} to the buoyancy flux, and so potentially reduces the strength of the otherwise convective turbulence in the upper ocean. This approach has been used at GFDL prior to 2012. However, with the incorporation of CVMix into MOM6, GFDL practice has moved towards that of NCAR whereby frazil is *not* included in B_f .

We have no strong argument for one approach versus the other. Tests should be run to consider sensitivity to the choice.

8.3.7 Penetrative shortwave radiation

The penetrative shortwave radiative heat flux $C_p^o Q_\theta^{\text{pen}} > 0$ arises from the net shortwave radiation entering through the ocean surface and absorbed by seawater. This heat flux does *not* arise from turbulent or advective processes, which makes it distinct from other heat and salt fluxes impacting the ocean through its upper boundary. This radiation is not generally deposited entirely within the ocean surface layer or the top ocean model grid cell. Instead, a fraction of this radiation can penetrate to beneath the surface ocean grid cell, with the fraction depending on the optical properties of seawater and thickness of the grid cell. Hence, we subtract a heat flux $C_p^o Q_\theta^{\text{pen}}(z = -\Delta z)$, which represents the radiative shortwave heat flux passing through the bottom of the surface ocean cell at $z = -\Delta z$. It is the difference,

$$\text{net shortwave heating of surface grid cell} = C_p^o \left(Q_\theta^{\text{pen}}(z = \eta) - Q_\theta^{\text{pen}}(z = -\Delta z) \right) \quad (8.44)$$

that stays in the surface grid cell. When considering the same budget for the surface ocean boundary layer, we are interested in the shortwave flux that penetrates through the bottom of the boundary layer at $z = -h$.

8.3.8 Buoyancy budget for a surface ocean model grid cell

We now bring the previous fluxes together to form the budget for buoyancy in a surface grid cell due to the impacts of surface fluxes. The resulting expression is then used to derive an expression for the buoyancy forcing that acts on the ocean surface boundary layer. Buoyancy (equation (8.31)) has a time tendency given by

$$-\left(\frac{\rho_o}{g}\right) \frac{\partial B}{\partial t} = \rho_{,\Theta} \frac{\partial \Theta}{\partial t} + \rho_{,S} \frac{\partial S}{\partial t}, \quad (8.45)$$

where we introduced the shorthand notation

$$\rho_{,\Theta} = \left(\frac{\partial \rho}{\partial \Theta} \right)_{S,p} \quad (8.46)$$

$$\rho_{,S} = \left(\frac{\partial \rho}{\partial S} \right)_{\Theta,p} \quad (8.47)$$

for the partial derivatives of density with respect to conservative temperature and salinity, respectively, each with pressure held constant. We wish to form an evolution equation for buoyancy at the ocean surface grid cell just due to the effects of surface forcing. For this purpose, multiply the temperature equation (8.32) by $\rho_{,\Theta}$ and add to the surface salinity equation (8.33) multiplied by $\rho_{,S}$

$$\rho_{,\Theta} \left(\frac{\partial(\rho dz \Theta)}{\partial t} \right) + \rho_{,S} \left(\frac{\partial(\rho dz S)}{\partial t} \right) = Q_m (\rho_{,\Theta} \Theta_m + \rho_{,S} S_m) + \rho_{,\Theta} (Q_\theta^{\text{non-pen}} + \delta_k Q_\theta^{\text{pen}}) + \rho_{,S} Q_s, \quad (8.48)$$

where we introduced the shorthand

$$\delta_k Q_\theta^{\text{pen}} = Q_\theta^{\text{pen}}(z = \eta) - Q_\theta^{\text{pen}}(z = -\Delta z). \quad (8.49)$$

We now use the mass budget (8.34) and introduce the buoyancy tendency according to equation (8.45) to realize an expression for the time tendency of the surface ocean buoyancy

$$(\rho_o/g) \rho dz \left(\frac{\partial B}{\partial t} \right) = Q_m [\rho_{,\Theta} (\Theta - \Theta_m) + \rho_{,S} (S - S_m)] + \rho_{,\Theta} (Q_\theta^{\text{non-pen}} + \delta_k Q_\theta^{\text{pen}}) - \rho_{,S} Q_s. \quad (8.50)$$

Now introduce the thermal expansion and saline contraction coefficients

$$\alpha = -\frac{1}{\rho} \left(\frac{\partial \rho}{\partial \Theta} \right)_{S,p} \quad (8.51)$$

$$\beta = \frac{1}{\rho} \left(\frac{\partial \rho}{\partial S} \right)_{\Theta,p} \quad (8.52)$$

to render

$$\frac{dz}{dt} \left(\frac{\partial B}{\partial t} \right) = \frac{g}{\rho_o} \left(Q_m [-\alpha (\Theta - \Theta_m) + \beta (S - S_m)] + \alpha (\delta_k Q_\theta^{\text{pen}} + Q_\theta^{\text{non-pen}}) - \beta Q_S \right). \quad (8.53)$$

8.3.9 Surface boundary terms contributing to buoyancy evolution

We now summarize the various boundary terms appearing on the right hand side of the surface grid cell buoyancy budget (8.53).

8.3.9.1 Heat carried by water transport

Assuming a positive thermal expansion coefficient, $\alpha > 0$, the term $-Q_m \alpha (\Theta - \Theta_m)$ reduces ocean buoyancy when adding water $Q_m > 0$ to the ocean that is colder than the surface ocean temperature, $\Theta = \Theta_{k=1}$. The opposite occurs in regions of cold fresh waters, such as the Baltic, where $\alpha < 0$. In such cases, adding water to the ocean that is colder than the sea surface temperature increases seawater buoyancy. Given the ability for α to change sign in the World Ocean, it is important to avoid making any assumptions about heating always increasing buoyancy. We now consider in turn the three cases evaporation, precipitation, and liquid river runoff and indicate how they are typically treated in climate models.

- In large-scale modeling, we generally assume that evaporating water leaves the ocean at the sea surface temperature, so that

$$\Theta^{\text{evap}} = \Theta_{k=1} \quad \text{climate models}, \quad (8.54)$$

in which case there is no change to ocean temperature upon transfer of evaporating water across the ocean surface.

- Precipitating liquid water need not fall on the ocean at the sea surface temperature, so that

$$\Theta^{\text{precip}} \neq \Theta_{k=1} \quad \text{real world}. \quad (8.55)$$

Kantha and Clayson (2000) (see their page 429) discuss this difference, and the associated transfer of heat across the ocean due to rain events, particularly in the West Pacific. However, we know of no climate modeling application in which the atmospheric model component carries information about the temperature of its condensed water, nor the heat content of that water. Hence, operationally all climate modeling applications assume that

$$\Theta^{\text{precip}} = \Theta_{k=1} \quad \text{climate models}, \quad (8.56)$$

in which case there is no change in ocean temperature upon transfer of precipitating liquid water across the ocean surface.

- Realistic river models carry the heat content of river water and pass this content to the ocean model at river mouths. Following from the discussion surrounding equation (8.36), we may thus write the river contribution to the buoyancy budget in the form

$$-Q_m \alpha (\Theta - \Theta_m) = \alpha \left(-Q_m \Theta + \frac{\mathcal{H}^{\text{liquid runoff}}}{C_p^{\text{liquid runoff}}} \right). \quad (8.57)$$

Depending on the heat content of liquid runoff relative to the sea surface, ocean buoyancy may increase or decrease when liquid runoff enters the ocean.

8.3.9.2 Penetrative radiation

Shortwave radiation is absorbed by seawater as it penetrates from the surface into the upper ocean. Hence, $\delta_k Q_\theta^{\text{pen}} > 0$ so that radiation increases the grid cell buoyancy if $\alpha > 0$, but decreases the buoyancy if $\alpha < 0$.

8.3.9.3 Non-penetrative heating

Longwave, latent, and sensible heating generally cool the upper ocean, and so lead to a decrease in ocean buoyancy for regions where the thermal expansion coefficient, α , is positive. In those few regions where $\alpha < 0$, such as the Baltic, non-penetrative cooling stabilizes the ocean.

8.3.9.4 Salt carried by water transport

The haline contraction coefficient, β , is generally positive. Hence, the term $Q_m \beta (S - S_m)$ increases ocean buoyancy for those cases where the sea surface salinity, $S_{k=1}$, is greater than the salinity of the water transferred across the ocean surface. Most applications assume $S_m = 0$, such as for evaporation and precipitation

$$S^{\text{evap}} = 0 \quad (8.58)$$

$$S^{\text{precip}} = 0. \quad (8.59)$$

However, river models sometimes consider a nonzero salinity of the runoff, in which case

$$S^{\text{liquid runoff}} \neq 0. \quad (8.60)$$

8.3.9.5 Salt fluxes due to sea ice melt and formation

Salt is exchanged with the ocean when sea ice melts and forms. This salt exchange is generally computed as part of a sea ice model, with the ocean model receiving a salt flux Q_S . The term βQ_S can either increase buoyancy (when salt is removed from the liquid ocean as per ice formation) or decrease buoyancy (when salt is added to the liquid ocean as per ice melt). Note that in addition to salt exchange, there is a freshwater exchange upon melting or forming sea ice, with the freshwater exchange also impacting buoyancy as part of the mass flux Q_m discussed earlier.

8.3.10 Buoyancy forcing that acts on the OBL

Equation (8.53) provides an expression for the buoyancy forcing from surface fluxes acting on a surface grid cell. We use that equation to derive an expression for buoyancy forcing on the OBL. The only subtle point concerns the treatment of penetrative shortwave radiation. Rather than consider that radiation leaving the bottom of the surface cell at $z = -\Delta z$, we are now concerned with that leaving the bottom of the boundary layer at $z = -h$. We also multiply this penetrative flux by the thermal expansion coefficient at that depth, rather than the expansion coefficient in the ocean surface cell. In this way we write the buoyancy forcing acting on the boundary layer

$$B_f = \frac{g}{\rho_o} \left[Q_m [-\alpha (\Theta - \Theta_m) + \beta (S - S_m)] + \alpha Q_\theta^{\text{non-pen}} - \beta Q_S \right] + \left[(\alpha Q_\theta^{\text{pen}})_{z=\eta} - (\alpha Q_\theta^{\text{pen}})_{z=-h} \right]. \quad (8.61)$$

This expression can be written as the sum of two terms

$$B_f = -\overline{wb}^0 + B_R. \quad (8.62)$$

The first term takes the form of a kinematic turbulent buoyancy flux at the ocean surface

$$-\overline{wb}^0 = \frac{g}{\rho_o} \left[Q_m [-\alpha (\Theta - \Theta_m) + \beta (S - S_m)] + \alpha Q_\theta^{\text{non-pen}} - \beta Q_S \right], \quad (8.63)$$

where the minus sign on the left hand side accounts for the assumption that $w > 0$ for an upward ocean velocity (see sign convention discussion in Section 8.1.1). The second term accounts for the penetrative radiation, which is neither a turbulent flux nor advective flux

$$B_R = (\alpha Q_\theta^{\text{pen}})_{z=\eta} - (\alpha Q_\theta^{\text{pen}})_{z=-h}. \quad (8.64)$$

The corresponding heat flux convergence onto the boundary layer is given by (see equation (A4) of [Large et al. \(1994\)](#))

$$Q_R = \left(Q_\theta^{\text{pen}} \right)_{z=\eta} - \left(Q_\theta^{\text{pen}} \right)_{z=-h}. \quad (8.65)$$

Notably, B_R , and hence B_f , are two-dimensional functions of the boundary forcing, but only once the boundary layer depth h is known, since it is necessary to remove the shortwave leaving through the bottom of the boundary layer.

We make note of one potential confusing point regarding the situation where $\alpha < 0$, as occurs in regions where the salinity is relatively fresh, such as the Baltic Sea. Surface heating in these regions leads to a negative buoyancy flux, $B_f < 0$, which is contrary to most cases in the open ocean where $\alpha > 0$ is the norm.

8.4 Surface layer and Monin-Obukhov similarity

The semi-empirical Monin-Obukhov similarity theory has proven quite useful in describing general features of boundary layer turbulence active in the atmospheric planetary boundary layer (see, e.g., Section 3.3 of [Kantha and Clayson, 2000](#)). One may thus choose to apply these ideas to the ocean planetary boundary layer, particularly since the atmospheric boundary layer is far better measured than the ocean, and there are certain features that are similar. However, before applying the Monin-Obukhov similarity theory to the ocean, we acknowledge some characteristics of the ocean surface boundary layer that distinguish it from atmospheric boundary layers.

- Surface ocean gravity waves can impact a nontrivial fraction of the ocean surface boundary layer, whereas such waves only impact a small fraction of atmospheric boundary layers.
- The surface ocean velocity is generally the largest velocity in the ocean. In contrast, the surface atmospheric velocity vanishes over land and is relatively small over the ocean.
- The surface ocean absorbs shortwave solar radiation, whereas the atmosphere is nearly transparent to radiation.

Despite these basic distinctions between planetary boundary layers in the atmosphere and ocean, [Large et al. \(1994\)](#) used the Monin-Obukhov similarity theory to introduce scales for turbulent fluctuations and to identify non-dimensional similarity functions in the ocean surface layer.

8.4.1 The surface layer

A molecular layer exists within roughly a millimetre of the upper ocean interface, with this layer dominated by molecular viscous and diffusive effects ([Large, 1998, 2012](#)). Since it is dominated by molecular viscous effects, this layer is not turbulent and thus leads to negligible mixing of tracer and momentum. It is the molecular layer that ultimately transfers properties between the ocean and atmosphere or ice, including momentum and buoyancy. The more this layer is “corrugated” through wave breaking and other turbulent action, the faster properties are transferred across the surface ocean interface.

The ocean *surface layer* (Figure 8.1) is a turbulent layer whose turbulent fluxes are roughly independent of distance from the upper boundary; i.e., the surface layer is nearly a *constant flux* layer. The surface layer starts just beneath the molecular viscous layer. Turbulence within the surface layer delivers properties to the molecular layer for transfer to the atmosphere or ice ([Fairall et al., 1996](#)). Given that no ocean model resolves the molecular sublayer, for purposes of surface flux exchange, the upper ocean interface at $z = \eta(x, y, t)$ in an ocean model operationally starts at the top of the surface layer, and thus excludes the molecular layer.

8.4.2 Monin-Obukhov similarity theory

The surface turbulent layer is of fundamental importance for determining the rate that properties are transferred across the surface ocean interface. It thus plays a key role in how the ocean is forced. If

we needed to model all the details of this layer, then the problem of coupled modeling would perhaps be intractable. Fortunately, the Monin-Obukhov similarity theory has proven to be quite useful in many contexts, particularly for the atmosphere boundary layer. Following [Large et al. \(1994\)](#), we consider its use for the ocean surface boundary layer.

Monin-Obukhov similarity theory assumes that the turbulent surface layer is a constant flux layer that starts just beneath any roughness elements, and certainly beneath the molecular sublayer. In the absence of breaking surface waves, roughness elements arise from capillary waves that allow the wind to affect the otherwise smooth ocean surface, in which case the roughness length is on the order of centimetres. With breaking surface waves, the roughness length can increase to the order of a metre (e.g., see concluding section to [Craig and Banner, 1994](#)). Furthermore, the scalings from Monin-Obukhov are distinctly not correct with surface wave breaking (e.g., [Craig and Banner, 1994](#); [Terray et al., 1996](#)). In the formulation of [Large et al. \(1994\)](#), surface gravity waves are ignored, though we note that including surface waves is the topic of ongoing research (see Section 8.7).

Even if the surface layer is not a constant flux layer, the following scalings are relevant so long as the surface boundary fluxes remain the dominant parameters determining properties of this layer ([Tennekes, 1973](#)). Within the surface layer, the relevant dimensional quantities are the distance d from the surface interface at $z = \eta$ (equation (8.18)), and the surface kinematic fluxes of momentum, tracer, scalars, and buoyancy

$$\overline{w\mathbf{u}}^0 = \text{surface kinematic momentum flux} \quad (8.66)$$

$$\rho_o C_p \overline{w\theta}^0 = \text{surface kinematic heat flux} \quad (8.67)$$

$$\overline{ws}^0 = \text{surface kinematic scalar (e.g., salt) flux} \quad (8.68)$$

$$\overline{wb}^0 = \text{surface kinematic buoyancy flux.} \quad (8.69)$$

We now introduce the following dimensional scales.

- **FRICTION VELOCITY:** From the surface kinematic momentum flux, we introduce the turbulent velocity scale, also known as the *friction velocity* scale

$$u_*^2 \equiv |\overline{w\mathbf{u}}^0|. \quad (8.70)$$

Note that $u_* \geq 0$ since it represents a velocity scale, and so is not a vector. Use of the identity (8.30) provides a means to compute the surface friction velocity given the surface momentum stress

$$\rho_o u_*^2 = |\boldsymbol{\tau}|. \quad (8.71)$$

- **TEMPERATURE SCALE:** From the surface kinematic heat flux and the surface kinematic momentum flux, we define a scale for the surface turbulent temperature fluctuations

$$\Theta_* = - \left(\frac{\overline{w\theta}^0}{\sqrt{|\overline{w\mathbf{u}}^0|}} \right) = - \left(\frac{\overline{w\theta}^0}{u_*} \right). \quad (8.72)$$

The sign is chosen so that turbulent fluxes leading to surface ocean cooling, $\overline{w\theta}^0 > 0$, correspond to a negative turbulent temperature scale, $\Theta_* < 0$, whereas surface heating corresponds to a positive temperature scale, $\Theta_* > 0$.

- **SCALAR SCALE:** From the surface kinematic scalar flux and the surface kinematic momentum flux, we define a scale for the surface turbulent scalar fluctuations

$$S_* = - \left(\frac{\overline{ws}^0}{u_*} \right). \quad (8.73)$$

As for the temperature scale, the sign is chosen so that turbulent fluxes leading to surface loss of scalar, $\overline{ws}^0 > 0$, correspond to a negative turbulent scale, $S_* < 0$.

- **BUOYANCY SCALE:** From the surface kinematic buoyancy flux $-\overline{wb}^0$ (equation (8.63)), and the penetrative buoyancy flux B_R (equation (8.64)), we define a scale for the surface turbulent buoyancy fluctuations

$$B_* = \left(\frac{B_f}{u_*} \right) = \left(\frac{-\overline{wb}^0 + B_R}{u_*} \right). \quad (8.74)$$

A positive buoyancy scale, $B_* > 0$, corresponds to an increase in ocean buoyancy.

8.4.3 Similarity functions and Monin-Obukhov length scale

The Monin-Obukhov similarity theory assumes the vertical gradient of any mean field, Λ , within the surface turbulent layer is a function of the scale Λ_* of its turbulent fluctuations, the buoyancy scale B_* , the velocity scale u_* , and the vertical distance from the upper interface, $d = -z + \eta$ (equation (8.18)). In this case, we write

$$\frac{\partial \Lambda}{\partial z} = \Psi(d, u_*, B_*, \Lambda_*), \quad (8.75)$$

where Ψ is an unknown function. Although no exact analytical expression exists for Ψ , Monin-Obukhov theory suggests that progress can be made by fitting data to the following form

$$\frac{\partial \Lambda}{\partial z} = \left(\frac{\Lambda_*}{\kappa d} \right) \phi_\Lambda(\zeta). \quad (8.76)$$

In this expression,

$$\kappa \approx 0.4 \quad (8.77)$$

is the von Karman constant, $\phi_\Lambda(\zeta)$ is a dimensionless *similarity function* or flux profile that is dependent only on the scaled distance

$$\zeta \equiv \frac{d}{L} \quad (8.78a)$$

$$= \frac{d}{h} \frac{h}{L} \quad (8.78b)$$

$$= \sigma \frac{h}{L} \quad (8.78c)$$

and

$$L = \frac{u_*^2}{\kappa B_*} = \frac{u_*^3}{\kappa B_f} = \frac{|\tau/\rho_o|^{3/2}}{\kappa B_f} \quad (8.79)$$

is the Monin-Obukhov length scale determined by the ratio of the momentum forcing to buoyancy forcing.

The Monin-Obukhov length scale takes on the following values for the suite of available boundary forcing

$$L = \begin{cases} 0 & u_* = 0, B_* \neq 0 & \tau = 0, B_f \neq 0 & \text{zero winds} \\ \infty & u_* \neq 0, B_* = 0 & \tau \neq 0, B_f = 0 & \text{zero buoyancy forcing (neutral forcing)} \\ > 0 & u_* \neq 0, B_* > 0 & \tau \neq 0, B_f > 0 & \text{stabilizing buoyancy forcing} \\ < 0 & u_* \neq 0, B_* < 0 & \tau \neq 0, B_f < 0 & \text{destabilizing or convective buoyancy forcing.} \end{cases} \quad (8.80)$$

Notably, L is *not* the finite positive thickness of the surface turbulent layer (Figure 8.1), as evident since L can be negative or infinite. Instead, L is the depth scale at which buoyancy production of turbulent kinetic energy is of the same magnitude as shear production. For depths shallower than $L > 0$, shear production dominates due to the effects from mechanical forcing through momentum stress τ . The case $L = \infty$ is trivially dominated by shear production since there is no buoyancy forcing. For depths deeper than L , buoyancy production dominates the turbulence. The case of $L < 0$ (convection) is always dominated by buoyancy production.

The similarity function ϕ_Λ appearing in equation (8.76) satisfies the following limit case under neutral forcing (zero buoyancy forcing)

$$\phi_\Lambda(0) = 1 \quad \text{arising from } B_f = 0 \text{ so that } L = \infty \text{ and } \zeta = d/L = 0. \quad (8.81)$$

This limit reduces the more general Monin-Obukhov form for the vertical derivative (8.76) to the logarithmic Law of the Wall form

$$\frac{\partial \Lambda}{\partial z} = \left(\frac{\Lambda_*}{\kappa d} \right) \quad \text{neutral forcing so } \phi_\Lambda = 1. \quad (8.82)$$

In the general case of nonzero buoyancy forcing, we integrate the similarity form (8.76) to expose the logarithmic Law of the Wall for neutral forcing, plus a term present with nonzero buoyancy forcing. For this purpose, rewrite equation (8.76) in terms of the scaled Monin-Obukhov distance, ζ , to have

$$\frac{\partial \Lambda}{\partial \zeta} = - \left(\frac{\Lambda_*}{\kappa \zeta} \right) \phi_\Lambda(\zeta), \quad (8.83)$$

where we used the relation between vertical increments through

$$d\zeta = -L dz \quad (8.84)$$

using $d = -z + \eta$ (equation (8.18)). We now vertically integrate equation (8.83) to have

$$\Lambda(\zeta) = \Lambda(Z_\lambda/L) + \left(\frac{\Lambda_*}{L} \right) \int_{Z_\lambda/L}^{\zeta} \left(\frac{(1 - \phi_\Lambda) - 1}{\zeta'} \right) d\zeta'. \quad (8.85)$$

In this expression,

$$Z_\lambda = \text{roughness length} \quad (8.86)$$

introduced the roughness length associated with each fluctuating field. Within a distance Z_λ or less from the boundary at $z = \eta$, the kinematic fluxes are not expected to be constant due to the impacts from roughness elements. Hence, we expect the Monin-Obukhov similarity theory to breakdown when getting closer than the roughness length to the surface.

Integrating the right hand side of equation (8.85) from the roughness length to an arbitrary point within the surface layer renders²

$$\Lambda(\zeta) = \Lambda(Z_\lambda/L) - \left(\frac{\Lambda_*}{L} \right) \ln(\zeta L/Z_\lambda) + \left(\frac{\Lambda_*}{L} \right) \int_{Z_\lambda/L}^{\zeta} \left(\frac{(1 - \phi_\Lambda)}{\zeta'} \right) d\zeta'. \quad (8.87)$$

As expected, the first term exposes the logarithmic Law of the Wall behaviour occurring for neutral forcing conditions ($\phi_\Lambda = 1$). Deviations from Law of the Wall for non-neutral forcing are embodied in the integral on the right hand side. Recall that values $\zeta < Z_\lambda/L$ are within the roughness elements or molecular sublayer, so the theory cannot be applied there.

Large et al. (1994) (see their page 365) use atmospheric boundary layer results from Tennekes (1973) to set the surface layer thickness to (see Figure 8.1)

$$\epsilon = 0.1 \quad \text{fraction of KPP boundary layer occupied by surface layer.} \quad (8.88)$$

Within the surface layer, atmospheric boundary layer studies indicate that turbulent fluxes are within 20% of their surface values when reaching a distance $d = \epsilon h$ from the upper ocean interface at $d = 0$. The value of $\epsilon = 0.1$ has never been observed in the ocean, but there is no reason to believe it is fundamentally incorrect. Hence, this is the value suggested by Large et al. (1994) for the KPP scheme.

²The result (8.87) disagrees with equation (4) in Large et al. (1994) by a minus sign, with the origin of the minus sign the relation (8.84) between infinitesimal changes in ζ and infinitesimal changes in z .

8.5 Specifying the KPP parameterization

We are now ready to determine the KPP boundary layer depth, h , the diffusivities, K_λ and $K_\lambda^{\text{non-local}}$, and non-local transport, γ_λ , thus enabling a full parameterization of the turbulent flux $\overline{w\lambda}$ according to

$$\overline{w\lambda} = -K_\lambda \left(\frac{\partial \Lambda}{\partial z} \right) + K_\lambda^{\text{non-local}} \gamma_\lambda. \quad (8.89)$$

Recall the diffusivity computed as part of the local flux is given by equation (8.13), rewritten here as

$$K_\lambda(\sigma) = h w_\lambda(\sigma) G_\lambda(\sigma), \quad (8.90)$$

and the non-local diffusivity, $K_\lambda^{\text{non-local}}$ is generally the same as K_λ , with one exception to be discussed in Section 8.5.3. Recall that

$$\sigma = d/h \quad (8.91)$$

is the dimensionless distance from the upper surface normalized by the boundary layer thickness, with

$$d = -z + \eta \quad (8.92)$$

the dimensionful distance.

8.5.1 The turbulent vertical velocity scale w_λ

We now determine the turbulent vertical velocity scale w_λ appearing in equation (8.90). This velocity scale is a function of the surface buoyancy forcing, surface wind forcing, and depth from the ocean surface. We generally assume it is the same for the various scalars

$$w_s = w_\theta. \quad (8.93)$$

Similarly, for stable buoyancy forcing, the turbulent velocity scale for scalars is the same as that for momentum momentum

$$w_s = w_m \quad \text{when } B_f > 0. \quad (8.94)$$

For unstable buoyancy forcing, scalars have a larger velocity scale than momentum

$$w_s > w_m \quad \text{when } B_f < 0. \quad (8.95)$$

We now provide details for the values of the velocity scales.

8.5.1.1 Velocity scale w_λ with stable buoyancy forcing

Following page 370 of Large et al. (1994), we first specify the velocity scale within the Monin-Obukhov surface layer, where $\sigma = d/h < \epsilon = 0.1$. We also assume stable buoyancy forcing, so that the non-local term, γ_λ , vanishes. We later extend these results to the full boundary layer for arbitrary buoyancy forcing.

The similarity result (8.76) holds in the surface layer, in which

$$\frac{\partial \Lambda}{\partial z} = \left(\frac{\Lambda_*}{\kappa d} \right) \phi_\Lambda(\zeta). \quad (8.96)$$

We may eliminate the vertical gradient $\partial \Lambda / \partial z$ using the KPP parameterization (8.89) with a zero non-local term under stable buoyancy forcing

$$\phi_\Lambda = -\frac{\kappa d}{\Lambda_*} \left(\frac{\overline{w\lambda}}{K_\lambda} \right). \quad (8.97)$$

Substituting the turbulent scale $\Lambda_* = -\overline{w\lambda}^0 / u_*$ from equation (8.73) yields

$$K_\lambda \phi_\Lambda = \kappa d u_* \left(\frac{\overline{w\lambda}}{\overline{w\lambda}^0} \right). \quad (8.98)$$

The KPP diffusivity expression (8.90) then renders

$$w_\lambda(\sigma) \sigma^{-1} G_\lambda(\sigma) = \left(\frac{\kappa u_*}{\phi_\Lambda(\sigma)} \right) \left(\frac{\overline{w \lambda}^\sigma}{\overline{w \lambda}^0} \right). \quad (8.99)$$

Recalling that $\sigma < \epsilon = 0.1$ in the surface layer yields the approximate linear relation

$$\sigma^{-1} G_\lambda(\sigma) \approx a_1 + a_2 \sigma, \quad (8.100)$$

where we used expression (8.23) for the shape function $G_\lambda(\sigma)$. Furthermore, within the surface layer, turbulent fluxes for any fluctuating field, $\overline{w \lambda}^\sigma$, are linearly proportional to their surface value, $\overline{w \lambda}^0$. We may thus use this result to specify a part of the shape function according to

$$a_1 + a_2 \sigma = \left(\frac{\overline{w \lambda}^\sigma}{\overline{w \lambda}^0} \right). \quad (8.101)$$

Note that as shown in Section 8.5.3, there is generally a dependence of a_2 on the field λ , whereas

$$a_1 = 1 \quad (8.102)$$

for all fields. With the specification (8.101), we are led to an expression for the turbulent velocity scale within the surface layer

$$w_\lambda(\sigma) = \frac{\kappa u_*}{\phi_\Lambda(\sigma h/L)} \quad \text{for stable forcing } B_f > 0 \text{ and } 0 < \sigma < \epsilon. \quad (8.103)$$

Troen and Mahrt (1986) assume this expression is valid throughout the stably forced boundary layer for $0 < \sigma < 1$, and Large et al. (1994) also make that assumption.

8.5.1.2 Velocity scale w_λ with unstable buoyancy forcing

For unstable buoyancy forcing conditions, $B_f < 0$, the turbulent velocity scales within the surface layer are assumed to be the same as the stable velocity scale (8.103), again within the surface layer. For unstable forcing beneath the surface layer, $\epsilon < \sigma < 1$, Large et al. (1994) cap the velocity scale to that evaluated at the base of the surface layer at $\sigma = \epsilon$.

8.5.1.3 Summarizing properties of the turbulent velocity scale w_λ

The net result for all conditions is that the turbulent vertical velocity scale is given by

$$w_\lambda(\sigma) = \kappa u_* \begin{cases} \phi_\Lambda^{-1}(\sigma h/L) & \text{stable forcing } B_f > 0 & \text{OBL} & 0 < \sigma < 1 \\ 1 & \text{neutral forcing } B_f = 0 & \text{OBL} & 0 < \sigma < 1 \\ \phi_\Lambda^{-1}(\sigma h/L) & \text{unstable forcing } B_f < 0 & \text{M-O surface layer} & \sigma < \epsilon \\ \phi_\Lambda^{-1}(\epsilon h/L) & \text{unstable forcing } B_f < 0 & \text{OBL beneath surface layer} & \epsilon < \sigma < 1. \end{cases} \quad (8.104)$$

We now summarize various properties of the velocity scale, with these properties reflected in Figure 8.3.

- **STABLE FORCING:** The similarity functions ϕ_Λ and velocity scales w_λ satisfy the following properties under positive buoyancy forcing, $B_f > 0$.
 - The similarity functions are increased so that the turbulent velocity scales are reduced.
 - The similarity functions are the same for all scalars and momentum, so that the velocity scales w_λ are the same.
- **NEUTRAL FORCING:** with zero buoyancy forcing, $B_f = 0$, the similarity functions satisfy $\phi_\Lambda = 1$, so that $w_\lambda(\sigma) = \kappa u_*$ is independent of both the species being mixed and the position within the boundary layer. This case is useful to test the integrity of the code. For example, consider a wind stress with magnitude $|\tau| = 0.2 \text{ N m}^{-2}$ and reference density $\rho_o = 1035 \text{ kg m}^{-3}$, so that the friction velocity is $u^* = \sqrt{|\tau|/\rho_o} = 0.014 \text{ m s}^{-1}$. The turbulent velocity scale is then the constant $w_\lambda = \kappa u^* = 0.0056 \text{ m s}^{-1}$.

- UNSTABLE FORCING: The similarity functions ϕ_Λ and velocity scales w_λ satisfy the following properties under negative buoyancy forcing, $B_f < 0$.

- The similarity functions ϕ_Λ are reduced so that the turbulent velocity scales w_λ are enhanced.
- The similarity functions for momentum are larger than those for scalars, so that the velocity scales for momentum are smaller than for scalars

$$w_m < w_s. \quad (8.105)$$

- In the convective limit, for which $u_* \rightarrow 0$, the velocity scales behave according to

$$w_\lambda \sim w_* = (-B_f h)^{1/3}. \quad (8.106)$$

In order to satisfy this scaling, the similarity functions ϕ_Λ must have the form

$$\phi_\Lambda = (a_\lambda - c_\lambda \zeta)^{-1/3} \quad \text{convective conditions with } u_* \rightarrow 0, \quad (8.107)$$

where $\zeta = d/L = \sigma h/L \ll 0$, and the constants a_λ and c_λ are chosen to match the convective form (8.107) to less unstable forms.

We now use the expression (8.107) within the unstable surface layer ($\sigma < \epsilon$) form in (8.104) to render

$$w_\lambda = \kappa u_* (a_\lambda - c_\lambda \zeta)^{1/3} \quad (8.108a)$$

$$= \kappa (a_\lambda u_*^3 - c_\lambda u_*^3 \zeta)^{1/3} \quad (8.108b)$$

$$= \kappa [a_\lambda u_*^3 - c_\lambda u_*^3 (h\sigma/L)]^{1/3} \quad (8.108c)$$

$$= \kappa (a_\lambda u_*^3 - c_\lambda \sigma \kappa h B_f)^{1/3} \quad (8.108d)$$

$$= \kappa (a_\lambda u_*^3 + c_\lambda \sigma \kappa w_*^3)^{1/3} \quad (8.108e)$$

$$\rightarrow \kappa w_* (c_\lambda \sigma \kappa)^{1/3}, \quad (8.108f)$$

where the final limit case is for the convective limit with $u_* \rightarrow 0$. Likewise, outside the surface layer ($\epsilon < \sigma < 1$) we have from equation (8.104)

$$w_\lambda = \kappa (a_\lambda u_*^3 + c_\lambda \epsilon \kappa w_*^3)^{1/3} \rightarrow \kappa w_* (c_\lambda \epsilon \kappa)^{1/3}, \quad (8.109)$$

where again the final limit case is for the convective limit with $u_* \rightarrow 0$.

8.5.1.4 Summarizing some useful test cases for the turbulent velocity scale

In developing the KPP scheme, and testing its implementation within any particular ocean model, it is important to identify test cases where the behaviour can be compared against analytical expressions. There are two rather useful limits that allow for testing the integrity of the CVMix code. The first limit is the neutral forcing case where $B_f = 0$, so that the turbulent velocity scale is a constant for all species and is given by

$$w_\lambda = \kappa u^* \quad B_f = 0. \quad (8.110)$$

We gave an example above in which $|\tau| = 0.2 \text{ N m}^{-2}$ yields $w_\lambda = \kappa u^* = 0.0056 \text{ m s}^{-1}$.

The second test case is the convective limit with $u_* = 0$ and $B_f < 0$. We can evaluate the turbulent velocity scale analytically according to equation (8.109). For example, consider the case where heat is being extracted from the ocean at a rate of $Q^{\text{non-pen}} = C_p^o Q_\theta^{\text{non-pen}} = -100 \text{ W m}^{-2}$, and assume there are no other sources of buoyancy forcing. The surface buoyancy flux in this case is then given by

$$B_f = \left(\frac{g \alpha}{\rho_o C_p^o} \right) Q^{\text{non-pen}} \quad (8.111a)$$

$$= \left(\frac{9.8 \text{ m s}^{-2} \times 2.5 \times 10^{-4} \text{ }^\circ\text{C}^{-1}}{1035 \text{ kg m}^{-3} \times 3992 \text{ J kg}^{-1} \text{ }^\circ\text{C}^{-1}} \right) (-100 \text{ W m}^{-2}) \quad (8.111b)$$

$$= -5.9 \times 10^{-8} \text{ m}^2 \text{ s}^{-3}. \quad (8.111c)$$

To reach this result we took $g = 9.8 \text{ m s}^{-2}$, $\alpha = 2.5 \times 10^{-4} \text{ }^\circ\text{C}^{-1}$, $\rho_o = 1035 \text{ kg m}^{-3}$, and $C_p = 3992 \text{ J kg}^{-1} \text{ }^\circ\text{C}^{-1}$. Let us further assume the ocean has neutral stratification (i.e., uniform temperature and salinity), in which case a negative buoyancy flux produces a boundary layer depth reaching to the ocean bottom, assumed to be 6000 m. The velocity scale w_* then takes the value

$$w_* = (-B_f h)^{1/3} \quad (8.112a)$$

$$= (5.9 \times 10^{-8} \text{ m}^2 \text{ s}^{-3} \times 6000 \text{ m})^{1/3} \quad (8.112b)$$

$$= 0.07 \text{ m s}^{-1}. \quad (8.112c)$$

The vertical turbulent velocity scale for scalars is then given by

$$w_s = \kappa w_* (c_s \epsilon \kappa)^{1/3} \quad (8.113a)$$

$$= 0.044 \text{ m s}^{-1}, \quad (8.113b)$$

where we used $\epsilon = 0.1$, $\kappa = 0.4$, and $c_s = 98.86$.

8.5.2 Similarity functions ϕ_Λ

The vertical velocity scales are functions of the similarity functions ϕ_Λ , also called the dimensionless flux profiles. Appendix B of [Large et al. \(1994\)](#) present analytic forms for these functions, based on fits to available data, with their Figure B1 (reproduced here as Figure 8.4) providing a summary of the choices for the momentum function ϕ_m and the scalar function ϕ_s . Both functions agree for stable buoyancy forcing, in which they depend linearly on the dimensionless Monin-Obukhov length $\zeta = d/L = \sigma h/L$. We now discuss the more complex case of unstable buoyancy forcing.

8.5.2.1 The [Large et al. \(1994\)](#) choices for unstable buoyancy forcing

For unstable buoyancy forcing, where $L < 0$ and so $\zeta < 0$, there are two regimes. The scalar function ϕ_s is always less than the momentum function ϕ_m . Hence, for unstable forcing there is a larger turbulent velocity scale for the scalars than momentum ($w_s > w_m$), and thus a larger vertical diffusivity for scalars than momentum ($K_s > K_m$). The turbulent Prandtl number, Pr , is given by the ratio of the flux functions

$$\text{Pr} = \frac{K_m}{K_s} = \frac{w_m}{w_s} = \frac{\phi_m}{\phi_s}. \quad (8.114)$$

The choices made by [Large et al. \(1994\)](#) lead to a Prandtl number in the convective limit ($\zeta \rightarrow -\infty$) of

$$\text{Pr} \rightarrow \left(\frac{c_m}{c_s} \right)^{1/3} = 0.44. \quad (8.115)$$

The coefficients c_m and c_s are parameters in the similarity functions ϕ_m and ϕ_s , respectively. Assuming the forms for the similarity functions given by [Large et al. \(1994\)](#), their Appendix B suggests the following values

$$c_s = 98.96 \quad (8.116a)$$

$$c_m = 8.38. \quad (8.116b)$$

If different forms for the similarity functions are used, such as proposed in Section 8.5.2.2, then different fit values will need to be used.

8.5.2.2 Alternative choices for unstable buoyancy forcing

[Large et al. \(1994\)](#) chose two regimes for the unstable buoyancy forced range, transitioning from different fractional exponents near $\zeta = 0$, to the same $-1/3$ power for larger negative ζ . The scalar function ϕ_s falls off faster near $\zeta = 0$, with a power $-1/2$, whereas the momentum function ϕ_m falls off with a $-1/4$ power.

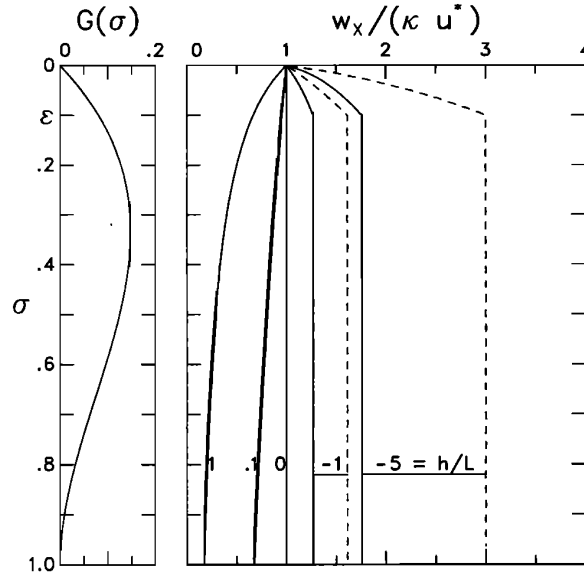


Figure 8.3: This is a reproduction of Figure 2 from [Large et al. \(1994\)](#). The vertical axis is the dimensionless vertical coordinate $\sigma = d/h$ within the KPP boundary layer $0 \leq \sigma \leq 1$. The left panel shows the vertical profile of the shape function, $G_\lambda(\sigma)$, used to scale the vertical diffusivity via equation (8.90). The analytic form shown here is given by the universal form (equation (8.157)) $G_{\text{universal}}(\sigma) = \sigma(1-\sigma)^2$ which corresponds to the [Troen and Mahrt \(1986\)](#) form and which is independent of the quantity Λ being diffused. This is the form recommended for CVMix use. [Large et al. \(1994\)](#) chose a more general form, based on the desire to match boundary layer diffusivities to interior diffusivities in which case the shape function becomes a function of λ . We detail the problems with this general approach in Section 8.5.3. The right panel shows various examples of the normalized turbulent velocity scale w_λ (called w_x in [Large et al. \(1994\)](#)), with the examples differing by the value of the dimensionless ratio h/L between the boundary layer depth, h , and the Monin-Obukhov length scale L . For unstable buoyancy forcing, $L < 0$, the velocity scale for scalars, w_s (dashed lines), is greater than that for momentum, w_m (solid lines). For stable forcing, $L > 0$, and both scalar and momentum have the same turbulent velocity scales, $w_s = w_m$. In general, the turbulent velocity scale is enhanced with unstable surface buoyancy forcing, and reduced with stable buoyancy forcing. Note how in the unstable forcing regime, with $L < 0$, the turbulent velocity scales are capped at their $\sigma = \epsilon$ values according to the discussion in Section 8.5.1.2.

This initial distinct fractional power falloff sets the scale for the Prandtl number in this portion of ζ in the weakly unstable regime.

Having two regimes for the negative buoyancy forcing adds complexity to the algorithm. We thus consider how well the original two-regime forms for ϕ_m and ϕ_s can be fit using a single regime, using only the fractional power $-1/3$. Tests suggest that the following forms may be suitable

$$\phi_m(\zeta) = \begin{cases} 1 + 5\zeta & \zeta > 0 \\ (1 - 9\zeta)^{-1/3} & \zeta < 0 \end{cases} \quad (8.117)$$

$$\phi_s(\zeta) = \begin{cases} 1 + 5\zeta & \zeta > 0 \\ (1 - 60\zeta)^{-1/3} & \zeta < 0. \end{cases} \quad (8.118)$$

A comparison of the original forms from [Large et al. \(1994\)](#) to the alternative forms is shown in Figure 8.5. Also shown is the ratio of these two functions which yields the turbulent Prandtl number according to equation (8.114). The agreement between the original forms and the new forms is worse when considering the Prandtl number. As discussed in the figure caption, a viable means for simplifying the turbulent

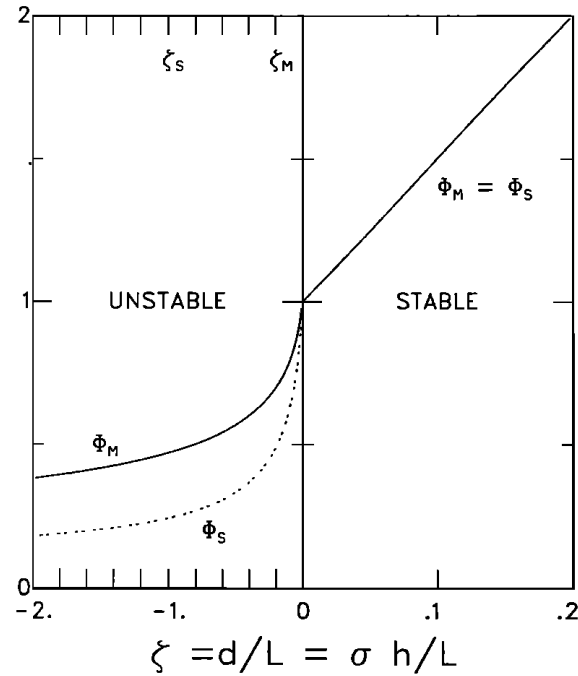


Figure 8.4: This is a reproduction of Figure B1 from [Large et al. \(1994\)](#). The vertical axis provides values for the dimensionless flux profiles, ϕ_λ , for momentum and scalars, and the horizontal axis gives the dimensionless Monin-Obukhov length scale $\zeta = d/L = \sigma h/L$. There is a transition across the neutrally forced value of $\zeta = 0$. For stable buoyancy forcing ($\zeta > 0$), both functions are the same, $\phi_s = \phi_m$, and are linear functions of ζ . For unstable buoyancy forcing ($\zeta < 0$), the scalar function is less than momentum, $\phi_s < \phi_m$, with both functions falling off with a negative fractional power. The analytic forms for the functions are given by equations (B1) and (B2) in [Large et al. \(1994\)](#).

functions, without compromising much on the values used in [Large et al. \(1994\)](#), is to maintain original 3-region ϕ_s form, but to simplify ϕ_m to 2-regions according to equation (8.117).

The simplified forms for the similarity functions ϕ_s and ϕ_m have *not* been implemented in CVMix. More testing is required.

8.5.3 The shape function $G_\lambda(\sigma)$ as per [Large et al. \(1994\)](#)

The vertical shape function $G_\lambda(\sigma)$ is given by the cubic polynomial

$$G_\lambda(\sigma) = a_0 + a_1 \sigma + a_2 \sigma^2 + a_3 \sigma^3. \quad (8.119)$$

As already noted when introducing this cubic expression (equation (8.23)), turbulent eddies do not cross the ocean surface at $\sigma = 0$, so the diffusivity should vanish at $\sigma = 0$. This constraint is satisfied by setting

$$a_0 = 0. \quad (8.120)$$

We now discuss further constraints to specify the remaining coefficients. For this purpose, we follow the general approach from [Large et al. \(1994\)](#), in which the shape function is determined by matching boundary layer diffusivity to the interior diffusivity. It is this matching that can lead to distinct shape functions for tracers, given that the interior diffusivities can differ between tracers. We question this matching method in Section 8.5.5, where we propose to use the universal shape function given by equation (8.157), and as used in the atmosphere by [Troen and Mahrt \(1986\)](#) (see Figure . 8.3).

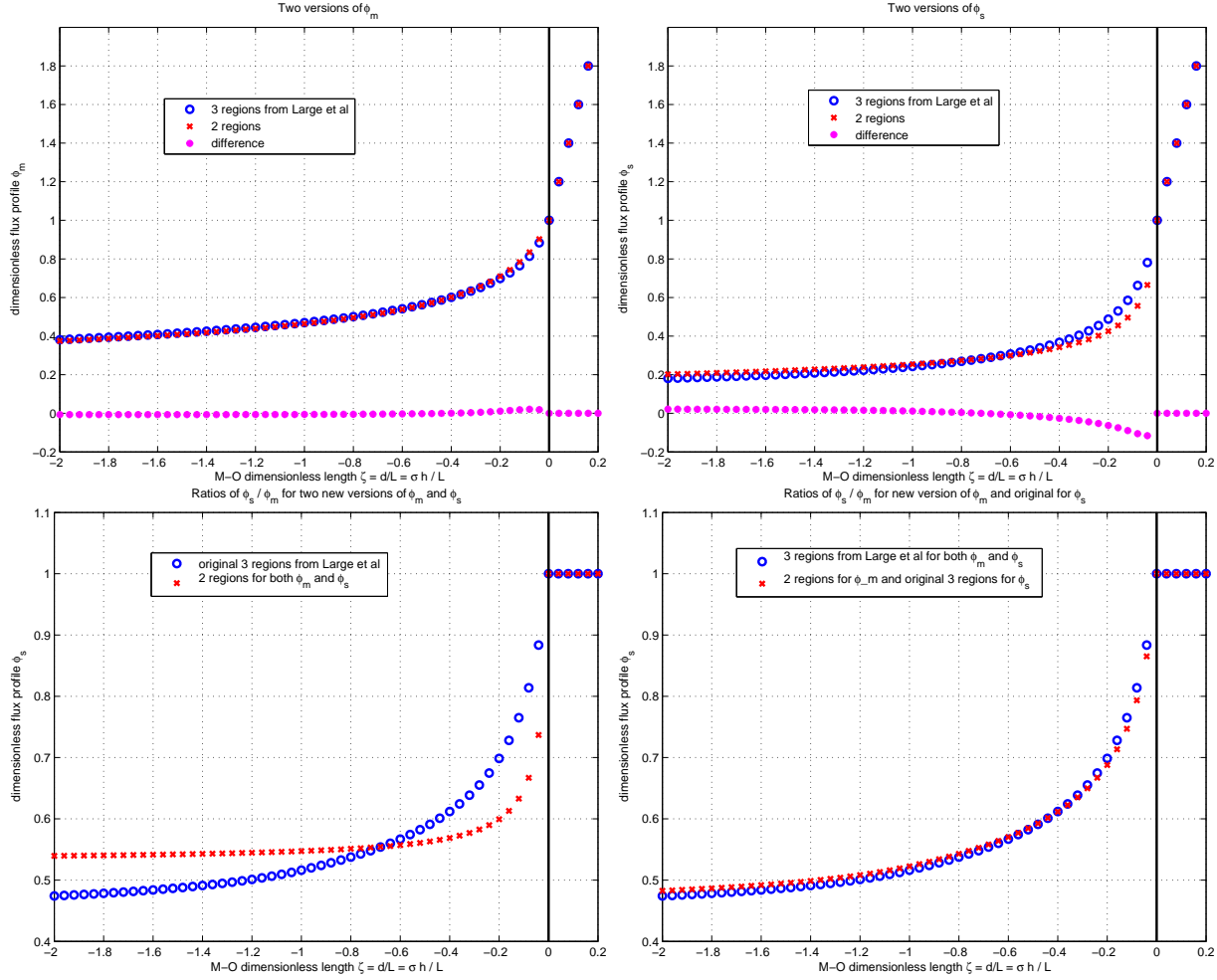


Figure 8.5: Shown here are 2-region flux profiles given by equations (8.117) and (8.118) as compared to the original 3-region profiles from Large et al. (1994). We also show the ratio, ϕ_s/ϕ_m , which defines the turbulent Prandtl number or the ratio of the vertical momentum viscosity to vertical tracer diffusivity. The top left panel shows the original 3-region ϕ_m as compared to the 2-region form (8.117). The agreement is quite close. The top right panel shows the comparison for ϕ_s , with the agreement not very good. The lower left panel shows the ratio ϕ_s/ϕ_m for the original 3-region functions and the new 2-region functions. Their ratio amplifies the problems with the new ϕ_s form (8.118). The lower right panel shows the ratio of the original 3-region ϕ_s to the new 2-region form of ϕ_m . These results suggest that to remain consistent with the original Large et al. (1994) results, it is feasible to switch to the 2-region form (8.117) for ϕ_m , but we must maintain the original 3-region form of ϕ_s .

8.5.3.1 Constraints arising from the surface boundary condition at $\sigma = 0$

We start by rewriting the expression (8.101) that expresses the ratio of turbulent fluxes within the surface layer to those at the surface boundary

$$a_1 + a_2 \sigma = \left(\frac{\overline{w \lambda}^\sigma}{\overline{w \lambda}^0} \right) \quad \text{surface layer: } 0 \leq \sigma \leq \epsilon. \quad (8.121)$$

Satisfying this relation at the ocean surface, $\sigma = 0$, requires

$$a_1 = 1, \quad (8.122)$$

so that

$$1 + a_2 \sigma = \left(\frac{\overline{w \lambda}^\sigma}{\overline{w \lambda}^0} \right) \quad \text{surface layer: } 0 \leq \sigma \leq \epsilon. \quad (8.123)$$

Now define the ratio

$$\beta_\lambda = \left(\frac{\overline{w \lambda}^\epsilon}{\overline{w \lambda}^0} \right), \quad (8.124)$$

which is the ratio of the turbulent flux at the base of the surface layer, $\sigma = \epsilon$, to the flux at the upper ocean interface, $d = -z + \eta = 0$. For atmospheric boundary layers, [Troen and Mahrt \(1986\)](#) set

$$\beta_\lambda = 2 \epsilon \quad \text{atmospheric boundary layers,} \quad (8.125)$$

with $\epsilon = 0.1$. [Troen and Mahrt \(1986\)](#) further assume both the shape function and its first derivative vanish at the base of the boundary layer, $\sigma = 1$. These assumptions lead to the cubic expression valid for all fluctuating fields λ

$$G_{\text{universal}}(\sigma) = \sigma(1 - \sigma)^2 \quad \text{for } G(\sigma = 0) = G(\sigma = 1) = G'(\sigma = 1) = 0, \quad (8.126)$$

with this function exhibited in the left panel of Figure 8.3. We return to this function in Section 8.5.5, where we recommend it be used for the CVMix implementation of KPP.

8.5.3.2 Constraints arising from matching at $\sigma = 1$

[Large et al. \(1994\)](#) also assume the surface layer is 10% of the boundary layer, so that

$$\epsilon = 0.1 \quad \text{KPP scheme.} \quad (8.127)$$

However, they consider a more general approach for the shape function. The reason [Large et al. \(1994\)](#) wish to generalize the atmospheric approach of [Troen and Mahrt \(1986\)](#) is to allow surface ocean boundary layer turbulence to be impacted by interior mixing, with this mixing parameterized by downgradient vertical diffusion. Such diffusion generally introduces distinct diffusivities for tracers (e.g., double diffusion) as well as for momentum (e.g., non-unit Prandtl number). For these reasons, [Large et al. \(1994\)](#) propose to have both the diffusivity and its vertical derivative match across the base of the boundary layer at $\sigma = 1$. These two matching conditions lead to constraints given by equation (18) in [Large et al. \(1994\)](#), which in turn leads to shape functions that are dependent on the field being transported. In practice, satisfying these matching conditions is not straightforward in an ocean model given the difficulties of estimating vertical derivatives of diffusivities. We also note that matching to nonzero interior diffusivities means that the non-local transport term does not smoothly go to zero at the base of the mixed layer. We return to these points in Section 8.5.5. For the meantime, we continue to present the prescription as proposed by [Large et al. \(1994\)](#), as this approach is that which has been implemented in the NCAR models using KPP.

It is critical note that if we allow the interior mixing coefficients to influence the KPP boundary layer diffusivities via the matching conditions at $\sigma = 1$, then the KPP calculation should be called *after* the various methods used to compute interior diffusivities (e.g., double diffusion, tide mixing, shear mixing). This ordering is reflected in the CVMix flow diagram in Figure 1.1. The alternative approach recommended in Section 8.5.5 allows for arbitrary ordering.

8.5.3.3 Vanishing derivative at $\sigma = 1$

Matching both the shape function and its vertical derivative across the boundary layer base at $\sigma = 1$ adds complexity to the KPP algorithm. Furthermore, it is unclear how accurate one can in fact satisfy both matching conditions on a finite grid with potentially coarse vertical spacing at the boundary layer base. To simplify the KPP algorithm, we drop the need to match the vertical derivative of the diffusivity. Instead, we

assume continuity of the diffusivity with a vanishing derivative at the boundary layer base, $\sigma = 1$. Setting $\partial_\sigma G(\sigma) = 0$ at $\sigma = 1$ leads to the relation

$$\left(\frac{\partial G(\sigma)}{\partial \sigma} \right)_{\sigma=1} = 0 \implies 3a_3 = -(1 + 2a_2). \quad (8.128)$$

Matching diffusivities at $\sigma = 1$ between the boundary layer and interior value leads to

$$a_2 = -2 + \left(\frac{3K_\lambda(h)}{hw_\lambda(h)} \right), \quad (8.129)$$

where the diffusivity $K_\lambda(h)$ is determined by parameterizations of interior mixing. Substituting this expression for a_2 into equation (8.128) for a_3 leads to

$$a_3 = 1 - \left(\frac{2K_\lambda(h)}{hw_\lambda(h)} \right). \quad (8.130)$$

The resulting form for $G_\lambda(\sigma)$ is given by

$$G_\lambda(\sigma) = \sigma(1-\sigma)^2 + \sigma^2(3-2\sigma) \left(\frac{K_\lambda(h)}{hw_\lambda(h)} \right) \quad \text{for } G_\lambda(\sigma=0) = G'_\lambda(\sigma=1) = 0. \quad (8.131)$$

Notice how the shape function reduces to the simpler form $G(\sigma) = \sigma(1-\sigma)^2$ when matching to a zero diffusivity, $K_\lambda(h) = 0$, at the boundary layer base (see equation (8.126)).

8.5.4 The non-local term γ_λ as per Large et al. (1994)

We now consider the parameterization for the non-local transport (see Section 8.1.4) as suggested by Large et al. (1994). Again, the KPP parameterization takes the form (equation (8.9))

$$\overline{w\lambda} = -K_\lambda \left(\frac{\partial \Lambda}{\partial z} - \gamma_\lambda \right), \quad (8.132)$$

where we set

$$K_\lambda^{\text{non-local}} = K_\lambda. \quad (8.133)$$

In this way, the non-local portion of the turbulent flux is parameterized according to

$$\overline{w\lambda}^{\text{non-local}} = K_\lambda \gamma_\lambda, \quad (8.134)$$

where K_λ takes the form in equation (8.90):

$$K_\lambda(\sigma) = hw_\lambda(\sigma) G_\lambda(\sigma). \quad (8.135)$$

For completeness, we repeat elements of the outline presented in Section 8.1.4.

8.5.4.1 General features of γ_λ with the KPP parameterization

- Smyth et al. (2002) consider a non-local term for momentum. Until their ideas have been fully tested in climate models, we follow recommendations from Large et al. (1994), who set the non-local momentum term to zero:

$$\gamma_\lambda = \begin{cases} 0 & \text{if } \lambda = (u, v, w) \text{ a velocity component} \\ \neq 0 & \text{nonzero if } \lambda = \theta, s \text{ or another tracer.} \end{cases} \quad (8.136)$$

- The non-local transport is non-zero only within the OBL:

$$\gamma_\lambda = \begin{cases} 0 & \text{if } \sigma > 1 \\ \neq 0 & \text{if } 0 \leq \sigma \leq 1. \end{cases} \quad (8.137)$$

- The non-local transport is non-zero only in the presence of destabilizing negative surface ocean buoyancy flux:

$$\gamma_\lambda = \begin{cases} 0 & \text{for } B_f > 0 \\ \neq 0 & \text{for } B_f < 0. \end{cases} \quad (8.138)$$

- The non-local transport for temperature and arbitrary scalars is given by the following form for destabilizing negative surface ocean buoyancy fluxes:

$$\gamma_\theta = C_s \left(\frac{\overline{w\theta}^0 - Q_R/(\rho_o C_p^o)}{h w_\theta(\sigma)} \right) \quad (8.139)$$

$$\gamma_s = C_s \left(\frac{\overline{ws}^0}{h w_s(\sigma)} \right), \quad (8.140)$$

where

$$C_s = C_* \kappa (c_s \kappa \epsilon)^{1/3}, \quad (8.141)$$

with

$$C_* = 10, \quad (8.142)$$

and Q_R is the heat flux from penetrative radiation given by equation (8.65). We follow here the approach of [Large et al. \(1994\)](#), in which they include shortwave flux, Q_R , as part of the non-local term (e.g., see equation (20) in [Large et al. \(1994\)](#)). Note that equation (8.139) uses c_s regardless of the scalar tracer field considered. We have more to say in Section 8.5.6 regarding the shortwave flux and the non-local term.

Combining the parameterizations (8.139) and (8.140) for the non-local term γ_λ , with that for the vertical diffusivity K_λ in equation (8.135) renders the non-local flux parameterization in the form

$$\overline{w\theta}^{\text{non-local}} = K_\theta \gamma_\theta = G_\theta(\sigma) C_s \left(\overline{w\theta}^0 - Q_R/(\rho_o C_p^o) \right) \quad (8.143)$$

$$\overline{ws}^{\text{non-local}} = K_s \gamma_s = G_s(\sigma) C_s \left(\overline{ws}^0 \right). \quad (8.144)$$

Notice how explicit dependence on both the turbulent velocity scale, w_λ , and boundary layer depth, h , drop out from the parameterization of the non-local flux.

The expressions (8.143) and (8.144) exhibit how the non-local transport provides a redistribution of the surface boundary flux into the boundary layer. This formulation of the KPP non-local transport is key to understanding its role in the boundary layer parameterization. The redistribution of surface fluxes by KPP is analogous to the way surface shortwave radiation is distributed through the upper ocean via penetrative radiation. The key difference is that shortwave penetration is a function of ocean optics, whereas the KPP non-local redistribution is a function of the boundary layer turbulence. Furthermore, the shortwave penetration occurs via an exponential attenuation function (such as those described by [Manizza et al. \(2005\)](#)), rather than an algebraic function used in KPP.

8.5.4.2 Summary of the non-local transport parameterization

We now summarize the non-local transport for temperature and arbitrary scalars, with [Large et al. \(1994\)](#) proposing a parameterization according to the following expression, again valid just for destabilizing negative surface ocean buoyancy fluxes (it vanishes for stable buoyancy forcing):

$$\gamma_\theta = C_s \left(\frac{\overline{w\theta}^0 - Q_R/(\rho_o C_p^o)}{h w_\theta(\sigma)} \right) \quad (8.145)$$

$$\gamma_s = C_s \left(\frac{\overline{ws}^0}{h w_s(\sigma)} \right). \quad (8.146)$$

In these expressions, we have (equation (8.141))

$$C_s = C_* \kappa (c_s \kappa \epsilon)^{1/3}, \quad (8.147)$$

with Large et al. (1994) suggesting the value of

$$C_* = 10, \quad (8.148)$$

whereas $C_* = 5$ in Smyth et al. (2002). The von Karman constant $\kappa = 0.40$ (equation (8.77)) appears in this expression, as well as the fraction of the boundary layer assumed to be occupied by the Monin-Obukhov surface layer

$$\epsilon = 0.1. \quad (8.149)$$

The coefficient $c_s = 98.96$ (equation (8.116b)) is set according to the similarity function ϕ_s (Section 8.5.2). Plugging in the constants suggested by Large et al. (1994) leads to

$$C_s \approx 6.33. \quad (8.150)$$

The flux $Q_R > 0$ appearing in the γ_θ expression for equation (8.145) is the heat flux crossing the ocean surface from shortwave radiation. We split this penetrative shortwave flux from the non-penetrative heat flux $\overline{w\theta}^0$, which is positive for cases where heat leaves the ocean surface due to non-penetrative heat fluxes (i.e., longwave, sensible, and latent). The net heat flux crossing the ocean surface is given by

$$Q^{\text{heat}} = Q_R - \rho_o C_p^o \overline{w\theta}^0, \quad (8.151a)$$

$$= Q_R + C_p^o Q_\theta^{\text{non-pen}}, \quad (8.151b)$$

where $Q^{\text{heat}} > 0$ for heat entering the ocean, and $C_p^o Q_\theta^{\text{non-pen}}$ is the non-penetrative heat fluxes arising from longwave, latent, and sensible heating (Section 8.3.5). The parameterized non-local transport term thus takes the following form for temperature

$$\gamma_\theta = - \left(\frac{C_s}{\rho_o C_p^o} \right) \frac{Q^{\text{heat}}}{h w_\theta(\sigma)}. \quad (8.152)$$

Generally the negative buoyancy forcing that gives rise to the non-local transport is associated with cooling ($Q^{\text{heat}} < 0$), so that

$$\gamma_\theta > 0 \quad \text{surface cooling.} \quad (8.153)$$

Similar considerations lead to the non-local transport term for scalars such as salt

$$\gamma_s = -C_s \left(\frac{Q^s}{h w_s(\sigma)} \right), \quad (8.154)$$

where $Q^s > 0$ when scalar enters through the ocean surface (Section 8.1.1).

Combining the parameterizations (8.152) and (8.146) for the non-local term γ_λ , with that for the vertical diffusivity K_λ in equation (8.13) renders the non-local flux parameterization for temperature and an arbitrary scalar in the form (again, $B_f < 0$ for non-zero non-local transport)

$$\overline{w\theta}^{\text{non-local}} = K_\theta \gamma_\theta = -G_\theta(\sigma) C_s \left(\frac{Q^{\text{heat}}}{\rho_o C_p^o} \right) \quad (8.155a)$$

$$\overline{ws}^{\text{non-local}} = K_s \gamma_s = -G_s(\sigma) C_s Q^s. \quad (8.155b)$$

Notice how explicit dependence on both the turbulent velocity scale, w_λ , and boundary layer depth, h , drop out from the parameterization of the non-local flux. For the CVMix implementation of the non-local transport, the CVMix code computes the products $G_\theta(\sigma) C_s$ and $G_s(\sigma) C_s$, and returns them to the calling model, which then computes the non-local flux upon multiplication by the boundary flux. In this way we see explicitly how the non-local transport provides a redistribution of the surface boundary flux into the boundary layer.

8.5.5 The shape function and non-local transport: Part I

The discussion of the shape function $G_\lambda(\sigma)$ in Section 8.5.3 and the non-local term γ_λ in Section 8.5.4 follow the general prescription from Large et al. (1994). However, there are problems with this prescription related to the non-local transport that motivate use of the universal shape function (8.157) for the diffusivity $K_\lambda = K_\lambda^{\text{non-local}}$.

8.5.5.1 Problem I: non-local flux larger than surface flux

The first problem with the Large et al. (1994) prescription relates to cases where the parameterized non-local flux, (8.143) of (8.144), is larger than the surface tracer flux

$$G_\lambda(\sigma)C_s > 1 \quad \text{non-local flux greater than surface flux.} \quad (8.156)$$

The non-local transport is meant to redistribute the surface flux through the boundary layer. However, values for $G_\lambda(\sigma)C_s > 1$ mean the non-local flux is itself larger than the surface boundary flux. Experience has shown that one may realize $G_\lambda(\sigma)C_s > 1$ near the boundary layer base, $\sigma = 1$, when the interior diffusivity is relatively large. The matching conditions employed by Large et al. (1994) (Section 8.5.3) then lead to a relatively large value for the shape function $G_\lambda(\sigma)$. In this case, one may be exposed to the production of extrema in the tracer field. In the presence of sea-ice, problems may arise particularly in fresh water regions such as the Baltic Sea where the thermal expansion coefficient is negative, $\alpha < 0$ (Martin Schmidt, personal communication).

The following modifications to the original Large et al. (1994) scheme have been found useful to reduce the potential for realizing $G_\lambda(\sigma)C_s > 1$.

- **INTERIOR GRAVITATIONAL INSTABILITIES:** When the vertical stratification is unstable ($N^2 < 0$), vertical diffusivity is enhanced to remove the gravitational instability. Notably, it is *not* appropriate to enhance the diffusivity within the KPP boundary layer, beyond that already computed via the KPP scheme, even when $N^2 < 0$. On those occasions when the instabilities appear beneath the boundary layer, diffusivities are enhanced. If one insisted that such diffusivities should match those in the boundary layer, then the shape function $G_\lambda(\sigma)$ would indeed become quite large in magnitude, thus leading to $G_\lambda(\sigma)C_s > 1$. Hence, NCAR recommends that one pull the “convective adjustment” portion of the mixing scheme outside of the KPP portion of the algorithm. That is, the interior convective instability diffusivities are *not* matched to the KPP boundary layer diffusivities. This is the key reason that NCAR implements KPP prior to the calculation of diffusivities arising from gravitational instabilities.
- **SIMPLER MATCHING:** As noted in Section 8.5.3, one may choose to simplify the matching at the boundary layer base. The simpler approach assumes that only the diffusivities match across the boundary layer base, rather than also insisting on the derivative of the diffusivities as proposed by Large et al. (1994). The simplified matching condition leads to less problems computing discrete vertical derivatives of the diffusivities, and in turn produces more well regularized diffusivities and shape functions. This approach has not been fully tested, but is compelling in theory.

8.5.5.2 Problem II: spuriously large divergence

By definition, the non-local transport vanishes beneath the boundary layer where $\sigma > 1$. However, the diffusivity generally does not vanish beneath the boundary layer. Hence, by determining the shape function $G_\lambda(\sigma)$ according to the needs of diffusivity matching, then the non-local transport will in turn have a jump at the boundary layer base. Only for those cases where the interior diffusivity vanishes will both the diffusivity and the non-local transport have a smooth transition from the boundary layer into the interior.

The jump in the non-local transport is unphysical, and it is a problem exacerbated in the following situations.

- In relatively shallow waters where bottom induced mixing from tides may produce a sizable diffusivity reaching into the boundary layer, then the matching condition will create a relatively large value for $G_\lambda(\sigma)C_s$ at the boundary layer base, thus enhancing the jump across the boundary layer base.

- Refining the vertical grid spacing increases the magnitude of the divergence at the boundary layer base.

8.5.5.3 Resolution I: two shape functions

The fundamental problem is that the non-local transport parameterization proposed by [Large et al. \(1994\)](#) does not smoothly approach zero at the boundary layer base in those cases where the interior diffusivity is nonzero. Its adverse effects may be mild for models with either small interior diffusivities or with coarse vertical grid spacing. However, modern global models, and many regional models, are pushing the limits where interior mixing is sizable and vertical grid spacing refined.

One solution to this problem is to use two distinct structure functions: one for the diffusivity K_λ and another for $K_\lambda^{\text{non-local}}$. The K_λ shape function, $G_\lambda(\sigma)$ will remain as originally proposed by [Large et al. \(1994\)](#), with matching to the interior diffusivity along with the caveats noted above. However, for the non-local transport, we propose to use the cubic function (8.126) for all tracers

$$G_{\text{universal}}(\sigma) = \sigma(1 - \sigma)^2 \quad \text{for } \sigma \leq 1. \quad (8.157)$$

As noted in the discussion of equation (8.126) (see also Figure 8.3), this shape function arises from matching the function and its derivative to zero at the boundary layer base. This shape function removes problems with the spuriously large divergences across the boundary layer base since the non-local term smoothly goes to zero at $\sigma = 1$. Additionally, the shape function $G_{\text{universal}}(\sigma)$ has a maximum at $\sigma = 1/3$, where $G'_{\text{universal}}(\sigma) = 1 - 4\sigma + 3\sigma^2 = 0$. Hence, the maximum value for the product $G_{\text{universal}}(\sigma)C_s$ is

$$[G_{\text{universal}}(\sigma = 1/3)C_s]_{\text{maximum}} = \left(\frac{4}{27}\right) 6.33 \approx 0.94 < 1, \quad (8.158)$$

using $C_s = 6.33$ suggested by [Large et al. \(1994\)](#) (see equation (8.150)). Since $[G_{\text{universal}}(\sigma = 1/3)C_s]_{\text{maximum}} < 1$, the shape function $G_{\text{universal}}(\sigma)$ removes problems with the non-local flux being larger than the surface flux.

8.5.5.4 Resolution II: universal shape function

The recommended approach for CVMix is to employ the *same* shape function for the diffusivities as given by $G_{\text{universal}}(\sigma) = \sigma(1 - \sigma)^2$ in equation (8.157). In this way, the KPP diffusivity takes on the rather simple form for both the parameterized local flux and non-local flux

$$K_\lambda^{\text{KPP}} = K_\lambda = K_\lambda^{\text{non-local}} = h w_\lambda \sigma(1 - \sigma)^2. \quad (8.159)$$

If this approach is used, then diffusivities from processes such as tide mixing and shear mixing, which are not parameterized by the KPP boundary layer scheme, should be allowed to penetrate into the surface boundary layer. That is, the approach proposed for CVMix assumes the net diffusivity, even in the surface boundary layer, is the *sum* of the KPP diffusivity plus that from other processes

$$K_\lambda^{\text{net}} = K_\lambda^{\text{KPP}} + \sum K_\lambda^{\text{other processes}}, \quad (8.160)$$

where those other processes parameterized by the diffusivities $K_\lambda^{\text{other processes}}$ are spectrally localized away from the processes parameterized by KPP. Again, this approach is simpler than the original [Large et al. \(1994\)](#) approach, which incorporated the effects from interior mixing by matching boundary layer and interior diffusivities at the base of the boundary layer. That approach has serious problems in practice due to the reasons noted earlier. It also has no more fundamental physical basis than the summed diffusivities (8.160) proposed for CVMix.

In summary, the recommended parameterization of the local and non-local flux within the surface boundary layer via the KPP scheme is given by

$$\overline{w\lambda}^{\text{local}} = -K_\lambda \left(\frac{\partial \Lambda}{\partial z} \right) \quad (8.161a)$$

$$\overline{w\theta}^{\text{non-local}} = K_\theta \gamma_\theta = -\sigma(1 - \sigma)^2 C_s \left(\frac{Q^{\text{heat}}}{\rho_o C_p^o} \right) \quad (8.161b)$$

$$\overline{ws}^{\text{non-local}} = K_s \gamma_s = -\sigma(1 - \sigma)^2 C_s Q^s. \quad (8.161c)$$

Since the vertical velocity scale w_λ is the same for scalar species, such as temperature, salinity, and biogeochemical species, the KPP diffusivity is then the same for all tracers³

$$K^{\text{KPP}} = K_\theta = K_s. \quad (8.162)$$

The vertical viscosity arising from the KPP scheme generally differs from the KPP tracer diffusivity, since the turbulent velocity scale for momentum, w_m , differs from the tracer velocity scale, w_s (see Sections 8.5.1 and 8.5.2).

8.5.5.5 Further problems to be discussed later

In section 8.6 we identify further problems with the parameterized non-local term, even when using the shape function $\sigma(1 - \sigma)^2$. We thus revisit in that section the question about how to parameterize the non-local flux.

8.5.6 Penetrative shortwave and the KPP non-local redistribution

Equation (20) from Large et al. (1994) provides an expression for the non-local flux parameterized by KPP. Notably, the heat flux includes shortwave radiation. In this section, we discuss some of the issues related to the shortwave radiation and its contribution to the non-local term. We note that there is no guidance from the atmospheric application of KPP, since the atmosphere is largely transparent to shortwave. In contrast, the ocean transmits surface shortwave radiation only into a few 10s of metres of the upper ocean, with the transmittance a function of the optical properties of seawater.

The importance of penetrative shortwave radiation for upper ocean heating, particularly in the tropics, is well established (e.g., Sweeney et al. (2005), Manizza et al. (2005), Anderson et al. (2007), Anderson et al. (2009)). Additionally, upper ocean shortwave heating plays an important role in sea ice formation/melt in relatively fresh regions, such as the Baltic Sea, where the thermal expansion coefficient, α , is negative. In these regions, shortwave heating, particularly in the spring time, destabilizes the boundary layer (heating provides a negative buoyancy flux when $\alpha < 0$), with the associated vertical mixing of warmer sub-surface waters helping to melt the winter sea ice (Martin Schmidt, personal communication).

8.5.6.1 Physical ideas

Recognizing that the KPP non-local term acts as a redistribution of surface tracer fluxes, we are led to question whether the shortwave heat flux should be included as part of the KPP surface heat flux redistribution. One may argue that it should *not* be included, since it is already included as part of an optics-based penetration process (e.g., Manizza et al. (2005)), with this penetration dependent only on seawater optical properties. If we allow the surface shortwave radiation to also be redistributed with the non-local KPP process, then the net shortwave reaching beneath the surface can be larger than the shortwave radiative flux incident on the ocean surface. But is this wrong? And will it be problematic? These are two related, but distinct, questions that we aim to address here.

Consider a quiescent stably stratified ocean with uniform optical properties; e.g., there is uniform chlorophyll concentration. Shortwave radiation incident on the ocean surface will penetrate into the interior according to the ocean optics, given some exponential decay relations such as those from Manizza et al. (2005). Now allow the surface to have a strong cooling that is stronger than the shortwave warming, thus creating a negative buoyancy flux and leading to convective mixing processes. Assuming uniform optical properties both before and after the negative buoyancy flux means that the exponential shortwave penetration remains unchanged. However, the shortwave absorbed in the surface layer ($\sigma < \epsilon h$) will be carried into the deeper reaches of the boundary layer through the action of the turbulence. Consequently, there will be more shortwave reaching the deeper portion of the boundary layer than just through the optical penetration alone.

³The net tracer diffusivity within the surface boundary layer may be a function of the tracer, but tracer dependence arises only from processes that are not parameterized by the KPP scheme (see equation (8.160)).

We are thus motivated to include the shortwave radiation as part of the surface buoyancy flux appearing in the non-local flux. Now the presence of shortwave radiation (i.e., daytime) in the presence of negative buoyancy forcing typically occurs in the high latitudes, where strong sensible and latent heating can overcome shortwave radiation even during the daytime. In these regions, most of the shortwave radiation is absorbed within the upper portion of the boundary layers. So it is common to merely include the full incident shortwave as part of the heat flux determining the parameterized non-local flux.

8.5.6.2 Some mathematics

A redistribution process vertically redistributes heat over a fluid column, and so does not generate or destroy the net heat entering through the ocean surface. This redistribution is presumably unphysical if somehow the process produces an interior heat flux that is larger than the boundary heat flux. This situation can occur if the KPP non-local term *plus* a penetrative optical scheme separately act to vertically redistribute the shortwave radiation in a fluid column. We illustrate this situation here.

For this purpose, return to the heat equation for a surface model grid cell (8.32). Now, consider only those contributions from surface heating and non-local KPP flux

$$\frac{\partial(\rho dz \Theta)}{\partial t} = \underbrace{Q_{\theta}^{\text{non-pen}}(z = \eta) + Q_{\theta}^{\text{pen}}(z = \eta)}_{\text{penetrative + non-penetrative surface flux}} - \underbrace{\left(Q_{\theta}^{\text{pen}} - \overline{w \theta}^{\text{non-local}}\right)_{z=-\Delta z}}_{\text{heat flux leaving through cell bottom}}. \quad (8.163)$$

Recall that $\overline{w \theta}^{\text{non-local}}(z = \eta) = 0$, and so the non-local term contributes to the surface cell only through the bottom of the surface grid cell. Now write the non-local term in the simplified form (8.161b) to render

$$\frac{\partial(\rho dz \Theta)}{\partial t} = Q_{\theta}^{\text{non-pen}}(z = \eta) \left(1 - C_s \sigma (1 - \sigma)^2\right) + Q_{\theta}^{\text{pen}}(z = \eta) - \left(Q_{\theta}^{\text{pen}}(z = \eta) C_s \sigma (1 - \sigma)^2 + Q_{\theta}^{\text{pen}}(z = -\Delta z)\right). \quad (8.164)$$

where $\sigma = \Delta z/h$ is the dimensionless depth within the boundary layer. The first term on the right hand side provides a vertical redistribution of the non-penetrative heat fluxes (i.e., sensible, longwave, latent) through the KPP boundary layer. Its form highlights the discussion in Section 8.5.5.1, in which we pointed out that that the non-locally redistributed surface flux must itself be less than the net surface flux entering the ocean surface. Otherwise, the redistributed heat flux leaving the bottom of the surface cell will have a magnitude larger than that entering the top.

The second term in equation (8.164) arises from the shortwave radiation incident on the ocean surface. The final term is the combined effect of redistribution of the shortwave radiation from KPP plus the shortwave that penetrates through the bottom of the cell as determined by seawater optical properties. We now see that if

$$Q_{\theta}^{\text{pen}}(z = \eta) < Q_{\theta}^{\text{pen}}(z = -\Delta z) + Q_{\theta}^{\text{pen}}(z = \eta) C_s \sigma (1 - \sigma)^2 \quad (8.165)$$

then the shortwave incident on the ocean surface is *less* than that which leaves the bottom of the grid cell. That is, the redistributed surface incident shortwave can be larger than the incident shortwave. This situation is exacerbated in situations where the seawater is relatively clear, or where the boundary layer is relatively shallow.

But is it unphysical to have more shortwave leave the bottom of a cell than entered the top? It is, if we are referring to the same shortwave (i.e., the same photons). But we can have more leaving the bottom if there is an absorption of some shortwave that is then transported to depth via the turbulence, as per the discussion in Section 8.5.6.1. Nonetheless, there can be problems in the transient situation, and we now discuss some possible remedies.

8.5.6.3 Modifying the treatment of shortwave in the KPP non-local flux

We consider two options to ameliorate the situation (8.165). First, we allow the KPP scheme to redistribute *only* that shortwave radiation local to the depth of the non-local term, in which case the heat equation (8.164) takes the form

$$\frac{\partial(\rho dz \Theta)}{\partial t} = Q_{\theta}^{\text{non-pen}}(z = \eta) \left(1 - C_s \sigma (1 - \sigma)^2\right) + Q_{\theta}^{\text{pen}}(z = \eta) - Q_{\theta}^{\text{pen}}(z = -\Delta z) \left(1 + C_s \sigma (1 - \sigma)^2\right). \quad (8.166)$$

Excessive heating now occurs only for those cases where

$$Q_{\theta}^{\text{pen}}(z = \eta) < Q_{\theta}^{\text{pen}}(z = -\Delta z) (1 + C_s \sigma (1 - \sigma)^2). \quad (8.167)$$

The second modification completely removes the shortwave heat flux from the KPP non-local redistribution. In this case, the heat equation (8.166) takes the form

$$\frac{\partial(\rho dz \Theta)}{\partial t} = Q_{\theta}^{\text{non-pen}}(z = \eta) (1 - C_s \sigma (1 - \sigma)^2) + (Q_{\theta}^{\text{pen}}(z = \eta) - Q_{\theta}^{\text{pen}}(z = -\Delta z)). \quad (8.168)$$

In this way, the non-local redistribution from KPP only acts on the non-penetrative surface heat flux, whereas the shortwave flux is redistributed only through the penetrative optical scheme. This approach is counter to the idea that some of the absorbed shortwave indeed is carried by the turbulent eddies.

8.5.7 Bulk Richardson number and the OBL thickness

Large et al. (1994) define the KPP boundary layer depth to be an interpolation to the depth at which the bulk Richardson number, Ri_b , equals to a critical Richardson number,

$$Ri_c = \text{critical bulk Richardson number}. \quad (8.169)$$

Smaller values for Ri_b , including negative values, signal that we are still in the boundary layer, whereas larger values are beneath. The critical value Ri_c sets a threshold for upper ocean mixing, with such enabling behaviour that is sensitive to its precise value.

The bulk Richardson number is a non-local version of the gradient Richardson number defined in Section 2.3. It aims to measure the ability of an upper ocean eddy, with buoyancy set by values of temperature and salinity in the surface layer (Figure 8.1), to move downward in the water column, overcoming the resistance from stratification and aided by both resolved and unresolved vertical shear. Presumably at some point, such boundary layer eddies will be suppressed by the reduced shear and increased buoyancy stratification present below the boundary layer.

Using the notation from Large et al. (1994), we may write the bulk Richardson number at a distance d from the ocean surface in the form

$$Ri_b(d) = \frac{d[B_r - B(d)]}{|\mathbf{U}_r - \mathbf{U}(d)|^2 + U_t^2}. \quad (8.170)$$

This calculation makes use of the surface layer averaged buoyancy, B_r , and surface layer averaged horizontal velocity, \mathbf{U}_r , where the surface layer is defined by $0 \leq \sigma \leq \epsilon$ (Figure 8.1). The term U_t^2 is associated with parameterized unresolved vertical shears that may act to further reduce the bulk Richardson number.

Using notation introduced in the local gravitational stability calculation from Section 2.2, we write the bulk Richardson number in the form

$$Ri_b(d) = \left(\frac{dg}{\rho_o} \right) \left(\frac{\rho[\Theta(d), S(d), p(d)] - \rho[\Theta_r, S_r, p(d)]}{|\mathbf{U}_r - \mathbf{U}(d)|^2 + U_t^2} \right). \quad (8.171)$$

The density $\rho[\Theta(d), S(d), p(d)]$ is the *in situ* value at a distance d from the surface. The density $\rho[\Theta_r, S_r, p(d)]$ is based on an adiabatic and isohaline displacement from the surface layer to the depth d . Now consider three cases to expose the physics of the bulk Richardson number.

- **SURFACE EDDY HAS NEGATIVE RELATIVE BUOYANCY:** If the density $\rho[\Theta_r, S_r, p(d)]$ is greater than the *in situ* density, $\rho[\Theta(d), S(d), p(d)]$, then a surface layer parcel can move downwards and the boundary layer base has yet to be reached. That is, the surface layer parcel has negative buoyancy relative to the ambient fluid. This situation leads to a negative bulk Richardson number, in which case the criteria $Ri_b(d) > Ri_c$ has not yet been reached.
- **SURFACE EDDY HAS POSITIVE RELATIVE BUOYANCY AND AMBIENT FLUID HAS STRONG SHEARS:** If the density $\rho[\Theta_r, S_r, p(d)]$ is less than the *in situ* density, $\rho[\Theta(d), S(d), p(d)]$, a surface layer eddy has positive buoyancy relative to the ambient fluid. However, if the vertical shear is large, then the bulk Richardson number can still be less than the critical value, in which case mechanically induced mixing is still large and the boundary layer base has yet to be reached.

- SURFACE EDDY HAS POSITIVE RELATIVE BUOYANCY AND AMBIENT FLUID HAS WEAK SHEARS: Finally, if a surface eddy has positive relative buoyancy and the ambient fluid has weak shears, then at some point the bulk Richardson number will become larger than the critical value. Interpolating to where that cross-over occurs determines the boundary layer thickness h .

8.5.7.1 Averaging properties over the surface layer

As mentioned above, it is necessary to determine the averaged temperature, salinity, and velocity within the surface layer $0 \leq d \leq \epsilon h$ in order to compute the bulk Richardson number (8.171). The surface layer will generally penetrate many grid cells in the vertical where the boundary deepens due to negative buoyancy forcing and/or in models with refined vertical grid spacing. In order to reduce sensitivity to vertical grid spacing, it is necessary to average properties over the surface layer prior to computing the bulk Richardson number.

However, the bulk Richardson number (equation (8.171)) is itself needed to compute the boundary layer depth h . So we have a circular situation in which to compute Ri_b we need the boundary layer depth h , but to compute h we need Ri_b . We can resolve this circularity by considering an iterative process. There are additional subtleties when averaging temperature and salinity over the surface layer. Each of these considerations must be handled by the model calling CVMix, since the density difference $\rho[\Theta(d), S(d), p(d)] - \rho[\Theta_r, S_r, p(d)]$ and velocity difference $|\mathbf{U}_r - \mathbf{U}(d)|$ are inputs to the CVMix scheme. We outline here the method used for the MOM6 implementation of CVMix.

On the initial iteration, we assume a boundary layer depth, $h^{(0)}$, (e.g., $h^{(0)} = 100$ m) and compute the surface layer averaged tracer and velocity according to the expression

$$\Phi_r^{(0)}(d) = \frac{1}{\min(\epsilon h^{(0)}, d)} \int_{-\min(\epsilon h^{(0)}, d)}^0 \Phi(z) dz. \quad (8.172)$$

For depths beneath the surface layer, $d > \epsilon h^{(0)}$, the surface averaged properties are computed over the full extent of the region from the ocean surface down to the base of the first guess surface layer at $d = \epsilon h^{(0)}$. However, for grid points shallower than the surface layer base, $d < \epsilon h^{(0)}$, the “surface” averaged properties are computed as an average just down to the grid point depth d (i.e., just over the region $0 < d$). That is, we omit points in the region deeper than d yet still within the surface layer. This approach ensures that for the Richardson number calculation at grid points within the surface layer, we are not spuriously stabilizing or destabilizing these points, which could occur if computing an average that includes deeper points within the surface layer.

After determining the initial surface averaged properties $\Phi_r^{(0)}$, using an initial guess for $h^{(0)}$, then the bulk Richardson number is used to determine the first nontrivial estimate of the boundary layer depth, $h^{(1)}$. The boundary layer depth $h^{(1)}$ then replaces $h^{(0)}$ for use in an updated calculation of the surface averaged properties, $\Phi_r^{(1)}$, then allowing calculation of a new bulk Richardson number, and finally a new boundary layer depth $h^{(2)}$. We are presently testing the needs to further iterate beyond $h^{(2)}$.⁴

8.5.7.2 Non-local gravitational stability

Section 2.2 presents a general discussion of local gravitational stability. Much of that material is useful for the purpose of determining gravitational stability for parcels that are a finite distance from one another. However, there is one aspect of the discussion in Section 2.2 that differs from the present considerations. Namely, we are here always considering downward displacements of parcels from the surface layer. The reason is that we are concerned with parcels starting from the surface layer moving downwards in an adiabatic and isohaline manner, with resistance to such motion determined by the ambient stratification and shear. Figure 8.6 illustrates this situation. We are not interested in the complement movement of a deep parcel towards the surface.

⁴Need to summarize MOM6 practice here.

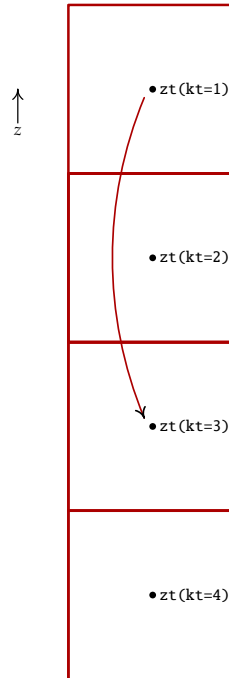


Figure 8.6: Schematic of the adiabatic and isohaline parcel displacement that is used to determine non-local gravitational stability for computing the bulk Richardson number according to equation (8.171). The reference temperature and salinity of this displaced parcel is set according to values determined in the surface layer, here approximated by the value at the top model grid cell with vertical position $z_t(kt=1)$. The density of this parcel is then computed using the surface layer temperature and salinity and the local *in situ* pressure. This displaced parcel's density is then compared to the ambient *in situ* density using the local temperature, salinity, and pressure. We illustrate that process by displacing the parcel to $z_t(kt=3)$. If the resulting bulk Richardson number is larger than the critical value, the base of the KPP boundary layer is at or shallower than $z_t(kt=3)$, with interpolation used to determine the KPP boundary layer thickness h . If the bulk Richardson number is less than the critical value, the boundary layer bottom has yet to be reached, so the downward search continues.

The expression (8.171) presents a direct means for computing the non-local gravitational stability via the computation of the density difference, written here using discrete notation from Figure 8.6

$$\delta\rho[kt, r] = \rho[\Theta(kt), S(kt), p(kt)] - \rho[\Theta_r, S_r, p(kt)], \quad (8.173)$$

where the surface layer values Θ_r, S_r are typically approximated by the values as $kt = 1$. This approximation breaks down for stable boundary layers with vertical grid spacing finer than roughly 2 m, in which case an averaging is required as in Section 8.5.7.1.

There is an alternative method to approximate $\delta\rho[kt, r]$ based on linear truncations of Taylor series expansions. The alternative leads to a sum of squared buoyancy frequencies, analogous to the expression (2.21). There are some advantages offered by the alternative approach, namely there are fewer calculations of the equation of state, assuming we already have the expansion coefficients α and β . However, the deeper the boundary layer, and the more nonlinear the equation of state, the less accurate the approximation becomes. We therefore recommend the more exact calculation based on the density differences in equation (8.173).

For completeness, we develop the alternative approach. For this purpose, consider a displacement from level $kt = 1$ to $kt > 1$, in which we need to compute $\rho[\Theta(kt = 1), S(kt = 1), p(kt > 1)]$. Truncating a Taylor

series at leading order yields

$$\rho[\Theta(1), S(1), p(kt > 1)] \approx \rho[\Theta(1), S(1), p(1)] - \sum_{n=1}^{kt} dz w(n+1) \left(\frac{\partial \rho}{\partial p} \frac{\partial p}{\partial z} \right)_{zt(n)}. \quad (8.174)$$

A similar expression for the *in situ* density $\rho[\Theta(kt), S(kt), p(kt)]$

$$\rho[\Theta(kt), S(kt), p(kt)] \approx \rho[\Theta(1), S(1), p(1)] - \sum_{n=1}^{kt} dz w(n+1) \left(\frac{\partial \rho}{\partial p} \frac{\partial p}{\partial z} + \frac{\partial \rho}{\partial \Theta} \frac{\partial \Theta}{\partial z} + \frac{\partial \rho}{\partial S} \frac{\partial S}{\partial z} \right)_{zt(n)}. \quad (8.175)$$

These results lead to the approximation

$$\delta \rho[kt, r] = \rho[\Theta(kt), S(kt), p(kt)] - \rho[\Theta_r, S_r, p(kt)] \quad (8.176a)$$

$$\approx - \sum_{n=1}^{kt} dz w(n+1) \left(\frac{\partial \rho}{\partial \Theta} \frac{\partial \Theta}{\partial z} + \frac{\partial \rho}{\partial S} \frac{\partial S}{\partial z} \right)_{zt(n)} \quad (8.176b)$$

$$= \sum_{n=1}^{kt} dz w(n+1) \left(\rho \alpha \frac{\partial \Theta}{\partial z} - \rho \beta \frac{\partial S}{\partial z} \right)_{zt(n)} \quad (8.176c)$$

$$= \frac{1}{g} \sum_{n=1}^{kt} dz w(n+1) (\rho N^2)_{zt(n)}. \quad (8.176d)$$

Again, this result is analogous to the approximate forms given in Section 2.2.3 for the local calculation of gravitational stability. However, for both the local and non-local calculation of stability, we recommend the more exact approach that does not perform a truncation, particularly in regions of deep mixing in the high latitudes. Making the approximation may also compromise the ability of the KPP scheme to include thermobaric convection. We are thus reticent to recommend this approach, and instead prefer the original approach given by equation (8.171).

8.5.7.3 Unresolved velocity scale U_t used for Ri_b

The shear, U_t/d , in the bulk Richardson number (8.171) acknowledges the potential for unresolved to impact on the boundary layer depth. The unresolved shear acts to deepen the boundary layer beyond that which would occur with only the resolved shears. Large et al. (1994) present an argument on their page 372 that focuses on an unresolved shear that reduces to a desired form for the case of pure convection. The general result is for the velocity scale U_t given by

$$U_t^2(d) = d \left(\frac{C_v (-\beta_T)^{1/2}}{Ri_c \kappa^2} \right) (c_s \epsilon)^{-1/2} N w_s \quad (8.177a)$$

$$= (d C_v N w_s) \left(\frac{\sqrt{-\beta_T / (c_s \epsilon)}}{Ri_c \kappa^2} \right). \quad (8.177b)$$

We now summarize the terms appearing in this expression.

- The von Karman constant $\kappa \approx 0.40$ is chosen according to equation (8.77).
- The constant C_v sets the buoyancy frequency at the entrainment depth, and its value is expected to be

$$1 < C_v < 2. \quad (8.178)$$

Appendix A of Danabasoglu et al. (2006) provides the specific suggestion of

$$C_v = \begin{cases} 2.1 - 200 \max(0, N) & N \leq 0.002 \text{ sec}^{-1} \\ 1.7 & \text{otherwise.} \end{cases} \quad (8.179)$$

- The constant c_s is part of the similarity function for scalar fields discussed in Section 8.4.3. It has a value $c_s = 98.96$ according to equation (8.116b).
- The constant β_T is discussed in the caption to Figure 8.2, and it is the ratio of the buoyancy flux at the entrainment depth, h_e , to the buoyancy flux at the surface,

$$\overline{wb}^{d=h_e} = \beta_T \overline{wb}^0, \quad (8.180)$$

with

$$\beta_T \approx -0.2 \quad (8.181)$$

an empirical result.

- The critical Richardson number, Ri_c , is used to determine when the boundary layer base is reached, in which case stratification and/or reduced shear lead to a bulk Richardson number larger than the critical value. Large et al. (1994) choose the value

$$Ri_c = 0.3. \quad (8.182)$$

- The dimensionless number ϵ determines the thickness of the surface layer as in Figure 8.1, with

$$\epsilon = 0.1 \quad (8.183)$$

chosen by Large et al. (1994).

- The MOM5 code takes the buoyancy frequency N appearing in equations (8.177b) and (8.179) to be the absolute value of the frequency

$$N = |N|. \quad (8.184)$$

However, this choice is problematic in regions of unstable buoyancy forcing, where $N^2 < 0$ is common. So instead, one should take

$$N = \max(0, N), \quad (8.185)$$

which is how this approach was implemented in POP.

- It is notable that there are no surface gravity wave parameters in the specification of the unresolved shear. We have more to say on this topic in Section 8.7.

8.5.7.4 An algorithm to specify the unresolved velocity scale U_t

The unresolved velocity scale U_t (equation (8.177b)) is needed for the bulk Richardson number in equation (8.170), with the bulk Richardson number used to compute the boundary layer depth, h . Now the unresolved velocity U_t requires the scalar turbulent velocity scale w_s (Section 8.5.1). Yet the scalar velocity scale w_s in turn requires the boundary layer depth h since w_s is a function of the dimensionless boundary layer depth $\sigma = d/h$ (equation (8.17)).

One method to resolve the above circular argument is to iterate. Another means, employed by the KPP code in POP and MOM, is based on the following observation. Namely, to compute the boundary layer depth h we determine the depth below which the bulk Richardson number is larger than the critical Richardson number (equation (8.169)). In determining that depth, we proceed as follows for each horizontal grid point.

- For a grid level k , assume the boundary layer depth, h , equals to the depth of a tracer grid point, d , in which case $\sigma = 1$ and $h = d$.
- Compute the turbulent velocity scale for scalars, w_s , as a function of the buoyancy forcing and wind forcing (Section 8.5.1).
- Compute the unresolved velocity scale U_t (equation (8.177b)).
- Compute the bulk Richardson number Ri_b (equation (8.170)).

- If $Ri_b < Ri_c$, then we are still within the surface boundary layer, in which case the algorithm proceeds downward by one grid cell.
- If $Ri_b \geq Ri_c$, then we have penetrated below the boundary layer, in which case the algorithm interpolates to determine the actual boundary layer depth h .
- Once the boundary layer depth is known, we compute the turbulent velocity scale w_λ , which is used to compute the KPP boundary layer diffusivity according to equation (8.90).

8.5.7.5 Minimum value for the unresolved velocity scale U_t

In the testing of the CVMix implementation of KPP in MOM6, we considered a trivial one-dimensional situation of neutral forcing ($B_f = 0$) and initially uniform temperature and salinity. We also maintained a zero resolved velocity through use of periodic lateral boundary conditions. The initially uniform temperature and salinity means that the buoyancy frequency is zero, in which case the unresolved velocity (8.177b) vanishes. The numerator and denominator of the bulk Richardson number thus vanish on the first time step. To remove the computational singularity associated with $0/0$, we add a small positive number to the denominator, in effect placing a minimum on the unresolved squared velocity U_t^2 . This approach follows *Alistair Adcroft's Theorem*, in which division by zero in an ocean model should be replaced by zero. The trivial test then proceeds with nothing happening, regardless the wind stress, which is physically what should occur given that the buoyancy forcing vanishes and the temperature and salinity are uniform.

Now impose a positive buoyancy forcing to the above test, again with nonzero wind acting on a uniform initial condition for temperature and salinity. If strong enough, mechanical energy from the winds mixes the positive buoyancy into the ocean over a nonzero boundary layer region, with the boundary layer deepening as long as the mechanical mixing is maintained. However, in some one-dimensional tests, this physical expectation was found to be sensitive to computational roundoff in the calculation of the buoyancy frequency. The resulting boundary layer depth in turn asymptoted to a fixed value that never deepened and was independent of the wind stress. The upper ocean buoyancy thus increased without bound.

The spurious behaviour in this test is removed by enabling a sufficiently large unresolved velocity U_t^2 to overcome computational roundoff in the calculation of N . Using double precision for the computations, we have found

$$\left(U_t^2\right)_{\text{minimum}} \approx 10^{-11} \text{ m}^2 \text{ s}^{-2} \quad (8.186)$$

is sufficient to recover physically consistent behaviour for this particular test case. With a nontrivial denominator, the bulk Richardson number is small in the upper ocean but large below the boundary layer, allowing for enhanced mixing to move the positive buoyancy into the interior, further deepening the boundary layer as the simulation proceeds.

8.5.7.6 Restrictions on h under stable buoyancy forcing

Large et al. (1994) suggest (see their page 372) that for stable buoyancy forcing, $B_f > 0$, the boundary layer thickness, h , should be no larger than either the Monin-Obukhov length scale, L , or the Ekman length scale,

$$h_E = 0.7 u_* / |f|, \quad (8.187)$$

with f the Coriolis parameter. The following reasons are noted to motivate these two restrictions.

- **MONIN-ОБУКHOV:** At depths deeper than L , buoyancy stratification suppresses the mechanically forced turbulence, thus cutting off the boundary layer.
- **EKMAN:** The Ekman depth is the extent of the boundary layer in neutral stratification ($N^2 = 0$). With stable buoyancy forcing, $B_f > 0$, we then expect the boundary layer depth to be less than the Ekman depth. Note that Large et al. (1994) do not mention the origin of the 0.7 factor in equation (8.187).

As noted in Large et al. (1994) and Large and Gent (1999), the restriction on boundary layer thickness based on the Monin-Obukhov length has been dropped in the NCAR implementation of KPP, as it does not lead to favorable effects. Dropping this constraint is also supported by the results from Shchepetkin (2005)

and [Lemarié et al. \(2012\)](#). Likewise, the constraint based on the Ekman depth is not used at NCAR, as little sensitivity was seen with its use. Hence, there are no restrictions for the maximum boundary layer depth under stable forcing imposed by the NCAR implementation of KPP. Such is the standard approach used in the CVMix implementation.

The key problem with the Monin-Obukhov length scale, L , relates to the question of how to include penetrative shortwave heating in the calculation of the buoyancy forcing, B_f (Section 8.3.10). Depending on the depth over which the penetrative heating is included (equation (8.64)), one can produce a positive Monin-Obukhov length (if including sufficient shortwave heating) or negative (if including less heating). Since there is no fundamental reason to choose a particular amount of the shortwave when considering the total buoyancy forcing, there is no compelling reason to enforce the L constraint on boundary layer thickness.

8.5.7.7 Noise in the boundary layer thickness

Experience in MOM, POP, and ROMS indicate that the KPP boundary layer thickness, h , can become quite noisy. Noise in the boundary layer thickness can translate into noise in the tracer fields within the boundary layer. Hence, it is common practice to apply a horizontal smoothing operator, such as a Laplacian, to h prior to its use in computing the diffusivity or non-local transport.

The horizontal smoothing of h poses an algorithmic problem for CVMix, since CVMix modules ideally know nothing about the horizontal grid. There are two possible options that may be considered.

- **INTERMEDIATE h SENT BACK TO CALLING MODEL:** One option is to compute h in CVMix; send it immediately back to the calling model for smoothing; then have the smoothed h used for further KPP computations such as the diffusivity and non-local term.
- **USE PREVIOUS h :** We compute the new value of h within a particular call to the CVMix-KPP module, and we send this unsmoothed h back to the calling model at the end of the CVMix-KPP module. But for computing the KPP diffusivities and non-local term within CVMix, we use the previous time step value h , with this earlier h having been smoothed by the calling model. This approach requires storing h in restart files, but that is easily handled by the calling model.

This issue remains under consideration and there is no consensus recommendation on a useful approach.

8.5.8 Surface boundary condition

The KPP parameterization as per [Large et al. \(1994\)](#) prescribe a vanishing non-local flux at the ocean surface, so that

$$\overline{w\lambda}^{\text{non-local}} = 0 \quad \text{at } z = \eta. \quad (8.188)$$

Although standard in the KPP implementation for CVMix, we reconsider this boundary condition in Section 8.6 in order to remove a pathology. For now, we note that this boundary condition is satisfied by ensuring that the non-dimensional vertical shape function $G_\lambda(\sigma)$ vanishes at $\sigma = 0$. Since the same shape function is used for the parameterized non-local flux as for the diffusivity, we have

$$K_\lambda = 0 \quad \text{at } z = \eta. \quad (8.189)$$

We thus also set the local closure portion of the flux to zero at the surface

$$\overline{w\lambda}^{\text{local}} = -K_\lambda \left(\frac{\partial \Lambda}{\partial z} \right) = 0 \quad \text{at } z = \eta, \quad (8.190)$$

To incorporate the non-advective surface boundary fluxes (e.g., shortwave, longwave, latent, and sensible heat fluxes), we follow the usual convention in which these fluxes enter as a boundary condition on the vertical diffusion equation. In effect we have

$$\overline{w\lambda}^0 = Q^\lambda \quad \text{at } z = \eta. \quad (8.191)$$

This boundary condition will be revisited in Section 8.6.

8.5.9 Summary of the standard CVMix implementation of KPP

We summarize here the recommendations for those wishing to implement the KPP using the CVMix code. The main recommendation is to employ the universal shape function (equation (8.157)) rather than determine this function via the matching conditions used by [Large et al. \(1994\)](#). Nonetheless, the original approach is available with CVMix code, which allows one to systematically transition to the simpler approach.

- The recommended parameterization of the turbulent flux is given by

$$\overline{w\lambda} = -K_\lambda \left(\frac{\partial \lambda}{\partial z} \right) + K_\lambda \gamma_\lambda. \quad (8.192)$$

The diffusivity is written in the form

$$K_\lambda(\sigma) = h w_\lambda(\sigma) \sigma (1 - \sigma)^2, \quad (8.193)$$

where $\sigma = d/h$ is the non-dimensional boundary layer depth with d the depth, and h the boundary layer thickness. We also use the shape function

$$G(\sigma)_{\text{universal}} = \sigma (1 - \sigma)^2 \quad (8.194)$$

for both the local and non-local flux, and for all tracers and momentum.

- The vertical velocity scale, $w_\lambda(\sigma)$, is the same for each scalar tracer field, and distinct for the momentum only for regions of negative buoyancy flux $B_f < 0$. It is proportional to κu^* , where $\kappa = 0.4$ is the von Karman constant and $u^* = \sqrt{|\tau|/\rho_o}$ is the friction velocity scale. The proportionality is determined by dimensionless similarity functions (Sections 8.4.3 and 8.5.2). These similarity functions are determined empirically according to analogs with the atmosphere as formulated within Monin-Obukov similarity theory. This aspect of the KPP scheme as applied to the ocean is perhaps the least satisfying, since our ability to directly use atmospheric similarity functions for the ocean has not been tested with measurements.
- The boundary layer depth, h , is determined by a bulk Richardson number criteria (Section 8.5.7), whereby the first depth where $Ri_b > Ri_c$ determines the boundary layer depth. There are subtle issues related to the computation of the bulk Richardson number, with details provided in Section 8.5.7.
- The non-local flux $K_\lambda \gamma_\lambda$ vanishes for a positive surface buoyancy flux $B_f > 0$ and for momentum. For a negative surface buoyancy flux, $K_\lambda \gamma_\lambda$ provides for a vertical redistribution of surface tracer fluxes, so that

$$\overline{w\theta}^{\text{non-local}} = K_\theta \gamma_\theta = -\sigma (1 - \sigma)^2 C_s \left(\frac{Q^{\text{heat}}}{\rho_o C_p^o} \right) \quad (8.195a)$$

$$\overline{ws}^{\text{non-local}} = K_s \gamma_s = -\sigma (1 - \sigma)^2 C_s Q^s. \quad (8.195b)$$

The non-dimensional constant C_s is determined according to the similarity function for scalars, as well as other non-dimensional coefficients (see equation (8.141)).

8.6 Further considerations for the KPP non-local term

During the testing of KPP in CVMix, we encountered some cases where unphysical behaviour resulted. Some of these cases were summarized earlier, such as when motivating use of the universal shape function $G(\sigma)$ in Section 8.5.3. We raise further issues in this section, with particular focus on problems with the KPP non-local flux parameterization along with potential remedies.

8.6.1 KPP in the top grid cell

We start our discussion by considering what happens in the $k = 1$ surface model grid cell from the combined effects of surface boundary fluxes, KPP local downgradient diffusion, and KPP non-local redistribution of surface boundary fluxes. We do not identify a problem here. Instead, our purpose is to introduce the general behaviour that will be further explored later in this section.

- **CONVERGENCE INTO TOP CELL:** At the surface boundary, $z = \eta$, the parameterized local and non-local flux components vanish (Section 8.5.8). However, these flux components are nonzero at the bottom interface of the $k = 1$ cell, with larger fluxes for thicker top grid cells. Hence, there is a convergence of the KPP parameterized fluxes into the $k = 1$ cell.
- **LOCAL DOWNGRAIDENT DIFFUSION:** In a region stably stratified in temperature ($\partial\Theta/\partial z > 0$), the downgradient diffusive flux

$$\overline{w\theta}^{\text{local}} = -K_\theta \left(\frac{\partial\Theta}{\partial z} \right) < 0, \quad (8.196)$$

is negative at the lower face of the $k = 1$ cell. With the no-flux boundary condition (8.190) at the ocean surface, the parameterized local diffusive flux will cool the top model grid cell. For $k > 1$ interior cells, the diffusive flux either cools or warms, depending on curvature in the temperature field.

- **NON-LOCAL REDISTRIBUTION OF SURFACE BOUNDARY FLUX:** The KPP parameterized non-local tracer flux is non-zero only for cases of negative buoyancy forcing. Assuming such forcing occurs with a negative (cooling) surface heat flux, we already showed in Section 8.5.8 that $\gamma_\theta > 0$ for cooling (equation (8.153)). With the no-flux surface boundary condition (8.188), we thus have a positive convergence of heat into the $k = 1$ cell due to the KPP parameterized non-local flux. Hence, the KPP non-local fluxes heat the $k = 1$ cells whereas the parameterized downgradient diffusive fluxes cool this cell.

8.6.2 Tracer evolution with the KPP parameterization

We next consider effects from KPP throughout the boundary layer. For this purpose, return to the vertical transport equation (8.8) and focus on the KPP parameterized vertical processes as per the recommendations in Section 8.5.9. In the presence of negative buoyancy forcing we include the non-local KPP redistribution function, so that evolution of an arbitrary scalar tracer (ignoring horizontal processes) is determined by

$$\frac{\partial S}{\partial t} = - \left(\frac{\partial(\overline{ws})}{\partial z} \right) + Q^s \delta(z - \eta) \quad (8.197a)$$

$$= - \left(\frac{\partial(\overline{ws}^{\text{local}})}{\partial z} \right) - \left(\frac{\partial(\overline{ws}^{\text{non-local}})}{\partial z} \right) + Q^s \delta(z - \eta), \quad (8.197b)$$

$$= \frac{\partial}{\partial z} \left(K \frac{\partial S}{\partial z} \right) + C_s Q^s \frac{\partial}{\partial z} [\sigma (1 - \sigma)^2] + Q^s \delta(z - \eta) \quad (8.197c)$$

$$= \underbrace{\frac{\partial}{\partial z} \left(K \frac{\partial S}{\partial z} \right)}_{\text{local downgradient diffusion}} - \underbrace{\left(\frac{C_s Q^s}{h} \right) (1 - 3\sigma)(1 - \sigma)}_{\text{non-local redistribution of surface flux}} + \underbrace{Q^s \delta(z - \eta)}_{\text{surface boundary forcing}} \quad (8.197d)$$

where Q^s is the surface tracer flux ($Q^s > 0$ means tracer enters the ocean),

$$K = h w \sigma (1 - \sigma)^2 \geq 0 \quad (8.198)$$

is the KPP diffusivity, and we used $\sigma = (-z + \eta)/h$ so that

$$\frac{\partial \sigma}{\partial z} = -1/h. \quad (8.199)$$

The surface boundary flux is multiplied by a Dirac delta function (dimensions of inverse length), where

$$\int_{z=-h}^{z=\eta} \delta(z - \eta) dz = 1, \quad (8.200)$$

so that the flux appears as a surface boundary condition when integrating the tracer budget over the surface grid cell.

To help interpret the result (8.197d), we plot the KPP structure function $G = \sigma(1 - \sigma)^2$ as well as its derivative $G'(\sigma) = (1 - 3\sigma)(1 - \sigma)$ in Figure 8.7, from which we deduce the following behaviours.

- **DOWNGRADIENT DIFFUSION:** The local downgradient diffusive portion of the KPP parameterization always acts to smooth the profile of a tracer, given that the diffusivity is non-negative. The vertical diffusivity is zero at the ocean surface, $\sigma = 0$, and vanishes again at the boundary layer base, $\sigma = 1$. It is modulated by the non-dimensional shape function $G(\sigma) = \sigma(1 - \sigma)^2$, which has a maximum at $\sigma = 1/3$ (Figure 8.7). In the presence of a surface boundary flux, vertical diffusion transports the surface flux into the ocean interior on a time scale set by the vertical diffusivity K and curvature in the tracer field.
- **NON-LOCAL REDISTRIBUTION:** The non-local portion of the KPP parameterization redistributes the surface flux throughout the boundary layer. Its vertical structure is provided exclusively by the non-dimensional shape function $G(\sigma)$. There is no time scale for impacts from the non-local redistribution to affect a point within the boundary layer. Instead, the impacts are instantaneous. In the upper portion of the boundary layer, where $\sigma < 1/3$, the tracer tendency has a contribution that is opposite in sign to the surface boundary flux. It is furthermore in this shallow region where the non-local parameterization has its largest contribution at a single grid point (Figure 8.7). In contrast, for deeper reaches of the boundary layer with $\sigma > 1/3$, the tracer tendency has a contribution that has the same sign as the surface flux.

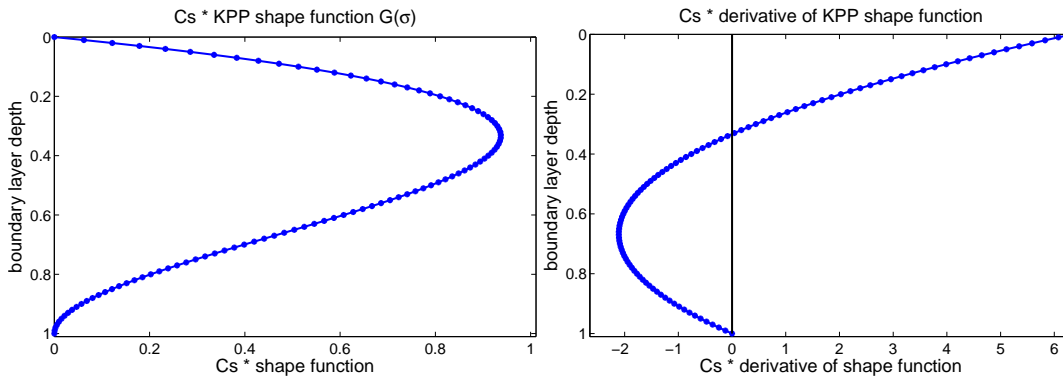


Figure 8.7: KPP shape function $G = \sigma(1 - \sigma)^2$ multiplied by the constant $C_s = 6.33$ (equation (8.150)) as well as its derivative $C_s G'(\sigma) = C_s(1 - 3\sigma)(1 - \sigma)$. In the upper portion of the boundary layer where $\sigma < 1/3$, the derivative is positive, in which case the non-local contribution to KPP adds a tendency to tracers with a sign opposite to that of the surface boundary flux (see equation (8.197d)). In the regions where $1/3 < \sigma < 1$, the KPP non-local tendency has the same sign as the surface boundary flux. The largest magnitude of $G'(\sigma)$ is at $\sigma = 0$, so that the largest impact at a single depth from the non-local flux convergence is in the upper portion of the boundary layer. The area encompassed by $G'(\sigma)$ in the shallow region $\sigma < 1/3$ is the same as that in the deeper region $1/3 < \sigma < 1$.

8.6.3 A thought experiment with surface cooling

We introduce a thought experiment to illustrate the potential for unphysical behaviour from the KPP parameterization, in particular from the parameterization of non-local transport of surface fluxes into the boundary layer. Consider constant surface cooling from sensible heat applied to an ocean that is stratified in salinity but unstratified in temperature, and ignore the impacts from penetrative shortwave radiation. There is no baroclinicity and surface forcing introduces no resolved vertical shear. Furthermore, assume zero surface water fluxes. Surface cooling thus imparts a negative buoyancy forcing, which means the KPP non-local redistribution function is active. Surface winds blow, but they are not fundamental to our considerations.

The tracer equation (8.197d) for temperature takes the form

$$\frac{\partial \Theta}{\partial t} = \frac{\partial}{\partial z} \left(K \frac{\partial \Theta}{\partial z} \right) - |Q_\theta| \left(\delta(z - \eta) - \frac{C_s}{h} (1 - 3\sigma)(1 - \sigma) \right). \quad (8.201)$$

Here are the basics of the temperature evolution.

- Boundary layer mixing penetrates to a depth determined initially by the salinity stratification, but over time the developing temperature structure also impacts on the boundary layer depth.
- The local portion of KPP diffusively spreads the surface cooling, $Q_\theta < 0$, into the ocean boundary layer as the boundary layer deepens.
- The KPP non-local redistribution warms the shallow regions of the boundary layer where $\sigma < 1/3$. Consequently, the KPP non-local flux partially counteracts cooling from the downgradient diffusion. Conversely, in the deeper portion of the boundary layer, where $\sigma > 1/3$, the non-local KPP flux enhances cooling. For the full boundary layer, the KPP non-local flux acts to restratify. Indeed, in cases where the non-local term dominates over the local diffusion, these stabilizing effects can reduce, rather than increase, the boundary layer depth. Conversely, for weakly stratified regions below the boundary layer, the introduction of cooling to the deeper boundary layer can destabilize the lower portion of the boundary layer, thus deepening the boundary layer.

As noted above, the KPP non-local term acts to increase the temperature in the shallow portion of the boundary layer where $0 < \sigma < 1/3$ (Figure 8.7). We further explore this process by considering the boundary layer at an early time in the simulation prior to local effects from downgradient diffusion having reached the depth considered, so that $\partial \Theta / \partial z = 0$. Even though diffusion has yet to reach this depth, the instantaneous effects from convergence of the KPP non-local flux acts to warm depths with $\sigma < 1/3$. We thus have ocean warming in the presence of surface cooling. As the simulation evolves, vertical diffusion spreads effects from surface cooling deeper into the boundary layer, and this cooling can overcome the warming effects from the non-local flux. We thus tend to see the warming from the KPP non-local flux early during a transient response to surface cooling.

This thought experiment has been realized in various idealized configurations of the KPP scheme using the CVMix code. We illustrate a particular case in Figure 8.8, with the figure caption providing experimental details. As seen in this figure, the warming manifests more prominently upon refining the vertical grid spacing. Doing so provides more grid points within the upper portion of the boundary layer, where the vertical diffusion effects are dominated by the non-local term. With a coarse enough vertical grid, evidence of spurious warming disappears.

In addition to noting problems with warming depths in the presence of surface cooling, it is trivial to illustrate problems in the case of an initially uniform passive tracer with a nonzero surface flux that adds tracer to the ocean. A negative passive tracer concentration arises during the early portion of the simulation, again due to the convergence of the KPP non-local flux in the region $\sigma < 1/3$.

In realistic configurations, time evolution of scalar fields may be dominated by effects such as advection and lateral mixing in a way that hides unphysical behaviour from the non-local KPP parameterization. Furthermore, the unphysical effects identified here occur in transient situations. Studies such as [Large et al. \(1994\)](#) focused instead on the steady state. Our results motivate investigating alternatives to the shape function used for the parameterized non-local flux, particularly in order to properly represent the transient behaviour.

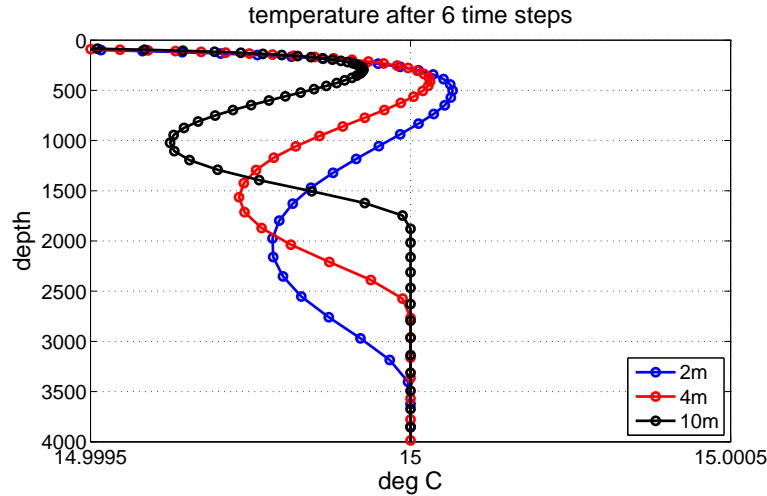


Figure 8.8: Temperature profiles after six time steps (each of one hour) for three different model grids from an idealized one-dimensional simulation. Each grid has 75 levels down to 6000 m (upper 4000 m shown here), with the upper ocean spacing noted in the figure. The simulation is forced with -100 W m^{-2} sensible heat flux, and no penetrative radiation. The temperature profile is initially uniform at 15°C , whereas the salinity profile is stable with the surface value of 35 and bottom value of 35.01. The equation of state is linear, with $\rho = \rho_o (1 - \alpha \Theta + \beta S)$, where $\alpha = 2.55 \times 10^{-4} \text{ }^\circ\text{C}^{-1}$, and $\beta = 7.4 \times 10^{-4} \text{ ppt}^{-1}$. Winds are applied with a stress of 0.1 N m^{-2} . The domain is periodic and there are no horizontal gradients, so that no resolved shear contributes to the bulk Richardson number calculation. Regions with temperatures larger than the initial uniform 15°C are unphysical, since they appear even though the surface is being cooled. Spurious warming is more prominent in the fine resolution simulation (2 m), whereas the coarse spaced grid (10 m) shows no sign of spurious warming due to the relatively larger contribution from vertical diffusion.

8.6.4 Modified shape function for the KPP non-local flux

In so far as properly representing the transient behaviour to a negative surface buoyancy flux, we identify the following two problems with the KPP non-local redistribution as parameterized by the shape function $G(\sigma) = \sigma(1 - \sigma)^2$.

- It redistributes a surface flux into the shallow boundary layer region ($\sigma < 1/3$) with an opposite sign to the surface flux itself.
- It affects the boundary layer instantaneously.

Unsatisfying elements from the instantaneous impacts become increasingly apparent when considering refined resolution models. Model time steps of a few minutes mean that the full extent of a boundary layer is impacted within minutes by changes in surface fluxes. This very short response time is reminiscent of the full convection parameterizations of the 1990s (e.g., [Rahmstorf \(1993\)](#)), which have largely been displaced by diffusive adjustment schemes that allow for a nonzero time scale (e.g., [Klinger et al. \(1996\)](#)). Nonetheless, within the framework of the KPP parameterization of non-local fluxes, we see no alternative to the instantaneous response.

However, we do see alternatives to the shape function used for the parameterized non-local flux. We denote this new function by $\mathcal{G}(\sigma)$ to distinguish it from $G(\sigma)$ used for the diffusivity. We emphasize that our considerations leave untouched the shape function for the diffusivity, which still takes the form $G(\sigma) = \sigma(1 - \sigma)^2$. Contrary to the $G(\sigma)$ shape function, we insist that $\mathcal{G}(\sigma)$ be monotonic, thus eliminating the sign change that causes problems with use of $G(\sigma)$ for the parameterized non-local flux. We also wish to

maintain a shape function that vanishes at the bottom of the boundary layer, so that

$$\mathcal{G}(\sigma = 1) = 0. \quad (8.202)$$

Given this lower boundary condition, a nontrivial shape function must have a nonzero surface value. Having $\mathcal{G}(0) \neq 0$ is fundamentally distinct from the constraint $G(0) = 0$ imposed by [Large et al. \(1994\)](#). However, having a non-zero non-local flux at the ocean surface may in fact be physically appropriate. Namely, we consider the non-local flux to be a redistribution of the surface flux into the boundary layer. Consequently, we may choose to let the parameterized non-local flux equal to the surface boundary flux when approaching the ocean surface, $\sigma \rightarrow 0$. That is,

$$\overline{ws}^{\text{non-local}}(\sigma = 0) = -Q^s \quad (8.203a)$$

$$= -C_s \mathcal{G}(0) Q^s \quad (8.203b)$$

$$\Rightarrow \mathcal{G}(0) = C_s^{-1}, \quad (8.203c)$$

where the minus sign in the first equation arose from the sign convention whereby $\overline{ws}^{\text{non-local}} > 0$ implies tracer leaving the ocean, whereas $Q^s > 0$ signals tracer entering the ocean (see [Section 8.1.1](#)).

Given the above considerations, we have investigated the following three shape functions

$$C_s \mathcal{G}(\sigma) = 1 - \sigma \quad (8.204a)$$

$$C_s \mathcal{G}(\sigma) = (1 - \sigma)^2 \quad (8.204b)$$

$$C_s \mathcal{G}(\sigma) = 1 + (2\sigma - 3)\sigma^2. \quad (8.204c)$$

The linear function has a constant nonzero slope, whereas the parabolic and cubic functions satisfy $\mathcal{G}'(\sigma = 1) = 0$. In [Figure 8.9](#) we plot the three modified shape functions and their derivatives. The non-local flux is parameterized by (compare to equation [\(8.195b\)](#))

$$\overline{ws}^{\text{non-local}} = -C_s \mathcal{G} Q^s \quad (8.205)$$

and its vertical convergence, which determines the tracer tendency, takes the form

$$-\frac{\partial}{\partial z} (\overline{ws}^{\text{non-local}})_{\text{linear}} = \left(\frac{Q^s}{h} \right) \quad (8.206a)$$

$$-\frac{\partial}{\partial z} (\overline{ws}^{\text{non-local}})_{\text{parabolic}} = \left(\frac{2Q^s}{h} \right) (1 - \sigma) \quad (8.206b)$$

$$-\frac{\partial}{\partial z} (\overline{ws}^{\text{non-local}})_{\text{cubic}} = \left(\frac{6Q^s}{h} \right) \sigma (1 - \sigma). \quad (8.206c)$$

The resulting tracer tendency ([8.197d](#)) is given by

$$\left(\frac{\partial S}{\partial t} \right)_{\text{linear}} = \underbrace{\frac{\partial}{\partial z} \left(K \frac{\partial S}{\partial z} \right)}_{\text{local downgradient diffusion}} + \underbrace{\left(\frac{Q^s}{h} \right)}_{\text{non-local redistribution}} \quad (8.207a)$$

$$\left(\frac{\partial S}{\partial t} \right)_{\text{parabolic}} = \underbrace{\frac{\partial}{\partial z} \left(K \frac{\partial S}{\partial z} \right)}_{\text{local downgradient diffusion}} + \underbrace{\left(\frac{2Q^s}{h} \right) (1 - \sigma)}_{\text{non-local redistribution}} \quad (8.207b)$$

$$\left(\frac{\partial S}{\partial t} \right)_{\text{cubic}} = \underbrace{\frac{\partial}{\partial z} \left(K \frac{\partial S}{\partial z} \right)}_{\text{local downgradient diffusion}} + \underbrace{\left(\frac{6Q^s}{h} \right) \sigma (1 - \sigma)}_{\text{non-local redistribution}}, \quad (8.207c)$$

in which we see that the non-local redistribution retains the sign of the surface flux throughout the boundary layer where $0 \leq \sigma \leq 1$. Note that the delta-function distributed surface flux, present in the formulation

(8.197d), has been dropped from equations (8.207a)–(8.207c). The reason is that the surface boundary condition has been absorbed by the parameterized non-local flux. That is, the boundary condition (8.191) is now directly part of the parameterized flux. Nonetheless, the reformulation of the boundary condition for the parameterized non-local flux leads to no code changes, since the boundary flux is introduced to the ocean in the same manner regardless the shape function.

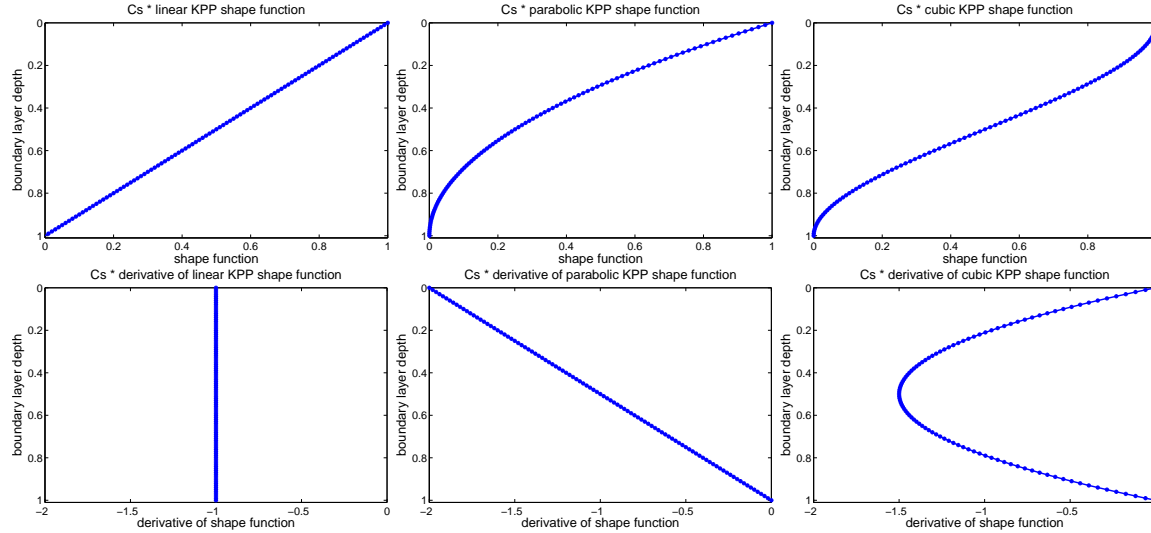


Figure 8.9: Modified KPP shape functions according to equations (8.204a)–(8.204c): linear function $C_s \mathcal{G}(\sigma) = 1 - \sigma$; parabolic function $C_s \mathcal{G}(\sigma) = (1 - \sigma)^2$; and cubic function $C_s \mathcal{G}(\sigma) = 1 + (2\sigma - 3)\sigma^2$. Also shown are their derivatives: linear function $C_s \mathcal{G}'(\sigma) = -1$; parabolic function $C_s \mathcal{G}'(\sigma) = -2(1 - \sigma)$; and cubic function $C_s \mathcal{G}'(\sigma) = -6\sigma(1 - \sigma)$. Note the monotonic nature of the function, which has a linear derivative of one sign throughout the boundary layer where $0 \leq \sigma \leq 1$.

8.6.5 Tests with the modified KPP non-local shape function

Figure 8.10 shows results from the modified shape functions (8.204a)–(8.204c) in the idealized test described in Figure 8.8. The first panel shows the very small sensitivity to vertical grid spacing when using the parabolic function (equation (8.204b)). This small sensitivity contrasts to the results from the original shape function as shown in Figure 8.8. All three of the new shape functions show similar small sensitivity to the vertical grid. Furthermore, there is no sign of spurious warming with the new functions.

The second panel in Figure 8.10 exhibits sensitivity to the use of the linear, parabolic, or cubic shape functions (8.204a)–(8.204c). The parabolic shape function generally renders a deeper boundary layer. We can understand that effect by noting that the parabolic shape function places the largest amount of cooling into the upper ocean, as revealed by the derivative shown in Figure 8.9. It is unclear how general this result is, though note that preliminary results from a more realistic seasonally forced test case that also show deeper boundary layers with the parabolic shape function.

8.7 KPP with surface waves

Craig and Banner (1994) considered surface waves in a modification of the Mellor and Yamada (1982) 2.5 order turbulence scheme. Axell (2002) considered also Langmuir turbulence in the $k - \epsilon$ closure scheme. We consider here some issues related to introducing both waves and Langmuir turbulence in the KPP scheme.

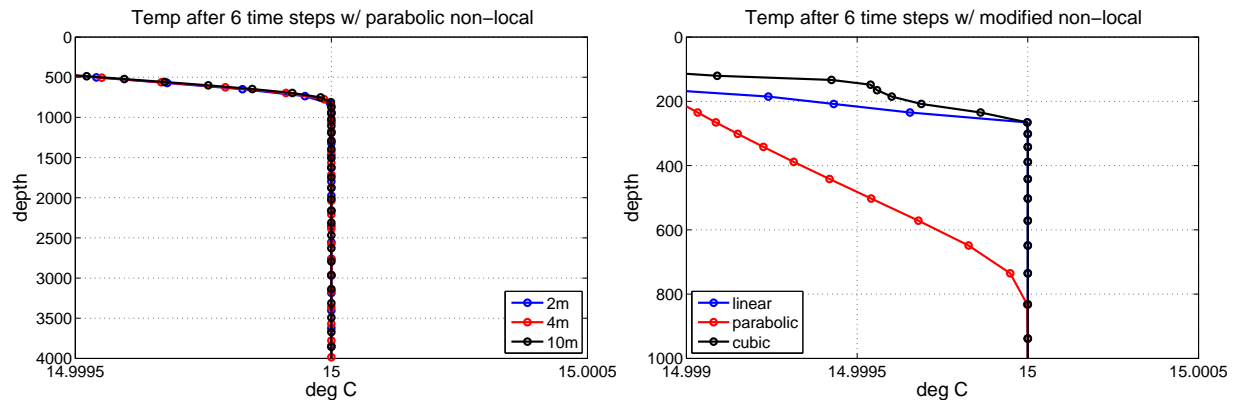


Figure 8.10: Temperature profiles after six time steps (each of one hour). The first panel shows sensitivity to three different model grids from an idealized one-dimensional simulation using the parabolic shape function $\mathcal{G} = (1 - \sigma)^2$ (equation (8.204b)) for the parameterized non-local flux. Details of the grid and experimental design are given in the caption to Figure 8.8. Note the absence of any water warmer than 15°C , and the close agreement for the three simulations with different vertical grid spacings. These results contrast with those shown in Figure 8.8 realized with the shape function $G = \sigma(1 - \sigma)^2$. The second panel here shows sensitivity to the modified non-local structure functions. The parabolic function exhibits the deeper boundary layer relative to the linear and cubic functions. Note the different horizontal and vertical scales for the two panels.

The KPP formulation presented by Large et al. (1994) ignores surface waves and the associated breaking waves and Langmuir turbulence. The basis for KPP must be revisited in regions of waves, since waves modify the Monin-Obukhov similarity scalings (see Terray et al. (1996) for the case of breaking waves, and Section 2.2 of Sullivan and McWilliams (2010) for wave-driven winds). In the presence of waves, the ocean surface contains both breaking waves to enhance upper ocean mixing and dissipation; swell, which can modify the atmospheric planetary boundary layer by providing momentum to lower atmospheric winds; and the coupling of Stokes drift to currents to produce Langmuir cells and associated turbulence (McWilliams et al., 1997a). These processes act in addition to and in interaction with the shear induced eddies and buoyant plumes traditionally considered as part of the KPP scheme. The modifications to KPP with waves represents a research project, with work from Belcher et al. (2012) a step towards this goal, in which they consider the regimes where winds are more or less important than Langmuir turbulence.

In this section, we identify some incremental steps that may be considered for modifying aspects of KPP to incorporate features of surface waves. Even with these more humble aspirations, there are many questions.

8.7.1 Modified budgets with Stokes velocity

Large eddy simulations that incorporate surface waves, such as those from McWilliams et al. (1997b), McWilliams and Sullivan (2001) and Sullivan et al. (2007), include a contribution in the momentum equation from the Stokes velocity on the Coriolis force as well as a vortex force. Additionally, the tracer equation includes advection from the Stokes velocity. Finally, the subgrid scale turbulent kinetic energy equation also includes advection by the Stokes velocity, as well as vertical shear of the Stokes velocity coupled to the subgrid scale stresses, thus acting as a source for turbulent kinetic energy. Mathematically, these

terms take the form (see equations (4a), (4b) and (4c) from [Sullivan and McWilliams \(2010\)](#))

$$\frac{\partial \mathbf{v}}{\partial t} = \dots - f \hat{\mathbf{z}} \wedge \mathbf{v}^{\text{stokes}} + \mathbf{v}^{\text{stokes}} \wedge \boldsymbol{\omega} \quad (8.208)$$

$$\frac{\partial C}{\partial t} = \dots - \mathbf{v}^{\text{stokes}} \cdot \nabla C \quad (8.209)$$

$$\frac{\partial E}{\partial t} = \dots - \mathbf{v}^{\text{stokes}} \cdot \nabla E - \tau_{ij} \frac{\partial v_i^{\text{stokes}}}{\partial x_j} \quad (8.210)$$

where \mathbf{v} is the velocity field (u, v, w) resolved by the LES, $\boldsymbol{\omega} = \nabla \wedge \mathbf{v}$ is the vorticity, $\mathbf{v}^{\text{stokes}}$ is the Stokes velocity due to wave motions, C is an arbitrary tracer concentration, E is the turbulent kinetic energy, and τ_{ij} is the deviatoric subgrid-scale stress tensor. The dots denote standard terms such as pressure gradients, friction, etc.

The question arises as to whether a hydrostatic primitive equation ocean model should also modify the prognostic equations for momentum and tracer in a manner emulating that done for the LES. We offer the following reasons to *not* do so.

- In present applications with hydrostatic primitive equation ocean models, a wave model provides information about the Stokes velocity, or an estimate of this velocity is made based on wind stress ([Li and Garrett, 1993](#)). However, there is no feedback to the waves from the circulation. Indeed, there is no such feedback considered in the LES studies from [McWilliams et al. \(1997b\)](#), [McWilliams and Sullivan \(2001\)](#) and [Sullivan et al. \(2007\)](#). For the primitive equation models used for climate research, it would be problematic to have a quiescent Eulerian mean flow impacted by a wave to thus initiate inertial circulations. In fact, it is the Stokes circulation itself that should be impacted.
- The Stokes circulation velocity, $\mathbf{v}^{\text{stokes}}$, is generally considered to have only horizontal components

$$\mathbf{v}^{\text{stokes}} = (u^{\text{stokes}}, v^{\text{stokes}}, 0) \quad (8.211)$$

These components are horizontally divergent. Hence, their presence in the flux-form tracer equation appears both as an advection plus a source term.

- As discussed by [Raschle et al. \(2006\)](#), ensemble averaging of these equations eliminates the added vortex force term.
- There are cases where the large-scale Eulerian mean flow in an LES will compensate for the Stokes flow, leading to a vanishing Lagrangian mean velocity. This balance cannot be represented in a primitive equation ocean model, so the selective introduction of only a piece of the full dynamics can lead to spurious effects.

In conclusion, introduction of the Stokes velocity into the tracer and momentum equations of a hydrostatic primitive equation ocean model is *not* recommended.

8.7.2 Modifications from Stokes velocity and Langmuir turbulence

- It is conjectured that the most important change to KPP may arise from enhanced shear due to Stokes velocity when computing bulk Richardson number (Section 8.5.7). We must be careful to note that in some cases, a piece of the Eulerian and Stokes velocities in fact cancel, leaving only a residual velocity whose vertical shear impacts the bulk Richardson number. However, this result needs some care to distinguish the potential for this effect to occur on the larger scaled represented in a primitive equation model. Note that for some reason, [Smyth et al. \(2002\)](#) do not consider this effect in their modifications to KPP from waves and Langmuir turbulence. Perhaps they assume there is a piece of the unresolved Eulerian velocity that exactly cancels the Stokes velocity, thus leaving no new unresolved term in the bulk Richardson number calculation.
- There are additional changes to the turbulent velocity scale, w_λ , that may arise from Langmuir turbulence. Questions arise regarding the precise calculation of the Langmuir number, the scaling added to the turbulence velocity scale, and the depth dependence of the Langmuir number.

8.8 Symbols used in this chapter

We here list many of the symbols used in this chapter, along with the pages, equations, or sections where they are described.

Greek Symbols

- α = thermal expansion coefficient (equation (8.51)), with units $^{\circ}\text{C}^{-1}$.
- β = haline contraction coefficient (equation (8.52)), with units ppt^{-1} .
- $\beta_T = \overline{wb}^{d=h_e} / \overline{wb}^0$ = ratio of the turbulent buoyancy flux at the entrainment depth in the boundary layer, to the buoyancy flux at the ocean surface. Empirically, it has been found that $\beta_T = -0.2$. See Figure 8.2 for an illustration.
- $\beta_\lambda = \overline{w\lambda}^\epsilon / \overline{w\lambda}^0$ = ratio of the turbulent flux at the base of the surface layer, $\sigma = \epsilon$, to the flux at the upper ocean interface, $z = \eta$ (equation (8.124)).
- γ_λ = non-local term resulting from the KPP parameterization (equation (8.9) and Section 8.1.4). This term has units equal to the vertical derivative of Λ ; i.e., $[\Lambda] \text{ m}^{-1}$.
- δ_k = vertical finite difference operator (equation (8.49)).
- ϵ = fraction of the KPP boundary layer comprised of the Monin-Obukhov surface sublayer. The KPP scheme generally sets $\epsilon = 0.1$ (equation (8.88) and Figure 8.1).
- $\zeta = d/L$ = dimensionless scaled distance (equation (8.78c)), where d is the depth within the surface boundary layer (equation (2.2) and (8.18)), and L is the Monin-Obukhov length scale (equation (8.79)).
- η = ocean free surface height (metre) relative to a resting ocean surface at $z = 0$ (page 37).
- (Θ, θ) = Eulerian mean potential or conservative temperature, and its corresponding turbulent fluctuation (page 38).
- (Θ, θ) = Eulerian mean potential or conservative temperature, and its corresponding turbulent fluctuation (page 38).
- $\Theta_* = -\overline{w\theta}^0 / u_*$ = scale for surface turbulent temperature fluctuations used in the Monin-Obukhov similarity theory (equation (8.72)). The sign is chosen so that turbulent fluxes leading to surface ocean cooling, $\overline{w\theta}^0 > 0$, correspond to a negative turbulent temperature scale, $\Theta_* < 0$.
- $\kappa = 0.40$ = dimensionless von Karman constant (equation (8.77)).
- (Λ, λ) = Eulerian mean of a tracer or velocity component within the surface ocean boundary layer, and its corresponding turbulent fluctuation (page 37). Note that (X, x) is the notation used in Large et al. (1994) and Large (1998), but we prefer the Greek (Λ, λ) to avoid confusion with the horizontal spatial coordinate.
- ρ = *in situ* density with units kg m^{-3} (equation (8.30)).
- ρ_o = constant reference density for the Boussinesq approximation, with units kg m^{-3} (equation (8.30)).
- $\sigma = d/h$ = non-dimensional depth within the boundary layer, with $\sigma = 0$ at the ocean free surface and $\sigma = 1$ at the base of the boundary layer (equation (8.17)).
- τ = momentum flux at the ocean surface (Figure 8.1), with units N m^{-2} .
- ϕ_Λ = dimensionless similarity function or flux profile (equation 8.76)).

Latin Symbols

- a_0, a_1, a_2, a_3 = non-dimensional expansion coefficients for the non-dimensional vertical shape function $G_\lambda(\sigma)$ (equation (8.23) and Section 8.5.3). The shape function depends on the field diffused, with this dependence arising from matching to interior diffusivities, which are generally a function of λ .
- a_λ = dimensionless matching coefficient for specifying the similarity function ϕ_Λ in the convective limit where $u_* = 0$ and $B_f < 0$ (equation (8.107)).
- (B, b) = Eulerian mean ocean buoyancy with units m s^{-2} (equation (8.31), and its turbulent fluctuation (equation (8.63)).
- B_0 = ocean buoyancy at the surface, with units m s^{-2} (Figure 8.1).
- B_* = buoyancy scale, with units m s^{-2} , for use in Monin-Obukhov theory (equation 8.74)).
- B_f = buoyancy forcing in the boundary layer, with units $\text{m}^2 \text{s}^{-3}$ (equation (8.61) and Section 8.3.10). Positive values add buoyancy to the ocean, thus stabilizing the boundary layer. Negative values destabilize the boundary layer and lead to non-local mixing (Section 8.1.4).
- B_R = buoyancy forcing due to penetrative radiation, with units $\text{m}^2 \text{s}^{-3}$ (equation (8.64) and Section 8.3.10). Positive values add buoyancy to the ocean, thus stabilizing the boundary layer.
- B_r = surface layer averaged buoyancy (m s^{-2}) for bulk Richardson number (equation 8.170)).
- c_λ = dimensionless matching coefficient for specifying the similarity function ϕ_Λ in the convective limit where $u_* = 0$ and $B_f < 0$ (equation (8.107)).
- C_* = dimensionless coefficient used in specifying the non-local transport term (equation (8.142)).
- C_p^o is the seawater heat capacity at constant pressure ($\text{J kg}^{-1} \text{ }^\circ\text{C}^{-1}$). IOC et al. (2010) provides the most precise value appropriate for an ocean with heat measured through conservative temperature. See page 46.
- C_v = dimensionless coefficient setting buoyancy frequency at the entrainment depth (equation 8.179)).
- $C_s = C_* \kappa (c_s \kappa \epsilon)^{1/3}$ = dimensionless coefficient as per equation (8.141).
- $d = -z + \eta$ is the depth (metre) from the ocean free surface to a point within the ocean (equation (2.2) and (8.18)).
- dz = thickness (metre) of a tracer cell appearing in the mass and tracer equations (equation (8.32)).
- g = constant gravitational acceleration (units m s^{-2}) (equation (8.31)).
- $G_\lambda(\sigma)$ = non-dimensional vertical shape or structure function used to smoothly transition from the ocean surface to the bottom of the boundary layer (equation 8.23 and Section 8.5.3).
- $G_{\text{universal}}(\sigma) = \sigma(1 - \sigma)^2$ = non-dimensional vertical shape or structure function used to smoothly transition from the ocean surface to the bottom of the boundary layer (equation (8.157)). This form deviates from the approach taken in Large et al. (1994), but it is recommended for use with all tracers using CVMix implementation of KPP. See Section 8.5.3).
- $\mathcal{G}(\sigma)$ = non-dimensional vertical shape or structure function for the parameterized non-local flux, used to smoothly transition from the ocean surface to the bottom of the boundary layer (equations 8.204a)–(8.204c)). This shape function is distinct from that used for the diffusivity.
- H = depth (metre) at the ocean bottom relative to a resting ocean surface at $z = 0$ (page 37).
- $\mathcal{H} = z - \eta$ = height (metre) above the sea surface (page 37).
- H^{fusion} = latent heat of fusion for fresh water = $3.34 \times 10^5 \text{ J kg}^{-1}$ (equation (8.42)).
- H^{vapor} = latent heat of vaporization for fresh water = $2.5 \times 10^6 \text{ J kg}^{-1}$ (equation (8.40)).
- $h \geq 0$ is the boundary layer thickness (metre) measured from the ocean free surface to the base of the surface boundary layer (equation (8.16) and Figure 8.1).

- $h_e \geq 0$ is the entrainment depth (metre) where the buoyancy flux reaches a negative extrema (Figure 8.1).
- $h_E = 0.7 u_* / |f|$ is the Ekman length scale (equation (8.187)).
- $h_m \geq 0$ is the mixed layer depth (metre), determined by a density criteria and measured from the ocean free surface to the base of the mixed layer (Figure 8.1).
- $h_{obl} \geq 0$ is the thickness (metre) of the surface boundary layer as measured from $z = 0$ to the boundary layer base (equation (8.19)).
- K_λ = vertical kinematic diffusivity ($\text{m}^2 \text{s}^{-1}$) in the surface boundary layer resulting from the KPP parameterization (equation (8.13)). This diffusivity is used to parameterize the downgradient diffusive portion of the KPP boundary layer scheme.
- $K_\lambda^{\text{non-local}}$ = vertical kinematic diffusivity ($\text{m}^2 \text{s}^{-1}$) in the surface boundary layer resulting from the KPP parameterization (equation (8.12)). This diffusivity is used to parameterize the non-local portion of the KPP boundary layer scheme.
- K_m = vertical kinematic viscosity for momentum ($\text{m}^2 \text{s}^{-1}$) in the surface boundary layer resulting from the KPP parameterization. It is related to the KPP tracer diffusivity through the Prandtl number as in equation (8.114).
- K_s = vertical kinematic diffusivity for scalar fields ($\text{m}^2 \text{s}^{-1}$) in the surface boundary layer resulting from the KPP parameterization (equation (8.13)). The KPP diffusivity is the same for all tracers, including temperature, salinity, and passive tracers.
- L = Monin-Obukhov length scale determined by the ratio of the momentum forcing to buoyancy forcing (equation (8.79)). L can be positive or negative as per the regimes given by equation (8.80). It is the depth scale at which buoyancy production of turbulent kinetic energy is of the same magnitude as shear production.
- Pr = Prandtl number, which is the ratio of the KPP momentum viscosity to KPP scalar diffusivity (equations (8.114) and (8.115)).
- Q_{latent} = latent heat flux at the ocean surface (equation (8.38)) with units of W m^{-2} and negative values for heat leaving the ocean ($Q_{\text{latent}} < 0$ for ocean cooling).
- Q_{long} = longwave heat flux at the ocean surface (equation (8.38)) with units of W m^{-2} and negative values for heat leaving the ocean ($Q_{\text{long}} < 0$ for ocean cooling).
- Q_{sens} = sensible heat flux at the ocean surface (equation (8.38)) with units of W m^{-2} and negative values for heat leaving the ocean ($Q_{\text{sens}} < 0$ for ocean cooling).
- Q_m = mass flux of water crossing the ocean surface (equation (8.34)) with units of $\text{kg m}^{-2} \text{s}^{-1}$ and positive values for mass entering the ocean domain ($Q_m > 0$ for mass entering the ocean).
- $Q_R > 0$ = penetrative heat flux due to shortwave radiation (equations (8.65) and (8.151a)) with units of W m^{-2} and positive values for heat entering the ocean surface ($Q_R > 0$ for ocean heating).
- Q_S = mass flux of salt crossing the ocean surface (equation (8.33)) with units of $\text{kg m}^{-2} \text{s}^{-1}$ and positive values for salt entering the ocean surface ($Q_S > 0$ for salt entering the ocean).
- $Q_\theta^{\text{non-pen}} C_p^o$ = non-penetrative surface heat flux associated with turbulent processes (latent and sensible) and radiative longwave cooling (W m^{-2}). The sign convention is chosen so that $Q_\theta^{\text{non-pen}} < 0$ for heat leaving the ocean surface (i.e., ocean cooling). See equation (8.32) and Section 8.3.5.
- $Q_\theta^{\text{pen}}(z = \eta) C_p^o$ = radiative shortwave heat flux (W m^{-2}) entering the ocean through its surface at $z = \eta$, with $Q_\theta^{\text{pen}}(\eta) > 0$ warming the ocean surface. Likewise, $C_p^o Q_\theta^{\text{pen}}(z = -\Delta z)$ is the radiative shortwave heat flux leaving the top cell through its bottom face. See Section 8.3.7.
- Ri_b = bulk Richardson number used to compute the KPP boundary layer thickness (equation (8.170)).
- Ri_c = critical bulk Richardson number used to compute the KPP boundary layer thickness (equations (8.169) and (8.182)). $\text{Ri}_c = 0.3$ is recommended by Large et al. (1994).
- (S, s) = Eulerian mean salinity or scalar tracer, and its corresponding turbulent fluctuation (page 38).

- S_m = concentration of salt in the mass flux crossing the ocean surface (equation (8.33)). Usually this concentration is set to zero.
- $S_* = -\overline{ws}^0/u_*$ = scale for surface turbulent salinity or scalar tracer fluctuations used in the Monin-Obukhov similarity theory (equation (8.73)). The sign is chosen so that turbulent fluxes leading to surface ocean freshening, $\overline{ws}^0 > 0$, correspond to a negative turbulent salinity scale, $S_* < 0$.
- $u_*^2 = |\overline{w\mathbf{u}}^0| = |\boldsymbol{\tau}|/\rho_0$ = squared surface friction velocity used in the Monin-Obukhov similarity theory (equations (8.70) and (8.71)).
- \mathbf{U}_r = surface layer averaged horizontal velocity (m s^{-1}) used to compute the bulk Richardson number (equation 8.170)).
- U_t = parameterized unresolved speed (m s^{-1}) used to compute the Bulk Richardson number (equation 8.170) and Section 8.5.7.3).
- (W, w) = Eulerian mean vertical velocity (m s^{-1}) component and its turbulent fluctuation, with $W > 0$ for upward mean motion, and $w > 0$ for upward turbulent fluctuations (page 38).
- w_λ = turbulent velocity scale (units m s^{-1}) (page 41 and Section 8.5.1).
- w_m = turbulent velocity scale for momentum (units m s^{-1}) (Figure 8.3).
- w_s = turbulent velocity scale for scalars, such as temperature, salinity, and passive tracers (units m s^{-1}). This velocity scale is the same for all tracers (Figure 8.3).
- $w_* = (-B_f h)^{1/3}$ = turbulent velocity scale in the convective limit (units m s^{-1}), with $B_f < 0$ the destabilizing surface buoyancy flux, and $h > 0$ the boundary layer depth (equation 8.106)).
- \overline{wb}^0 = Eulerian correlation at the ocean surface between the fluctuating turbulent vertical velocity and a fluctuating surface buoyancy. It is equated to the non-penetrative portion of the surface buoyancy flux (equation (8.63)). This term is also called the *kinematic* turbulent buoyancy flux. The units are $\text{m}^2 \text{s}^{-3}$.
- $\overline{w\mathbf{u}}^0$ = Eulerian correlation, at the ocean surface, between the fluctuating turbulent vertical velocity and the fluctuating horizontal velocity. It is equated to the surface wind stress forcing through equation (8.30). This term is also called the *kinematic* turbulent momentum flux. The units are $\text{m}^2 \text{s}^{-2}$.
- $W\Lambda$ = vertical advective flux of the Eulerian mean field Λ by the Eulerian mean vertical velocity component W (equation (8.8)). This flux is represented by the advection operator. It has units of velocity * $[\Lambda]$.
- $\overline{w\lambda}$ = Eulerian correlation of the fluctuating turbulent vertical velocity and a fluctuating scalar or vector field (page 38). Note that $\overline{w\lambda} > 0$ for an upward turbulent flux for λ . It has units of velocity * $[\lambda]$.
- $\overline{w\lambda}^{\text{local}} = -K_\lambda \partial\Lambda/\partial z$ is the local portion of the KPP parameterization of the turbulent flux (equation (8.11)). It has units of velocity * $[\lambda]$.
- $\overline{w\lambda}^{\text{non-local}} = K_\lambda^{\text{non-local}} \gamma_\lambda$ is the non-local portion of the KPP parameterization of the turbulent flux (equation (8.12) and Sections 8.5.1).
- z = geopotential vertical coordinate (metre) with $z = 0$ at the resting ocean surface, $z = -H(x, y)$ at the ocean bottom, and $z = \eta(x, y, t)$ at the ocean free surface (page 37).
- Z_λ = roughness length (metre) appearing in the Monin-Obukhov similarity theory (equation 8.86)).

Bibliography

- Adcroft, A., Hill, C., Marshall, J., 1999. A new treatment of the coriolis terms in c-grid models at both high and low resolutions. *Monthly Weather Review* 127, 1928–1936.
- Anderson, W., Gnanadesikan, A., Hallberg, R. W., Dunne, J. P., Samuels, B. L., 2007. Impact of ocean color on the maintenance of the pacific cold tongue. *Geophysical Research Letters* 34-L11609, DOI:10.1029/2007GL030100.
- Anderson, W., Gnanadesikan, A., Wittenberg, A. T., 2009. Regional impacts of ocean color on tropical pacific variability. *Ocean Science* 5, DOI:10.5194/os-5-313-2009.
- Axell, L., 2002. Wind-driven internal waves and Langmuir circulations in a numerical ocean model of the southern Baltic Sea. *Journal of Geophysical Research* 107, 107(C11), 3204, doi:10.1029/2001JC000922.
- Belcher, S., Grant, A., Hanley, K., Fox-Kemper, B., Van Roekel, L., Sullivan, P., Large, W., Brown, A., Hines, A., Calvert, D., Rutgersson, A., Petterson, H., Bidlot, J., Janssen, P., Polton, J. A., 2012. A global perspective on Langmuir turbulence in the ocean surface boundary layer. *Geophysical Research Letters* 39-L18605, doi:10.1029/2012GL052932.
- Bryan, K., Lewis, L. J., 1979. A water mass model of the world ocean. *Journal of Geophysical Research* 84, 2503–2517.
- Chang, Y. S., Xu, X., Özgökmen, T. M., Chassignet, E. P., Peters, H., Fischer, P. F., 2005. Comparison of gravity current mixing parameterizations and calibration using a high-resolution 3d nonhydrostatic spectral element model. *Ocean Modelling* 3-4, 342–368.
- Cox, M. D., 1984. *A Primitive Equation, 3-Dimensional Model of the Ocean*. NOAA/Geophysical Fluid Dynamics Laboratory, Princeton, USA.
- Craig, P., Banner, M., 1994. Modeling wave-enhanced turbulence in the surface ocean layer. *Journal of Physical Oceanography* 24, 2546–2559.
- Danabasoglu, G., Large, W. G., Tribbia, J. J., Gent, P. R., Briegleb, B. P., McWilliams, J. C., 2006. Diurnal coupling in the tropical oceans of CCSM3. *Journal of Climate* 19, 2347–2365.
- Dunne, J. P., John, J. G., Hallberg, R. W., Griffies, S. M., Shevliakova, E. N., Stouffer, R. J., Krasting, J. P., Sentman, L. A., Milly, P. C. D., Malyshev, S. L., Adcroft, A. J., Cooke, W., Dunne, K. A., Harrison, M. J., Levy, H., Samuels, B. L., Spelman, M., Winton, M., Wittenberg, A. T., Phillips, P. J., Zadeh, N., 2012. GFDLs ESM2 global coupled climate-carbon Earth System Models Part I: Physical formulation and baseline simulation characteristics. *Journal of Climate* 25, 6646–6665.
- Durski, S. M., Glenn, S. M., Haidvogel, D. B., 2004. Vertical mixing schemes in the coastal ocean: Comparison of the level 2.5 Mellor-Yamada scheme with an enhanced version of the K profile parameterization. *Journal of Geophysical Research* 109, doi:10.1029/2002JC001702.

- Fairall, C., Bradley, E., Godfrey, J., Wick, G., Edson, J., Young, G., 1996. Cool-skin and warm-layer effects on sea surface temperature. *Journal of Geophysical Research* 101, 1295–1308.
- Gent, P., Bryan, F., Danabasoglu, G., Doney, S., Holland, W., Large, W., McWilliams, J., 1998. The NCAR climate system model global ocean component. *Journal of Climate* 11, 1287–1306.
- Gill, A., 1982. *Atmosphere-Ocean Dynamics*. Vol. 30 of International Geophysics Series. Academic Press, London, 662 + xv pp.
- Goosens, M., Mittelbach, F., Samarin, A., 1994. *The L^AT_EX Companion*. Addison-Wesley, Reading, Massachusetts, 528 pp.
- Griffies, S. M., 2004. *Fundamentals of Ocean Climate Models*. Princeton University Press, Princeton, USA, 518+xxxiv pages.
- Griffies, S. M., Biastoch, A., Böning, C. W., Bryan, F., Danabasoglu, G., Chassignet, E., England, M. H., Gerdes, R., Haak, H., Hallberg, R. W., Hazeleger, W., Jungclaus, J., Large, W. G., Madec, G., Pirani, A., Samuels, B. L., Scheinert, M., Gupta, A. S., Severijns, C. A., Simmons, H. L., Treguier, A. M., Winton, M., Yeager, S., Yin, J., 2009. Coordinated Ocean-ice Reference Experiments (COREs). *Ocean Modelling* 26, 1–46.
- Griffies, S. M., Gnanadesikan, A., Dixon, K. W., Dunne, J. P., Gerdes, R., Harrison, M. J., Rosati, A., Russell, J., Samuels, B. L., Spelman, M. J., Winton, M., Zhang, R., 2005. Formulation of an ocean model for global climate simulations. *Ocean Science* 1, 45–79.
- Griffies, S. M., Pacanowski, R., Schmidt, M., Balaji, V., 2001. Tracer conservation with an explicit free surface method for z-coordinate ocean models. *Monthly Weather Review* 129, 1081–1098.
- Holland, W., Chow, J., Bryan, F., 1998. Application of a third-order upwind scheme in the NCAR ocean model. *Journal of Climate* 11, 1487–1493.
- Huang, R. X., 1993. Real freshwater flux as a natural boundary condition for the salinity balance and thermohaline circulation forced by evaporation and precipitation. *Journal of Physical Oceanography* 23, 2428–2446.
- IOC, SCOR, IAPSO, 2010. *The international thermodynamic equation of seawater-2010: calculation and use of thermodynamic properties*. Intergovernmental Oceanographic Commission, Manuals and Guides No. 56, UNESCO, available from <http://www.TEOS-10.org>, 196pp.
- Ivey, G., Imberger, J., 1991. On the nature of turbulence in a stratified fluid. Part I: The energetics of mixing. *Journal of Physical Oceanography* 25, 650–658.
- Jackson, L., Hallberg, R., Legg, S., 2008. A parameterization of shear-driven turbulence for ocean climate models. *Journal of Physical Oceanography* 38, 1033–1053.
- Jayne, S., 2009. The impact of abyssal mixing parameterizations in an ocean general circulation model. *Journal of Physical Oceanography* 39, 1756–1775.
- Jayne, S., St.Laurent, L. C., 2001. Parameterizing tidal dissipation over rough topography. *Geophysical Research Letters* 28, 811–814.
- Jochum, M., 2009. Impact of latitudinal variations in vertical diffusivity on climate simulations. *Journal of Geophysical Research* 114 C01010, doi:10.1029/2008JC005030.
- Kantha, L. H., Clayson, C. A., 2000. *Small Scale Processes in Geophysical Fluid Flows*. Academic Press, New York, USA, 883 pp.
- Killworth, P. D., Stainforth, D., Webb, D. J., Paterson, S. M., 1991. The development of a free-surface Bryan-Cox-Semtner ocean model. *Journal of Physical Oceanography* 21, 1333–1348.
- Klinger, B. A., Marshall, J., Send, U., 1996. Representation of convective plumes by vertical adjustment. *Journal of Geophysical Research* 101, 18175–18182.

- Klymak, J., Moum, J., Nash, J., Kunze, E., Girton, J., Carter, G., Lee, C., Sanford, T., Gregg, M., 2005. An estimate of tidal energy lost to turbulence at the hawaiian ridge. *Journal of Physical Oceanography* submitted.
- Lamport, L., 1994. \LaTeX : A Documentation Preparation System User's Guide and Reference Manual. Addison-Wesley, Reading, Massachusetts, 272 pp.
- Large, W., 1998. Modeling the oceanic boundary layer. In: Chassignet, E. P., Verron, J. (Eds.), *Ocean Modeling and Parameterization*. Vol. 516 of NATO ASI Mathematical and Physical Sciences Series. Kluwer, pp. 81–120.
- Large, W., Gent, P., 1999. Validation of vertical mixing in an equatorial ocean model using large eddy simulations and observations. *Journal of Physical Oceanography* 29, 449–464.
- Large, W., McWilliams, J., Doney, S., 1994. Oceanic vertical mixing: a review and a model with a nonlocal boundary layer parameterization. *Reviews of Geophysics* 32, 363–403.
- Large, W. G., 2012. An ocean climate modeling perspective on buoyancy-driven flows. In: Chassignet, E. P., Cenedese, C., Verron, J. (Eds.), *Buoyancy-driven flows*. Cambridge, pp. 240–280.
- Large, W. G., Danabasoglu, G., Doney, S. C., McWilliams, J. C., 1997. Sensitivity to surface forcing and boundary layer mixing in a global ocean model: annual-mean climatology. *Journal of Physical Oceanography* 27, 2418–2447.
- Large, W. G., Yeager, S., 2009. The global climatology of an interannually varying air-sea flux data set. *Climate Dynamics* 33, 341–364.
- Laurent, L. C. S., Schmitt, R., 1999. The contribution of salt fingers to vertical mixing in the north atlantic tracer release experiment. *Journal of Physical Oceanography* 29, 1404–1424.
- Ledwell, J. R., Watson, A. J., Law, C. S., 1993. Evidence for slow mixing across the pycnocline from an open-ocean tracer-release experiment. *Nature* 364, 701–703.
- Legg, S., Hallberg, R., Girton, J., 2006. Comparison of entrainment in overflows simulated by z-coordinate, isopycnal and non-hydrostatic models. *Ocean Modelling* 11, 69–97.
- Lemarié, F., Kurian, J., Shchepetkin, A. F., Molemaker, M. J., Colas, F., McWilliams, J. C., 2012. Are there inescapable issues prohibiting the use of terrain-following coordinates in climate models? *Ocean Modelling* 42, 57–79.
- Li, M., Garrett, C., 1993. Cell merging and the jet/downwelling ratio in Langmuir circulation. *Journal of Marine Research* 51, 737–769.
- Li, X., Chao, Y., McWilliams, J. C., Fu, L. L., 2001. A comparison of two vertical-mixing schemes in a Pacific ocean general circulation model. *Journal of Climate* 14, 1377–1398.
- Manizza, M., Le Quere, C., Watson, A., Buitenhuis, E., 2005. Bio-optical feedbacks among phytoplankton, upper ocean physics and sea-ice in a global model. *Geophysical Research Letters* 32, doi:10.1029/2004GL020778.
- McDougall, T. J., 1987. Neutral surfaces. *Journal of Physical Oceanography* 17, 1950–1967.
- McDougall, T. J., 2003. Potential enthalpy: a conservative oceanic variable for evaluating heat content and heat fluxes. *Journal of Physical Oceanography* 33, 945–963.
- McWilliams, J. C., Sullivan, P., 2001. Vertical mixing by Langmuir circulations. *Spill Science and Technology Bulletin* 6, 225–237.
- McWilliams, J. C., Sullivan, P., Moeng, C.-H., 1997a. Langmuir turbulence in the ocean. *Journal of Fluid Mechanics* 334, 1–30.

- McWilliams, J. C., Sullivan, P., Moeng, C.-H., 1997b. Langmuir turbulence in the ocean. *Journal of Fluid Mechanics* 334, 1–30.
- Melet, A., Hallberg, R., Legg, S., Polzin, K., 2013. Sensitivity of the Pacific Ocean state to the vertical distribution of internal-tide driven mixing. *Journal of Physical Oceanography* 43, 602–615.
- Mellor, G. L., Yamada, T., 1982. Development of a turbulent closure model for geophysical fluid problems. *Reviews of Geophysics* 20, 851–875.
- Mesinger, F., 1973. A method for construction of second-order accurate difference schemes permitting no false two-grid-interval waves in the height field. *Tellus* 25, 444–457.
- Miles, J., 1961. On the stability of heterogeneous shear flows. *Journal of Fluid Mechanics* 10, 496–508.
- Moum, J., Caldwell, D., Nash, J., Gunderson, G., 2002. Observations of boundary mixing over the continental slope. *Journal of Physical Oceanography* 32, 2113–2130.
- Osborn, T. R., 1980. Estimates of the local rate of vertical diffusion from dissipation measurements. *Journal of Physical Oceanography* 10, 83–89.
- Pacanowski, R. C., Griffies, S. M., 1999. *The MOM3 Manual*. NOAA/Geophysical Fluid Dynamics Laboratory, Princeton, USA, 680 pp.
- Pacanowski, R. C., Philander, G., 1981. Parameterization of vertical mixing in numerical models of the tropical ocean. *Journal of Physical Oceanography* 11, 1442–1451.
- Polzin, K., 2009. An abyssal recipe. *Ocean Modelling* 30, 298–309.
- Polzin, K. L., Toole, J. M., Ledwell, J. R., Schmitt, R. W., 1997. Spatial variability of turbulent mixing in the abyssal ocean. *Science* 276, 93–96.
- Rahmstorf, S., 1993. A fast and complete convection scheme for ocean models. *Ocean Modelling* 101, 9–11.
- Raschle, N., Arduin, F., Terray, F., 2006. Drift and mixing under the ocean surface: a coherent one-dimensional description with application to unstratified conditions. *Journal of Geophysical Research* 111: C03016.
- Roquet, F., Madec, G., McDougall, T. J., Barker, P. M., 2014. Accurate polynomial expressions for the density and specific volume of seawater using the TEOS-10 standard. *Ocean Modelling* under review.
- Schmitt, R. W., 1994. Double diffusion in oceanography. *Annual Review of Fluid Mechanics* 26, 255–285.
- Shchepetkin, A. F., 2005. If-less kpp. ROMS/TOMS Workshop: Adjoint Modeling and Applications.
- Simmons, H. L., Jayne, S. R., St-Laurent, L. C., Weaver, A. J., 2004. Tidally driven mixing in a numerical model of the ocean general circulation. *Ocean Modelling* 6, 245–263.
- Smyth, G. C. W. D., Skillingstad, E. D., Wijesekera, H., 2002. Nonlocal fluxes and Stokes drift effects in the K-profile parameterization. *Ocean Dynamics* 52, 104–115.
- St-Laurent, L. C., Simmons, H., Jayne, S., 2002. Estimating tidally driven energy in the deep ocean. *Geophysical Research Letters* 29, 2106–2110.
- St-Laurent, L. C., Stringer, S., Garrett, C., Perrault-Joncas, D., 2003. The generation of internal tides at abrupt topography. *Deep-Sea Research* 50, 987–1003.
- St-Laurent, L. C., Toole, J., Schmitt, R., 2001. Buoyancy forcing by turbulence above rough topography in the abyssal Brazil basin. *Journal of Physical Oceanography* 31, 3476–3495.
- Sullivan, P. P., McWilliams, J. C., 2010. Dynamics of winds and currents coupled to surface waves. *Annual Review of Fluid Mechanics* 42, 19–42.

- Sullivan, P. P., McWilliams, J. C., Melville, W. K., 2007. Surface gravity wave effects in the oceanic boundary layer: large-eddy simulation with vortex force and stochastic breakers. *Journal of Fluid Mechanics* 593, 405–452.
- Sweeney, C., Gnanadesikan, A., Griffies, S. M., Harrison, M., Rosati, A., Samuels, B., 2005. Impacts of shortwave penetration depth on large-scale ocean circulation and heat transport. *Journal of Physical Oceanography* 35, 1103–1119.
- Tennekes, H., 1973. The logarithmic wind profile. *Journal of Atmospheric Sciences* 30, 558–567.
- Terray, E., Donelan, M., Agrawal, Y., Drennan, W., Kahma, K., Williams, A., Hwang, P., Kitaigorodskii, S., 1996. Estimates of kinetic energy dissipation under breaking waves. *Journal of Physical Oceanography* 26, 792–807.
- Troen, I. B., Mahrt, L., 1986. A simple model of the atmospheric boundary layer: sensitivity to surface evaporation. *Boundary Layer Meteorology* 37, 129–148.
- Umlauf, L., Burchard, H., Bolding, K., 2005. GOTM: source code and test case documentation: version 3.2. 231pp.
- Vallis, G. K., 2006. *Atmospheric and Oceanic Fluid Dynamics: Fundamentals and Large-scale Circulation*, 1st Edition. Cambridge University Press, Cambridge, 745 + xxv pp.
- Webb, D. J., Coward, A. C., de Cuevas, B. A., Gwilliam, C. S., 1998. The first main run of the OCCAM global ocean model. Internal Document No. 34. Southampton Oceanography Centre, Southampton, England.

Index

- Adcroft et al. (1999), [14](#), [91](#)
Anderson et al. (2007), [69](#), [91](#)
Anderson et al. (2009), [69](#), [91](#)
Axell (2002), [84](#), [91](#)
Belcher et al. (2012), [85](#), [91](#)
Bryan and Lewis (1979), [1](#), [19–21](#), [26](#), [91](#)
Chang et al. (2005), [37](#), [91](#)
Cox (1984), [2](#), [91](#)
Craig and Banner (1994), [53](#), [84](#), [91](#)
Danabasoglu et al. (2006), [37](#), [74](#), [91](#)
Dunne et al. (2012), [29](#), [47](#), [91](#)
Durski et al. (2004), [37](#), [38](#), [41](#), [91](#)
Fairall et al. (1996), [52](#), [91](#)
Gent et al. (1998), [37](#), [92](#)
Gill (1982), [47](#), [92](#)
Goosens et al. (1994), [ii](#), [92](#)
Griffies et al. (2001), [13](#), [47](#), [92](#)
Griffies et al. (2005), [20](#), [21](#), [92](#)
Griffies et al. (2009), [44](#), [47](#), [92](#)
Griffies (2004), [13](#), [92](#)
Holland et al. (1998), [37](#), [92](#)
Huang (1993), [47](#), [92](#)
Ivey and Imberger (1991), [27](#), [92](#)
Jackson et al. (2008), [13](#), [23](#), [92](#)
Jayne and St.Laurent (2001), [26](#), [27](#), [92](#)
Jayne (2009), [26](#), [29–32](#), [92](#)
Jochum (2009), [19](#), [92](#)
Kantha and Clayson (2000), [45](#), [50](#), [52](#), [92](#)
Killworth et al. (1991), [13](#), [92](#)
Klinger et al. (1996), [82](#), [92](#)
Klymak et al. (2005), [29](#), [92](#)
Lamport (1994), [ii](#), [93](#)
Large and Gent (1999), [1](#), [24](#), [76](#), [93](#)
Large and Yeager (2009), [44](#), [45](#), [93](#)
Large et al. (1994), [iii](#), [v](#), [1–4](#), [24](#), [34](#), [37–44](#), [52](#), [53](#),
[55–57](#), [59–69](#), [71](#), [74–78](#), [81](#), [83](#), [85](#), [87–](#)
[89](#), [93](#)
Large et al. (1997), [37](#), [93](#)
Large (1998), [37](#), [40](#), [45](#), [52](#), [87](#), [93](#)
Large (2012), [37](#), [52](#), [93](#)
Laurent and Schmitt (1999), [34](#), [93](#)
Ledwell et al. (1993), [29](#), [93](#)
Legg et al. (2006), [29](#), [93](#)
Lemarié et al. (2012), [77](#), [93](#)
Li and Garrett (1993), [86](#), [93](#)
Li et al. (2001), [37](#), [93](#)
Manizza et al. (2005), [65](#), [69](#), [93](#)
McDougall (1987), [9](#), [93](#)
McDougall (2003), [46](#), [93](#)
McWilliams and Sullivan (2001), [85](#), [86](#), [93](#)
McWilliams et al. (1997a), [85](#), [93](#)
McWilliams et al. (1997b), [85](#), [86](#), [93](#)
Melet et al. (2013), [26–29](#), [94](#)
Mellor and Yamada (1982), [84](#), [94](#)
Mesinger (1973), [13](#), [94](#)
Miles (1961), [12](#), [23](#), [94](#)
Moum et al. (2002), [31](#), [94](#)
Osborn (1980), [27](#), [94](#)
Pacanowski and Griffies (1999), [13](#), [94](#)
Pacanowski and Philander (1981), [1](#), [24](#), [94](#)
Polzin et al. (1997), [31](#), [94](#)
Polzin (2009), [26](#), [28](#), [94](#)
Rahmstorf (1993), [2](#), [82](#), [94](#)
Raschle et al. (2006), [86](#), [94](#)
Roquet et al. (2014), [11](#), [94](#)
Schmitt (1994), [33](#), [94](#)
Shchepetkin (2005), [76](#), [94](#)
Simmons et al. (2004), [1](#), [26](#), [28–32](#), [94](#)
Smyth et al. (2002), [37](#), [43](#), [64](#), [66](#), [86](#), [94](#)
St.Laurent et al. (2001), [31](#), [94](#)
St.Laurent et al. (2002), [28](#), [94](#)
St.Laurent et al. (2003), [29](#), [94](#)
Sullivan and McWilliams (2010), [85](#), [86](#), [94](#)
Sullivan et al. (2007), [85](#), [86](#), [94](#)
Sweeney et al. (2005), [69](#), [95](#)
Tennekes (1973), [53](#), [55](#), [95](#)
Terray et al. (1996), [53](#), [85](#), [95](#)
Troen and Mahrt (1986), [57](#), [60](#), [61](#), [63](#), [95](#)
Umlauf et al. (2005), [1](#), [37](#), [44](#), [95](#)
Vallis (2006), [10](#), [95](#)
Webb et al. (1998), [26](#), [95](#)
IOC et al. (2010), [46](#), [88](#), [92](#)